Dakar's urban pollution plume: A SAMUM-II case study on the plume structure and the influence of urban emissions on dust physico-chemical and radiative properties

Andreas Veira

Munich, March 2011

Dakar's urban pollution plume: A SAMUM-II case study on the plume structure and the influence of urban emissions on dust physico-chemical and radiative properties

Andreas Veira

Diploma Thesis
at the Meteorological Institute
Ludwig–Maximilians–University
Munich

by
Andreas Veira

Munich, 31 March 2011

First Examiner: PD Dr. Andreas Petzold
Second Examiner: Prof. Dr. Bernhard Mayer

Contents

Contents i

Abstract iii

Zusammenfassung v

1 Introduction 1
- 1.1 Scientific Background . . . 1
- 1.2 Objectives, Aims and Tasks of this Study . . . 5

2 Theoretical Background 7
- 2.1 Formation, Evolution and Deposition of Aerosols . . . 7
- 2.2 Aerosol Size Distributions . . . 11
- 2.3 Aerosol Optical Properties . . . 14
  - 2.3.1 Theory of scattering and absorption of light by aerosol particles . 14
  - 2.3.2 Optical properties of mixed aerosol compositions . . . 19
  - 2.3.3 Optical parameters for particle ensembles . . . 21
- 2.4 Sea Breezes . . . 23
- 2.5 Description of the MM5 Model . . . 26

3 Instrumentation and Analysis Methods 29
- 3.1 Instrumentation . . . 29
  - 3.1.1 Particle number concentration . . . 30
  - 3.1.2 Size distribution . . . 34
  - 3.1.3 Absorption . . . 36
  - 3.1.4 Volatility . . . 39
  - 3.1.5 Aerosol optical depth and extinction coefficient . . . 40
  - 3.1.6 Single particle chemical analysis . . . 42
  - 3.1.7 Meteorological data . . . 43
- 3.2 Data Analysis Methods . . . 44
  - 3.2.1 Overall analysis scheme . . . 44
  - 3.2.2 PSAP data analysis scheme . . . 45
  - 3.2.3 Set-up of the MM5 model . . . 50
  - 3.2.4 Back trajectories . . . 52

4 Results **53**
4.1 Flight Strategy . . . 53
4.2 Results from the Basic Data Analysis . . . 57
4.2.1 HSRL data . . . 57
4.2.2 In-situ measurements . . . 59
4.3 Meteorological Analysis and Plume Structure . . . 60
4.3.1 HSRL data and the local circulation pattern . . . 60
4.3.2 ECMWF analysis data, synoptic data and Falcon in-situ data . . . 63
4.3.3 MM5 model results . . . 67
4.4 Physico-Chemical and Optical Properties . . . 74
4.4.1 Particle microphysical properties . . . 74
4.4.2 Particle optical properties . . . 79
4.4.3 Particle chemical composition and refractive index . . . 82

5 Discussion and Conclusions **87**
5.1 Plume Structure and Meteorological Analysis . . . 87
5.1.1 General plume structure . . . 88
5.1.2 Sea breeze circulation . . . 88
5.1.3 Air mass characterization . . . 90
5.1.4 Further development of the plume . . . 92
5.2 Aerosol Properties . . . 93

6 Summary and Future Work **97**

Bibliography **99**

A MM5 Figures and Tables **109**

B HSRL Figures **125**

List of Abbreviations **129**

List of Symbols **131**

List of Figures **136**

List of Tables **137**

Acknowledgment **139**

Erklärung **141**

Abstract

In the framework of the Saharan Mineral Dust Experiment (SAMUM-II) in 2008 the mixing of the urban pollution plume of Dakar (Senegal) with mineral dust aerosol was investigated. Radiative properties of mineral dust mixed with anthropogenic pollution are in the focus of current research, because deserts are by far the strongest sources for airborne particulate matter on a global scale, and, driven by growing megacities in arid areas, the impact of anthropogenic pollution on the physico-chemical properties of mineral dust becomes more and more relevant. Within this case study extensive airborne aerosol in-situ measurements as well as remote sensing data from a High Spectral Resolution Lidar (HSRL) were analyzed. The results from these measurements show a significant increase of the aerosol optical depth and the extinction coefficient as well as considerably enhanced number concentrations and absorption over the urban area of Dakar compared to pure mineral dust. In order to achieve a reliable basis for the interpretation of the airborne measurements, the plume structure and the meteorological conditions, which determine extension and evolution of the plume, were investigated in detail by means of simulations with a mesoscale numerical weather prediction model. The meteorological analysis illustrates that the superposition of a strong westward mesoscale flow and a sea breeze circulation determined the spatial distribution of the plume. Compared to measurements in pure mineral dust, the in-situ measured particle size distribution showed a large increase in sub-300 nm particles (up to a factor of 60), while the fraction of larger particles with diameters $d_p > 500$ nm remained unaffected. The fraction of volatile particles was significantly enhanced (from 20 % up to 70 %). In contrast to pure mineral dust and less polluted plume areas, where single scattering albedos ω_0 between 0.95 and 0.99 (for a wavelength of 530 nm) were measured, an $\omega_{0,min} = 0.907 \pm 0.027$ was observed directly in the plume center. Similar to results from SAMUM-I (located in Morocco, 2006) absorption coefficients had a maximum value of $12.0 \pm 2.6\,\mathrm{Mm}^{-1}$, but in contrast to those measurements near the urban area of Casablanca, the Ångström coefficient of absorption $\mathring{a}_{ap}$ ranged between 2.3 and 4.5 over Dakar. Thus this parameter behaves completely different to the results from SAMUM-I, where an $\mathring{a}_{ap}$ of 1.28 ± 0.28 had been detected. Size distributions and transmission electron microscopy analyses indicate that the observed anthropogenic soot aerosol was externally mixed. Soot constituted a maximum particle volume fraction of 1.028 ± 0.434 % (corresponding to a mass concentration of $1.33 \pm 0.56\,\mu\mathrm{g/m}^3$) and a maximum increase in the imaginary part of the refractive index at 530 nm from 0.001–0.002 (for pure mineral dust) to 0.0065 ± 0.0025 (for the plume center) was observed. The high imaginary part computed for the plume center suggests that there is an increased absorption of solar radiation within the plume center. However, this value is still within the natural variability of previous mineral dust measurements. In summary significant changes in optical and microphysical properties of mineral dust due to mixing with Dakar's anthropogenic pollution plume were found to be locally confined.

Zusammenfassung

Im Rahmen des Saharastaub Experiments SAMUM-II im Jahr 2008 wurde die Einmischung anthropogenen Aerosols der Großstadt Dakar (Senegal) in Wüstenstaubaerosol untersucht. Die Strahlungseigenschaften von Mischungen aus Wüstenstaub und anthropogenem Aerosol sind Bestandteil aktueller Forschung, da Wüsten global gesehen die größte Quelle von Aerosolen darstellen und gleichzeitig ein starkes Wachstum städtischer Agglomerationen in ariden Gebieten zu beobachten ist. In der vorliegenden Fallstudie wurden sowohl Flugzeug getragene in-situ Messungen als auch Fernerkundungsdaten eines spektral hochauflösenden Lidars (HSRL) ausgewertet. Die Messergebnisse zeigen über der Agglomeration von Dakar sowohl eine signifikante Zunahme der aerosol-optischen Dicke als auch eine deutliche Erhöhung von Partikelkonzentrationen und Absorptionskoeffizienten im Vergleich zu reinem Wüstenstaub. Um eine belastbare Basis für die Interpretation der Flugzeugmessdaten zu schaffen, wurden die meteorologischen Bedingungen, welche die Ausdehnung und Entwicklung der Aerosolfahne von Dakar bestimmten, anhand von Simulationen eines numerischen Wettermodels detailiert untersucht. Die meteorologische Analyse zeigt, dass Lage, Ausdehnung und Struktur der Aerosolfahne durch die Überlagerung der westwärts gerichteten mesoskaligen Strömung mit einer lokalen Seebrise entstanden. Im Vergleich zu Messungen im reinen Wüstenstaub war im Bereich der urbanen Aerosolfahne ein erheblicher Anstieg kleiner Partikel mit Durchmessern $d_p < 300\,\mathrm{nm}$ beobachtbar, wohingegen der Anteil der großen Partikel mit Durchmessern $d_p > 500\,\mathrm{nm}$ unbeeinflusst blieb. Der Gesamtanteil volatiler Partikel war dabei erheblich erhöht (von 20 % auf 70 %). Im Gegensatz zum reinem Wüstenstaub sowie Randgebieten der Aerosolfahne, wo Einfachstreualbeden (SSA) zwischen 0.95 und 0.99 (für 530 nm) gemessen wurden, wurde für das Zentrum der Fahne eine minimale SSA von $\omega_{0,min} = 0.907 \pm 0.027$ ermittelt. Die maximalen Absorptionskoeffizienten für 530 nm betrugen $12.0 \pm 2.6\,\mathrm{Mm}^{-1}$ und stimmen gut mit den Werten von SAMUM-I (Marokko, 2006) überein. Im Gegensatz dazu weichen die in der Aerosolfahne von Dakar gemessenen Ångström Koeffizienten der Absorption $\mathring{a}_{ap}$ mit 2.3–4.5 deutlich von den in Cassablanca gemessenen Werten ab (dort wurden $\mathring{a}_{ap}$-Werte von 1.28 ± 0.28 beobachtet). Sowohl die Größenverteilung als auch chemische Analysen zeigen, dass es sich bei der Mischung von Wüstenstaub mit den urbanen Emissionen ausschließlich um externe Mischungen handelte. Der maximale Rußanteil betrug dabei 1.028 ± 0.434 % Vol. , bzw. $1.33 \pm 0.56\,\mu\mathrm{g/m}^3$. Die damit verbundenen maximalen Imaginärteile des komplexen Brechungsindizes für 530 nm lagen bei $k = 0.0065 \pm 0.0025$, was einer deutlichen Erhöhung zu den im reinen Wüstenstaub gemessenen Werten von $k = 0.001$–0.002 entspricht. Allerdings liegen diese Werte noch innerhalb der natürlichen Variabilität, die für verschiedene Wüstenstäube gemessen wurde. Zusammenfassend lässt sich der durch die Einmischung der Abgasfahne von Dakar entstehenden, signifikanten Veränderungen in den optischen und mikrophysikalischen Wüstenstaubeigenschaften eine lediglich lokale Bedeutung zuordnen.

Chapter 1

Introduction

1.1 Scientific Background

Climate change is an interdisciplinary subject of current political, social and scientific discussion. Besides greenhouse gases, which form the most important and well-known contribution to climate change, aerosols provide the second most relevant contribution to radiative forcing. In contrast to greenhouse gases, the publicity of aerosol effects on climate change is considerably smaller. An aerosol in general is defined as a collection of solid or liquid particles suspended in a gas, which forms a two-phase system (Hinds, 1999). There are various natural and anthropogenic sources of atmospheric aerosols like deserts, the sea surface, volcanic eruptions, fuel combustion and forest fires just to name the most important ones. Furthermore all atmospheric aerosols are modified by the meteorological conditions along their pathway through the atmosphere. According to the different sources and the special meteorological conditions, atmospheric aerosol particles cover a broad diameter range from some nm up to 100 μm (Seinfeld and Pandis, 1996).
To quantify the influence of aerosols on climate change, one has to consider direct and indirect aerosol contributions to radiative forcing. A descriptive overview of these effects is shown in Fig. 1.1:

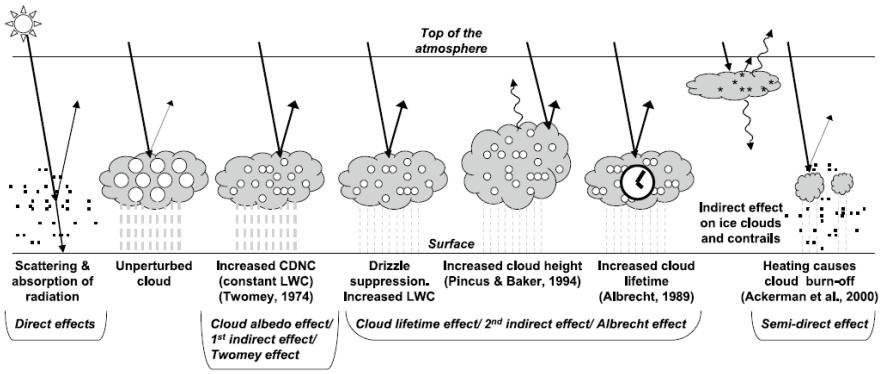

Figure 1.1: Schematic diagram showing the various radiative mechanisms associated without and with cloud effects; adapted from IPCC (2007).

Direct effects are scattering and absorption of incoming solar and outgoing longwave radiation, whereas the indirect effects are assigned to aerosol-cloud-interactions. Cur-

rent scientific literature assess the cloud albedo (Twomey-effect) and the cloud lifetime effects as the two most important indirect effects, but in addition there are a couple of other, less studied, thermodynamic, glaciation and riming effects, which also contribute to radiative forcing (Rotstayn and Penner, 2001; Lohmann and Feichter, 2005). Due to different aerosol sources and modifications in the atmosphere, the chemical, microphysical and optical properties of atmospheric aerosols show large spatial and temporal variations. This fact complicates aerosol classifications and the evaluation of the influence on our climate. The Intergovernmental Panel on Climate Change (IPCC) report 2007 categorizes the following main aerosol types: Sulphate aerosol, organic carbon aerosol from fossil fuels, black carbon from fossil fuels, biomass burning aerosol, nitrate aerosol and mineral dust aerosol.
Within my diploma thesis I will focus on mineral dust and anthropogenic black carbon aerosol. In general mineral dust and black carbon aerosol can scatter sunlight back to space leading to negative radiative forcing and absorb solar and infrared radiation leading to positive radiative forcing (Sokolik and Toon, 1996; Fuller et al., 1999). In contrast to black carbon that acts as a strong absorber for all relevant wavelengths, absorption by mineral dust varies significantly in the visible with highest absorption in the blue. Apart from the climate impact, mineral dust emissions have a direct and indirect influence on human health because of the enhancement of respiratory diseases by inhalation and the long range transport of bacteria and fungi species. Furthermore mineral dust plays a major role in biogeochemical processes by influencing the iron budget of oceanic phytoplankton and presumably also coral reefs (Fung et al., 2000; Shinn et al., 2000; Griffin et al., 2001; Rodriguez et al., 2001). As dust aerosol particles are generated by aeolian erosion in arid and semi-arid regions, there are two main source regions of mineral dust emissions: The North African and the Asian deserts. Thereby the North African desert contributes 50–70 % to the global dust emissions, this is about three to five times the Asian dust input (Tegen and Schepanski, 2009). The global distribution of dust emissions is reflected in maps of the total aerosol optical depth (AOD) as one can see in Fig. 1.2:

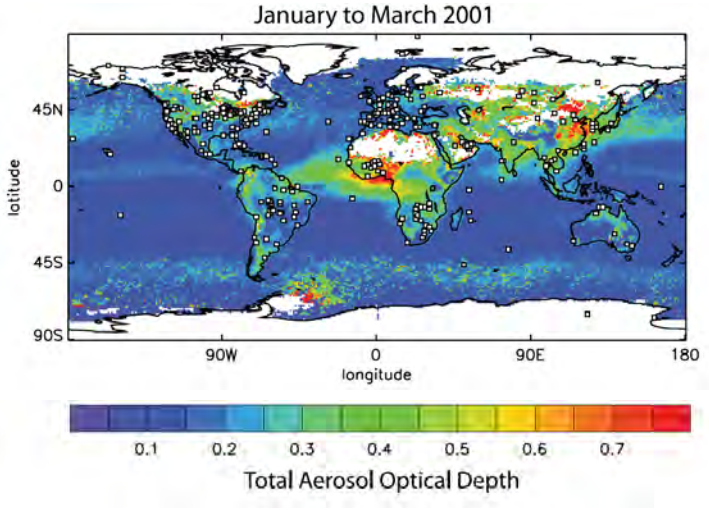

Figure 1.2: Aerosol optical depth at 0.55 μm as determined by the MODIS instrument averaged from January to March 2001 (IPCC, 2007).

Taking into account the high uncertainty of the knowledge about annual global dust emissions (1000–3000 Mt/yr) in general and the high variation of dust properties referring to source regions, it is not surprising that the uncertainty of the aerosol contribution to radiative forcing and climate change did not decrease at all within the development from the third (2001) to the fourth (2007) IPCC report (Heintzenberg, 2009). The main aerosol input needed for calculation of atmospheric radiative transfer in climate models is shown in Fig. 1.3.

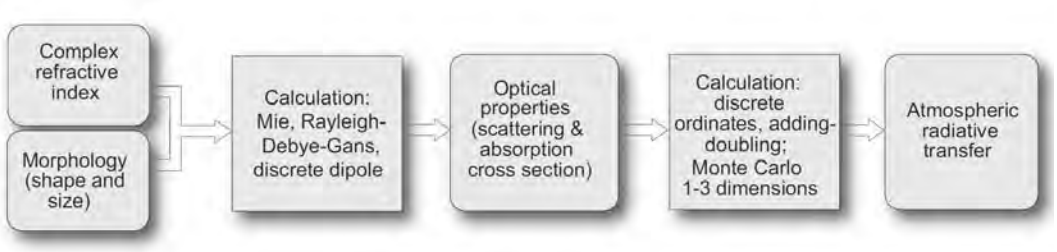

Figure 1.3: Radiative transfer calculation scheme after Bond and Bergstrom (2006).

Measured microphysical properties like size, shape and complex refractive index can be used for Mie/Rayleigh/T-matrix models to calculate optical properties like scattering, absorption and extinction coefficients. Those in turn serve as input for radiative transfer models (Bond and Bergstrom, 2006; Dubovik et al., 2002). In particular Saharan dust has to be studied in detail to improve our scientific understanding, because the North African desert is the world's major dust source. Therefore the **Sa**haran **M**ineral D**u**st Experi**m**ent (SAMUM) research group funded by the German Science Foundation (DFG) was established. The main target of SAMUM was to study chemical composition, shape morphology, size distribution and optical effects of the mineral dust particles (Heintzenberg, 2009). Therefore different kinds of field observations (airborne, ground-based, remote sensing) were compared to modeling results. A detailed discussion about the results from the different working groups will be published in a special issue in Tellus Series B - Chemical and Physical Meteorology - Vol. 63, 2011.
While the first part, SAMUM-I, focused on the analysis of aerosol properties near source regions (the field campaign took place in Morocco in 2006), SAMUM-II concentrated on the long range transport including a field campaign with an operation base on the Cape Verde Islands in January/February 2008, see Fig. 1.4. In the framework of flights to study the aging of mineral dust layers with biomass burning layers above, my diploma thesis investigates a rarely explored feature of mineral dust, namely the mixing of mineral dust with anthropogenic aerosol from the coastal megacity Dakar. As already described above, the radiative properties of aerosols crucially depend on the absorption properties. In case of dust there is a substantial spectral dependence of light absorbing properties in the visible spectral region with strong absorption in the blue and green spectral range and only very week absorption in the red spectral range. By contrast soot is characterized by significant and constant absorption throughout the visible (Fuller et al., 1999; Bond and Bergstrom, 2006; Mogili et al., 2007). For the direct radiative forcing by (pure) mineral dust aerosol the uncertainty in the refractive index has been identified to be the most important error source (Kahnert et al., 2007). This fact is not astonishing, if one takes into account the complex chemical compositions of mineral dust which show not only great spatial variations due to local geology,

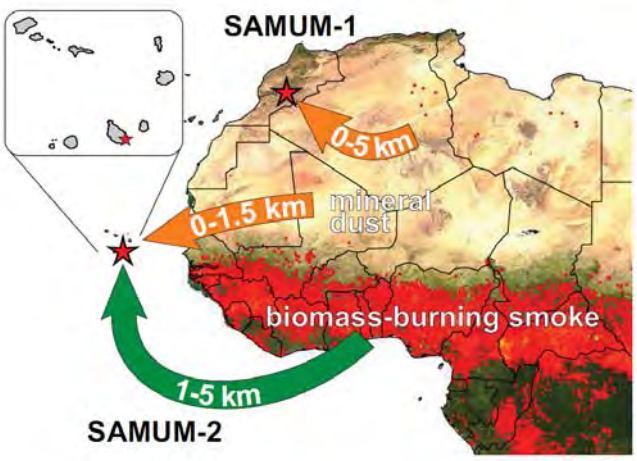

Figure 1.4: SAMUM-I and SAMUM-II field sites (stars) in southern Morocco and at Cape Verde. Pure dust conditions prevailed during SAMUM-I, whereas during SAMUM-II a shallow dust layer up to 1.5 km height (orange arrow, 0–1.5 km) and an extended lofted aerosol layer from 1–5 km height (green arrow) consisting of biomass-burning smoke and mineral dust were frequently observed. The underlying fire map derived from MODIS observations (`http://rapidfire.sci.gsfc.nasa.gov`) shows all fires (red spots) detected during the 21–30 January 2008 period. Figure adapted from Ansmann et al. (2011).

but also temporal differences because of the highly wind speed dependent mobilization processes. In this context the iron fractions and their exact form of appearance play a crucial role for all absorption relevant parameters, because the imaginary part of the refractive index of iron species exceeds those of the other mineral dust components (mainly silicates and quartz) up to some orders of magnitude. Therefore there have been several studies to investigate the impact of chemical compositions on optical and microphysical properties like refractive index, single scattering albedo, asymetry parameter and extinction coefficients (Sokolik and Toon, 1999; Fuller et al., 1999; Kahnert et al., 2007; Lafon et al., 2006; Kandler et al., 2007). Having in mind the described features of mineral dust and black carbon aerosols as single phenomena, the question arises, how and where mixing of the two components occurs in the atmosphere and in which way this mixing influences the optical and physio-chemical properties. The most important mixing processes take place in regions featuring vicinity to urban agglomerations close to mineral dust source regions. This combination can be observed in Asia, where dust from the Gobi and Taklamakan desert is transported over heavily polluted areas, around the Arabian Gulf and along the west coast of Africa. One can imagine that the increase in population in developing countries and migration into cities forces the rapid growth of megacities which boost the anthropogenic emissions in those regions. Therefore the influence of mixing of anthropogenic emissions with mineral dust will remain or even become more relevant within the next decades.
During the last years there have been several field campaigns in the mentioned regions, e.g. TRACE-P (Transport and Chemical Evolution over the Pacific) and ACE-Asia (Aerosol Characterization Experiment) in 2001, as well as SAMUM-I in 2006, which have already provided several of publications in addition to former field experiments

and current laboratory studies (Parungo et al., 1994; Quinn et al., 2004; Clarke et al., 2004; Linke et al., 2006; Petzold et al., 2009). These papers discuss the configuration of optical and microphysical aerosol properties by mixing of dust with anthropogenic emissions at least as side issues. Furthermore Fan et al. (2004) hypothesizes that air pollution increases the scavenging of dust by producing high levels of soluble materials on the dust surface, which makes dust aerosols effective cloud condensation nuclei. However, the level of understanding is still poor and the uncertainties remain quite remarkable.

1.2 Objectives, Aims and Tasks of this Study

While SAMUM-I focused on the mesoscale spatial and temporal impact of anthropogenic emissions in Morocco, but omitted the small-scale analysis of single aerosol plumes, SAMUM-II provides a unique dataset to study the influence of Dakar's anthropogenic aerosol plume on mineral dust properties. In-situ and remote sensing data from two flights on 29 January 2008, which were performed with the DLR research aircraft *Falcon*, form the basis of this study. Taking into account the advantages and limitations of airborne aerosol measurements as well as the recent level of understanding described above, this study focuses on the following key objects:

- How can Dakar's urban pollution plume be characterized referring to aerosol properties and in which way does the mesoscale and local circulation influence the plume structure?
- To what extent does mixing of dust with anthropogenic emissions influence the physico-chemical and optical properties of pure mineral dust?

To explore these key objects, the following parameters will be analyzed:

- Plume characterization and circulation pattern: Lidar backscatter ratio, measured and simulated horizontal and vertical wind patterns
- Microphysical properties: Complex refractive index, size distribution, fraction of volatile particles
- Optical properties: Aerosol optical depth, absorption coefficient, ångstrom coefficient of absorption, single scattering albedo
- Chemical composition: Single particle analyses and volume fraction estimations

At this point it has to be mentioned that I neither participated in the measurements nor in the basic routine data analysis. The remote sensing data analysis was kindly provided by Michael Esselborn, Christoph Kiemle and Andreas Petzold (DLR) and the single particle chemical analyses were provided by Kirsten Lieke and Konrad Kandler (both TH Darmstadt). The task of my diploma thesis was to use the existing basic data from SAMUM-II to develop and accomplish a detailed data analysis for investigation of the key objects mentioned above. Most of the results from this case study will be published in:
Petzold, A., Veira, A., Mund, S., Esselborn, M., Kiemle, C., Weinzierl, B., Hamburger, T., Ehret, G., Lieke, K. and Kandler, K. (2011): *Mixing of mineral dust with urban pollution aerosol over Dakar (Senegal) – Impact on dust physico-chemical and radiative properties. Tellus B, Vol. 63.*

Chapter 2

Theoretical Background

This chapter provides a brief overview of the theoretical background of this thesis. All microphysical and optical aerosol properties, which are part of the subsequent data analysis, are introduced and the basic approaches for their theoretical derivation are provided. Furthermore a short abstract on sea breezes and the model set up of the MM5 (Mesoscale Meteorology Model 5), which is part of the meteorological analysis, will be given.

2.1 Formation, Evolution and Deposition of Aerosols

There are many natural and anthropogenic aerosol sources which have already been presented in the introduction. It is a common classification to divide aerosols into two groups: *primary* aerosol particles, which are introduced directly into the atmosphere and *secondary* aerosol particles that are formed in the atmosphere by chemical reactions, the so called "gas-to-particle conversion" (Hinds, 1999). Usually primary aerosols (mainly dust and sea salt particles) correspond to the micron range due to their mobilization by sufficient surface winds, but beyond that also soot particles from combustion processes which are considerably smaller that $1\,\mu$m belong to primary aerosols. Secondary aerosols arise from complex chemical processes whereupon ion clusters of 1-nm-size serve as precursors for aerosol formation by nucleation. Thereafter condensation and coagulation processes lead to further particle growth. Once an aerosol appears within the atmosphere, it undergoes a specific life cycle that is crucially dependent on meteorological conditions and trace gas concentrations. Evaporation is opposed to hygroscopic growth, which can lead to formation of droplets and wet deposition. In general dry deposition of aerosols is far more efficient for large particles $> 1\,\mu$m than for smaller ones. Raes et al. (2000) provides a detailed description of the evolution of tropospheric aerosol, see Fig. 2.1.

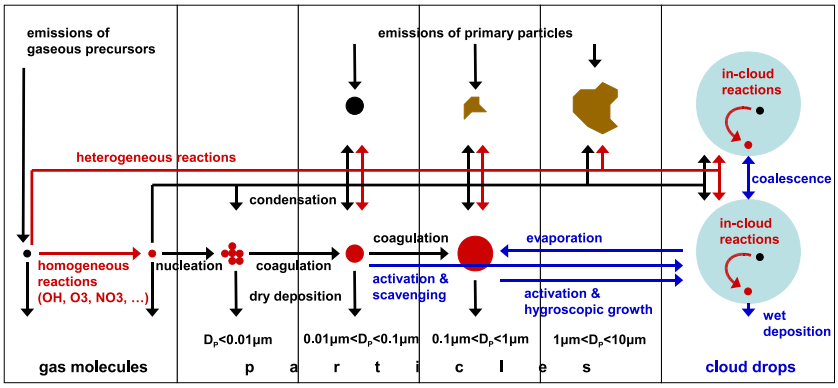

Figure 2.1: Evolution of tropospheric aerosol after Raes et al. (2000) respectively Hamburger (2010).

In order to understand discussions on changes in size distributions and aerosol microphysical properties referring to mixtures of mineral dust and anthropogenic emissions, it is essential to know the basic physics of nucleation, coagulation and deposition processes. The following description of these processes is based on Seinfeld and Pandis (1996) and Hinds (1999).

Nucleation

Nucleation can be described as a problem of aerosol thermodynamics. The key aspect that distinguishes the thermodynamics of aerosols and droplets is their curved interface. Therefore it is useful to describe thermodynamic processes in terms of the Gibbs free energy G, defined as

$$G = U + pV - TS, \tag{2.1}$$

where $U =$ the internal energy of the system, $T =$ temperature, $p =$ pressure, $V =$ volume and $S =$ entropy. To relate the vapor pressure of a curved surface to that over a flat surface, one has to consider the change of Gibbs free energy accompanying the formation of a single drop of radius r_p containing n molecules:

$$\Delta G = G_{droplet} - G_{purevapor}. \tag{2.2}$$

If the initial number of molecules in the vapor phase is N_T, the number of remaining molecules is $N_l = N_T - n$. Defining g_v and g_l as the Gibbs free energy of the vapor and the liquid phase, respectively, the change in Gibbs free energy can be written as follows:

$$\Delta G = N_l g_v + n g_l - N_T g_v + 4\pi r_p^2 \gamma \tag{2.3}$$

The last term of Equation 2.3 represents the free energy related to surface tension γ of a surface with curvature r_p. As an infinitesimal change in g can be expressed in terms of a change in pressure an the volume v_l occupied by a molecule in the liquid phase ($dg = -v_v dp$), integration leads to evaluation of $g_v + n g_l$. After some lines of calculation and the definition of supersaturation $S = \frac{p}{p_0}$ (where p_0 describes the vapor pressure over a flat surface and p is the equilibrium partial pressure over the liquid), the Gibbs free energy change appears to be:

$$\Delta G = -\frac{4}{3}\pi r_p^3 \frac{k_B T}{v_l} \ln S + 4\pi r_p^2 \gamma \tag{2.4}$$

where v_l is the occupied volume by a molecule in the liquid phase. If $S < 1$, ΔG increases monotonically with r_p, whereas values $S < 1$ requires a distinction of two cases: For small values of r_p, ΔG shows similar characteristics as for $S > 1$, but for large values of r_p, ΔG decreases with increasing droplet radius. If one calculates the partial derivative of ΔG to r_p, the maximum Gibbs free energy comes out. This equation can be written as follows and is called *Kelvin equation*:

$$p = p_0 \exp\left(\frac{2\gamma v_l}{k_B T r_p}\right) \tag{2.5}$$

The quintessence from Kelvin equation is that the vapor pressure over a curved interface is always higher than over a flat surface of the same substance. This in turn means that supersaturations are necessary for aerosol nucleation. Furthermore an equilibrium between evaporation and condensation can only occur for supersaturation. In the atmosphere typical precursor gases for nucleation of secondary aerosols are sulphuric acid (H_2SO_4), nitric acid (HNO_3) and ammonia (NH_3) (Seinfeld and Pandis, 1996; Korhonen et al., 1999).

Coagulation

If aerosol particles of similar or different size show motion relative to each other, particle collision can occur. Thus, sometimes particles adhere and form new, larger particles - this process is called *coagulation*. The net result is a decrease in number concentration and an increase in particle size. Depending on the reason for the relative motion, the coagulation is either called *thermal coagulation* (if Brownian motion dominates) or *kinematic coagulation* (if aerodynamic effects are referred to show the major contribution). Starting from Fick's first law of diffusion, Smoluchowski developed a thermal coagulation theory for particles with $d_p \geq 0.1\,\mu$m. The result is an equation for the a rate of change in the number concentration:

$$\frac{dN(t)}{dt} = -K_0 N(t)^2 \tag{2.6}$$

with

$$N(t) = \frac{N_0}{1 + N_0 K_0 t} \tag{2.7}$$

where K_0 is the coagulation coefficient including the diffusion coefficient D:

$$K_0 = 4\pi d_p D \tag{2.8}$$

As the rate of coagulation is proportional to N^2, it is rapid at high concentrations and slow at low concentrations. A very descriptive way to imagine how coagulation evaluates is the calculation of times for number concentrations to halve, see Table 2.1.

Table 2.1: Monodisperse coagulation: Time for number concentrations to halve and particle size to double*. (Adapted from Hinds (1999))

Initial concentration, N_0	Time to reach $\frac{1}{2}N_0$	Time for Particle size to double
10^{14}	20 μs	140 μs
10^{12}	2 ms	14 ms
10^{10}	0.2 ms	1.4 s
10^{8}	20 s	140 ms
10^{6}	33 min	4 h
10^{4}	55 h	16 days
10^{2}	231 days	4 years

* $K_0 = 5 \times 10\,\mathrm{cm}^3/\mathrm{s}$

For a detailed derivation and information about polydisperse aerosol as well as kinematic coagulation, see Hinds (1999).

Deposition

Deposition processes form the sink for atmospheric aerosol and can be divided into two main types: dry deposition and wet deposition. While wet deposition by precipitation forms a very fast and effective scavenging process, time scales of dry deposition are significantly larger. In general the main factors determining dry deposition are particle shape and diameter, chemical composition, atmospheric turbulence and the nature of the surface (Seinfeld and Pandis, 1996). Thereby the process of capturing at the surface is of special interest. Besides Brownian diffusion, interception, impaction and gravitational settling govern the deposition. Feng (2008) provides an extensive comparison of different measurements and model predictions with the particular parameterizations. Pryor and Barthelmie (2000) showed that deposition velocity is a function of wind speed and diameter and dry deposition of fine particles with $0.1\,\mu\mathrm{m} < d_p < 1.0\,\mu\mathrm{m}$ is a very slow process. According to the one-year global average the deposition velocity over continents is about an order of magnitude higher than over oceans for all particle sizes (Nho-Kim et al., 2004). The model results describe only negligible seasonal variations, whereas diurnal variations over land exist with a maximum around 12—15 h local solar time.

The described life cycle of aerosol particles forms the background for aging processes, which appear for all atmospheric aerosols. Thus, also the Saharan mineral dust and the Dakar plume in particular are governed by these processes. Closely related to coagulation and deposition processes are changes in the aerosol size distribution. The exact appearance of the aerosol size distribution in turn has a crucial influence on all optical parameters.

2.2 Aerosol Size Distributions

Atmospheric aerosol particles show a wide range of size diameters covering four to five orders of magnitude. Usually 1 nm is considered to be the lowermost particle diameter, because in terms of kinetics all particles with diameters $d_p < 1$ to 1.5 nm should be categorized as ion clusters (Laakso, 2004). Specifications for the uppermost boundary of atmospheric aerosol particles differ between 10 μm and 100 μm for extremely large particles (Laakso, 2004; Haywood and Boucher, 2000). The fact that the physical and optical properties of aerosols are crucially dependent on particle size calls for a characterization of aerosol size distributions by statistical means. According to Seinfeld and Pandis (1996) and Hinds (1999) we will limit our considerations to spherical particles and neglect effects of non-spherical particle shape. The concept of momentum distribution appears to be an appropriate mean to discuss particle size statistics in general. This concept uses the aerosol distribution function $n\,(d_p)$ to describe the total number of particles N, the total surface area A and the total aerosol volume V, each per cm^3. The meaning of the size distribution function can be interpreted as follows:

$$dN = n(d_p)dd_p = \textit{the number of particles per } cm^3 \textit{ of air having diameters in the range } d_p \textit{ to } d_p + dd_p$$

With this definition of the size distribution function $n\,(d_p)$ the four moments of a size distribution can be expressed as shown in Table 2.2:

Table 2.2: Moments of the size distribution function n(D_p)

Momentum	Formula	Abbreviations
0.Momentum: M_0	$M_0 = \int n\,(d_p)\mathrm{d}d_p$	N
1.Momentum: M_1	$M_1 = \int d_p n\,(d_p)\mathrm{d}d_p$	M_1
2.Momentum: M_2	$M_2 = \int d_p^2 n\,(d_p)\mathrm{d}d_p$	$\frac{A}{\pi}$
3.Momentum: M_3	$M_3 = \int d_p^3 n\,(d_p)\mathrm{d}d_p$	$6\frac{V}{\pi}$

It has been found by experiments that most single-source aerosols can be approximated by a lognormal distribution. The mathematical formula, which describes the particle concentration dN per cm^{-3} and per logarithm diameter interval $dlogD_p$ has the following shape:

$$\frac{dN}{\mathrm{d}logd_p} = \frac{N}{\sqrt{2\pi}logGSD} exp\left(-\frac{(logd_p - logCMD)^2}{2\,(logGSD)^2}\right) \tag{2.9}$$

The CMD is the median diameter of the log-normal distribution and the GSD is the geometric standard deviation, which describes the with of the aerosol size distribution. Thus the GSD is a useful parameter to describe the appearance of an aerosol, because a GSD = 1 indicates monodisperse aerosol, whereas a GSD > 1 reflects a polydisperse aerosol due to the logarithmic size distribution.

Table 2.3: Typical size distribution modes

Mode name	Particle diameter	Process of origin
Nucleation mode	d_p<0.01 μm	condensation from gas phase
Aitken mode	0.01 μm < d_p < 0.1 μm	coagulation and condensation
Accumulation mode	0.1 μm < d_p < 1.0 μm	progressed coagulation
Coarse mode	d_p > 1.0 μm	mechanical generation

Of course, it has to be mentioned that the sum of two or more log-normal distributions usually do not form one new log-normal distribution and there are other approaches to describe those size distributions, e.g. exponential or power-law distributions, see Hinds (1999). But typical mixtures of atmospheric aerosols, which can for example be found in urban air masses, possess a multimodal size distribution. It is a common method to use a four-modal fit to determine those atmospheric aerosol size distributions, in which the different modes can be categorized due to their physical background of appearance. The classification of these four modes and their origin are shown in Table 2.3.

A distinctive nucleation mode usually appears close to boundary layer aerosol sources and in the upper troposphere because nucleation mode particles are converted into Aitken mode particles by coagulation. Considerable accumulation modes are always present in aged aerosols as they are nurtured by aging of the nucleation mode and sedimentation takes place slowly. In contrast, coarse mode aerosol particles feature efficient sedimentation. Therefore they can be found close to source regions of primary aerosols only.

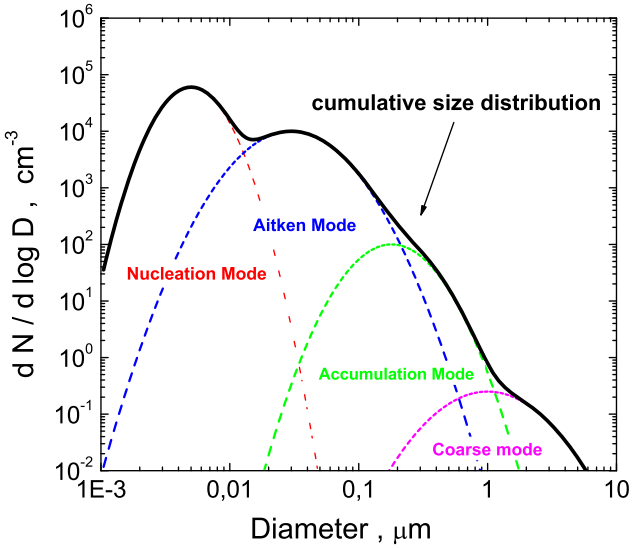

Figure 2.2: Idealized aerosol size distribution with four modes

At this point it is worth mentioning that the large number of Aitken mode particles dominates the number of the total aerosol distribution. In contrast the accumulation mode dominates the surface and, together with the coarse mode, also the volume distribution. An idealized size distribution with four modes can be seen in Fig. 2.2. Due to sedimentation processes the coarse mode tends to disappear far away from sources of large particles and in greater heights. Furthermore rainout and washout are two important processes, which crucially influence all size distribution modes.
Changes in the aerosol size distribution are always connected with changes in the aerosol optical properties, which will be described in the next section. As the theoretical treatment of aerosol optical properties is quite complex, it is useful to consider the optical properties of single aerosol particles at first.

2.3 Aerosol Optical Properties

The following disquisition on aerosol optical properties largely presents an excerpt of Bohren and Huffmans' often-cited work published in 1983. A detailed introduction to the electrodynamic issues is also provided by the most famous standard book of Jackson (1998).

2.3.1 Theory of scattering and absorption of light by aerosol particles

General formulation of the problem

The fundamental problem of scattering and absorption in terms of classical electrodynamics can be verbalized as follows:

"Given a particle of specified size, shape and optical properties that is illuminated by an arbitrarily polarized monochromatic wave, determine the electromagnetic field at all points in the particle and at all points of the homogeneous medium in which the particle is embedded."(Bohren and Huffman, 1983).

As an arbitrary electromagnetic field can be decomposed into its Fourier components, that means into plain waves, we can determine a solution for the given problem as a superposition of several plane waves. Classical electrodynamics says that an electromagnetic field is defined by the electric field $\mathbf{E}$ and the magnetic field $\mathbf{H}$. We can describe the field inside the particle by ($\mathbf{E_1}$,$\mathbf{H_1}$), where the field of the surrounding medium is ($\mathbf{E_2}$,$\mathbf{H_2}$). It describes a superposition of the incident field ($\mathbf{E_i}$,$\mathbf{H_i}$) and the scattered field ($\mathbf{E_s}$,$\mathbf{H_s}$). In terms of wave equations we can write:

$$\mathbf{E}_2 = \mathbf{E}_i + \mathbf{E}_s \tag{2.10}$$

$$\mathbf{H}_2 = \mathbf{H}_i + \mathbf{H}_s \tag{2.11}$$

$$\mathbf{E}_i = \mathbf{E}_o \; exp\,(i\mathbf{k} \bullet \mathbf{x} - iwt) \tag{2.12}$$

$$\mathbf{H}_i = \mathbf{H}_o \; exp\,(i\mathbf{k} \bullet \mathbf{x} - iwt) \tag{2.13}$$

Classical electrodynamics determines these equation to satisfy the Maxwell equations. For the special case of a region with no electrical charges and no currents, such as in a vacuum, the Maxwell equations can be written as:

$$\nabla \bullet \mathbf{E} = 0 \tag{2.14}$$

$$\nabla \bullet \mathbf{H} = 0 \tag{2.15}$$

$$\nabla \times \mathbf{E} = iw\mu\mathbf{H} \tag{2.16}$$

$$\nabla \times \mathbf{H} = iw\epsilon\mathbf{E} \tag{2.17}$$

Taking the curl of 2.16, using the $\nabla (\times\nabla \times \mathbf{E})$ vector identity, 2.17 and 2.14, the vector wave equations 2.18 and 2.19 arise. The denoted form uses the wave vector k instead of the frequency ω, whereupon $k^2 = \omega^2\epsilon\mu$.

$$\nabla^2 \mathbf{E} + k^2 \mathbf{E} = 0 \tag{2.18}$$

$$\nabla^2 \mathbf{H} + k^2 \mathbf{H} = 0 \tag{2.19}$$

As the permitivity ϵ and permeability μ change rapidly at the boundary between particle and medium, one has to take a closer look at these discontinuities. Again classical electrodynamics determines the solution of this problem by forcing the tangential components of $\mathbf{E}$ and $\mathbf{H}$ to be continuous across the boundary:

$$[\mathbf{E}_2 (\mathbf{x}) - \mathbf{E}_1 (\mathbf{x})] \times \hat{\mathbf{n}} = 0 \tag{2.20}$$

$$[\mathbf{H}_2 (x) - \mathbf{H}_1 (x)] \times \hat{\mathbf{n}} = 0 \tag{2.21}$$

where $\hat{\mathbf{n}}$ is directed normal to the boundary surface and $\mathbf{n}$ lies on the surface. The next step is to define a convenient rectangular Cartesian coordinate system, where the direction of the incident light $\hat{\mathbf{e}}_z$ (forward direction) and the scattering direction $\hat{\mathbf{e}}_r$ form the scattering plane (see Fig. 2.3).

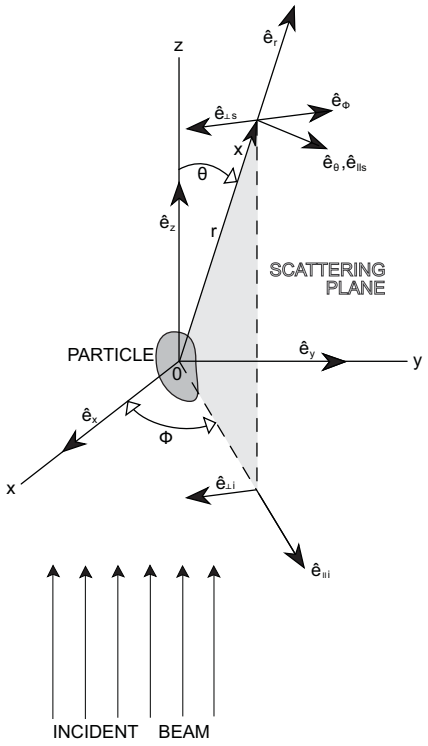

Figure 2.3: Coordinate system for scattering plane, analogous to Bohren and Huffman (1983).

Furthermore, it turns out to be useful to split the incident and scattered fields into one component perpendicular (index $\perp$) and one parallel (index $\parallel$) to the scattering plane. Usually one can assume to neglect the near field and concentrate on the far-field approximation, which is suitable for $kr >> 1$. That means the scattered electric field $\mathbf{E}_s$ is approximately transverse and, by defining $\hat{\mathbf{e}}_{r_\perp} \bullet \hat{\mathbf{e}}_r = 0$, it has the asymptotic form:

$$\mathbf{E}_s \propto \frac{e^{ikr}}{-ikr}\, \hat{\mathbf{e}}_{r_\perp} \qquad kr >> 1, \tag{2.22}$$

Taking into account the boundary conditions 2.20 and 2.21 and making some effort on transformation, the electric field components of the scattered field can be written in matrix form

$$\begin{pmatrix} \mathbf{E}_{\parallel s} \\ \mathbf{E}_{\perp s} \end{pmatrix} = \frac{e^{ik(r-z)}}{-ikr} \begin{pmatrix} S_2 & S_3 \\ S_4 & S_1 \end{pmatrix} \begin{pmatrix} \mathbf{E}_{\parallel i} \\ \mathbf{E}_{\perp i} \end{pmatrix} \tag{2.23}$$

An exact derivation and discussion of all elements S_j of the scattering matrix goes beyond the scope of this more experimentally oriented diploma thesis, but nevertheless it is important to mention the general dependence of S_j on the scattering angle θ and the azimuthal angle ϕ. Furthermore on the one hand Equations 2.10 to 2.19 form the basis for the derivation of absorption and scattering by a single sphere, which favorable derivation requires a spherical coordinate system using spherical Bessel functions. On the other hand 2.22 is essential to obtain the scattering cross section C_{sca} and its absorption cross section C_{abs}, which present more practical tools in aerosol physics. In particular the scattering cross section is an important parameter for optical measurement techniques, which were used within this case study.
The extinction, scattering and absorption cross section are defined as follows:

$$C_{ext} = \frac{W_{ext}}{I}, \quad C_{sca} = \frac{W_{sca}}{I}, \quad C_{abs} = \frac{W_{abs}}{I}, \tag{2.24}$$

where $W_{ext} = W_{abs} + W_{sca}$. Thereby W_{abs} is the ratio of energy absorbed and W_{sca} the ratio of energy scattered, respectively. Furthermore I describes the scattering irradiance. Taking energy considerations as a starting point, the so called *Pointing vector* S, which is a complex parameter that specifies the rate the magnitude and direction of transfer of electromagnetic energy, serves as the key parameter.

$$\mathbf{S} = \mathbf{E} \times \mathbf{H} \tag{2.25}$$

Using the time averaged Poynting vector $\bar{S}$ one can consider the net rate of electromagnetic energy W crossing a surface A, for a detailed derivation see Bohren and Huffman (1983).

$$W = W_i - W_{sca} + W_{ext} \tag{2.26}$$

$$W_i = -\int_A \mathbf{S}_1 \cdot \hat{\mathbf{e}}_{r_\perp} dA, \quad W_{sca} = -\int_A \mathbf{S}_{sca} \cdot \hat{\mathbf{e}}_{r_\perp} dA, \quad W_{ext} = -\int_A \mathbf{S}_{ext} \cdot \hat{\mathbf{e}}_{r_\perp} dA, \tag{2.27}$$

whereas W_i drops out for a non absorbing medium. Formulating a vector scattering amplitude $\mathbf{X}$ out of the ϕ- and θ- dependent $\mathbf{S}_i$ as follows

$$\mathbf{X} = (S_2 cos\phi + S_3 sin\phi)\,\hat{\mathbf{e}}_{\parallel s} + (S_4 cos\phi + S_1 sin\phi)\,\hat{\mathbf{e}}_{\perp s} \tag{2.28}$$

the basic equations for C_{ext} and C_{sca} appear to be:

$$C_{ext} = \frac{4\pi}{k^2} Re\left\{(\mathbf{X}\cdot\hat{\mathbf{e}}_x)_{\theta=0}\right\} \tag{2.29}$$

$$C_{sca} = \int_0^{2\pi}\int_0^{\pi} \frac{|\mathbf{X}|^2}{k^2} sin\theta\; d\theta\; d\phi = \int_{4\pi} \frac{|\mathbf{X}|}{k^2}\; d\Omega \tag{2.30}$$

The scattering and absorption cross sections are fundamental parameters for the theoretical treatment of the complex refractive index, which will be discussed in the framework of Mie theory.

Mie theory - Scattering and absorption of light by a single spherical particle

A theoretical and comprehensive characterization of scattering and absorption of light by single spherical particles has already been published more than 100 years ago by Gustav Mie(Mie, 1908). Even if parts of his calculations had been developed by Lorenz some years before, Mie's work is a milestone in atmospheric physics and the application of Mie theory is particularly relevant for this thesis, too. A huge part of the data analysis due to optical and physico-chemical properties is based on the so called *PSAP data analysis scheme* (see Chapter 3.2.2) which includes the implementation of the well-known numerical Mie code "Bh Mie" (Bohren and Huffman, 1983). Therefore I will provide a short summary of the important results from Mie theory in this chapter.

Starting point for the derivation of the electric and magnetic field vectors of scattering and absorption are the wave equations of a time-harmonic electromagnetic field (**E**,**H**), which we derived above according to Equation 2.18 and 2.19. As we have already shown, the rough procedure to deduce the scattering and extinction cross section C_{sca} and C_{ext}, we can follow up the derivation of these parameters. Taking into account that C_{sca} and C_{ext} are now independent of the azimuthal angle ϕ due to the symmetry of rotation, spherical polar coordinates provide an adequate mean for further calculations. The surface spherical harmonics in terms of the associated Legendre functions of first kind $P_n^m(\cos\theta)$ of degree n and order m lead to spherical Bessel functions and after several lines of calculation the following formula for C_{sca} and C_{ext} appears:

$$C_{ext} = \frac{2\pi}{k^2}\sum_{n=1}^{\infty}(2n+1)\,Re\left\{a_n + b_n\right\}, \tag{2.31}$$

$$C_{sca} = \frac{2\pi}{k^2}\sum_{n=1}^{\infty}(2n+1)\left(|a_n|^2 + |b_n|^2\right), \tag{2.32}$$

where the scattering coefficients a_n and b_n are defined as 2.33 and 2.34 for the case of taking the permeability of the particle and the surrounding medium the same:

$$a_n = \frac{m\psi_n(mx)\,\psi_n'(x) - \psi_n(x)\,\psi_n'(mx)}{m\psi_n(mx)\,\xi_n'(x) - \xi_n(x)\,\psi_n'(mx)} \tag{2.33}$$

$$b_n = \frac{\psi_n(mx)\,\psi_n'(x) - m\psi_n(x)\,\psi_n'(mx)}{\psi_n(mx)\,\xi_n'(x) - m\xi_n(x)\,\psi_n'(mx)} \tag{2.34}$$

m describes the complex refractive index in terms of the refractive index of the surrounding medium m_m and the refractive index of the particle m_p:

$$m = \frac{m_p}{m_m} = n + ik \tag{2.35}$$

whereas the size parameter x is a modified ratio of the particle size (respectively the particle diameter d_p) and the wavelength of the incident wave:

$$x = \frac{\pi N_m d_p}{\lambda} \tag{2.36}$$

If any particle is absolutely non-absorbing, the imaginary part of m disappears and the refractive index of the surrounding medium air can be assumed as $N_m \approx 1$ (Ciddor, 1996).
To depict the major results from Mie theory in a more descriptive way, one should take a look at scattering irradiance calculations referring to different scattering angles, particle sizes and wavelengths. Taking into account these variable parameters, the symmetry of backward and forward scattering turns out to vary significantly. For wavelengths in the visible, scattering intensities for small particles with diameters $d_p < 100\,\text{nm}$ are to a large extent symmetric in forward and backward scattering, whereas the scattering intensity of particle diameters $d_p \geq 1\,\mu\text{m}$ becomes more and more unsymmetric and forward. A graphical description of these results is shown in Fig. 2.4.

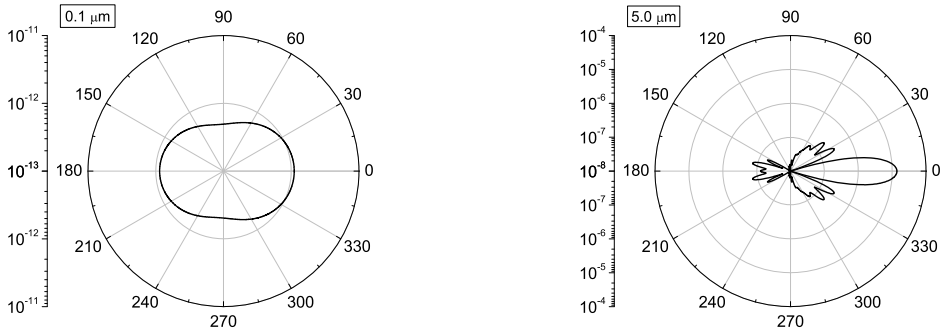

Figure 2.4: Angle-dependent scattering intensity for two spherical dust particles (refractive index m = 1.553 + 0.0024). The scattering intensity of particle 1 is based on a diameter of 0.1μm (left figure), Particle 2 has a diameter of 5.0 μm (right figure).

The tendency that the scattering intensity is symmetric in forward and backward scattering for very small particles forces the idea that simplifications to Mie theory are available for special assumptions. Already more than 100 years ago the wavelength dependence of scattering intensity for very small particles (like air molecules) had been found to show the following wavelength dependence (*Rayleigh theory*):

$$I \propto \frac{1}{\lambda^4}. \tag{2.37}$$

In terms of Mie theory this means: for Size parameters $x << 1$ the *Rayleigh theory*, a modification of the Mie theory, is applicable. A size parameter $x << 1$ implicates that the particle diameter is small compared to the incident wavelength. In terms of visible light, the Rayleigh regime is applicable for particle diameters $d_p < 0.1\,\mu$m, that means for fine mode aerosol particles.

2.3.2 Optical properties of mixed aerosol compositions

The last subsection dealt with scattering and absorption of single particles. Of course Mie theory is applicable for all spherical aerosol particles, but the investigation of a bulk of several aerosol particles requires a different approach. Atmospheric aerosols exist (nearly) unexceptional of polydisperse size distributions, but furthermore, the chemical composition varies significantly within every size distribution. This leads to the need of considering an effective refractive index for a bulk of different particles instead of a single refractive index. Chýlek et al. (1988) studied different approximations to calculate an effective refractive and verified these by detailed laboratory experiments. Based on an aerosol consisting of spherical particles of a non-absorbing matrix and a small amount (1.6 and 2.7 % by volume v) of highly absorbing inclusions. Among others, he tested simple schemes like the volume average of refractive indices (see Equation 2.38), the volume average of dielectric constants (2.39) and different "*Maxwell-Garnett*" mixing rules for two materials (index $_0$ and $_a$), of those only one (the acrylic matrix with water inclusions) is shown (2.40):

$$m_{c(ref)} = v_0 m_0 + v_a m_a \tag{2.38}$$

$$m_{c(die)} = \sqrt{v_0 m_0^2 + v_a m_a^2} \tag{2.39}$$

$$m_{c(max)} = \sqrt{m_0^2 \frac{m_a^2 + 2m_0^2 + 2v_a\left(m_a^2 - m_0^2\right)}{m_a^2 + 2m_0^2 - v_a\left(m_a^2 - m_0^2\right)}} \tag{2.40}$$

Chýlek's results show that neither the volume average of refractive index nor the volume average of dielectric constants shows reasonable agreement with measured data, whereas the Maxwell-Garnett approach is in eligible agreement with the experimental data. According to the dominant aerosol species (dust and soot, respectively) discussed in this thesis, the refractive indices for quartz, hematite (iron oxides, FeOx) and for soot are presented in Fig. 2.5; data for hematite and quartz are adapted from Sokolik and Toon (1999), soot data is related to Shettle and Fenn (1979). This figure gives a good impression of the general problem of mixing dust and soot aerosol.

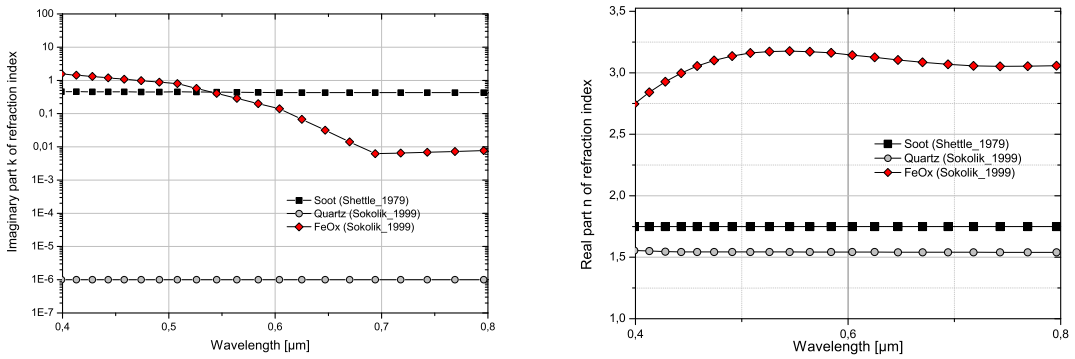

Figure 2.5: Wavelength dependency of the imaginary part (left) and real part (right) of the complex refractive index for soot (Shettle and Fenn, 1979), quartz and iron oxide (Sokolik and Toon, 1999)

As already discussed in the introduction, soot serves as a strong absorber for all relevant wavelengths, whereas absorption for quartz is very small ($k = 10^{-6}$) in this interval. Hematite possesses a significant decrease of k in the discussed spectrum. Although the real part of the refractive index n does not vary about six orders of magnitude as the imaginary index k does, all three components are clearly distinguishable due to their spectral characteristics. At this point it has to be mentioned that the refractive index of mixtures containing dust and black carbon aerosol is crucially dependent on the exact appearance of the elemental carbon. As aerosol particles in general take many different shapes and aggregates, the effects of internal and external mixtures as well as coating processes lead to significant differences in the optical properties (Jacobson, 2000; Fuller et al., 1999).

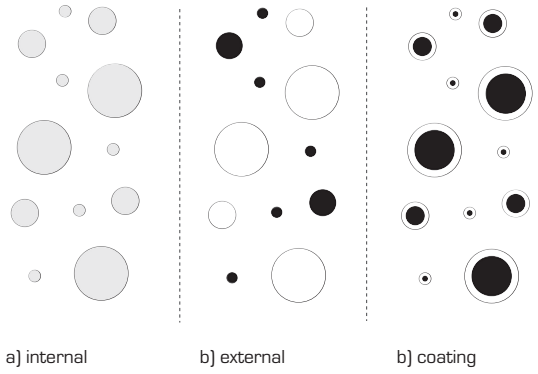

Figure 2.6: Different types of aerosol mixtures: *a*) homogeneous internal mixture, *b*) external mixture, *c*) heterogeneous internal mixture (coating) after Bond and Bergstrom (2006).

Figure 2.6 shows a simple illustration of the basic states of mixing. Pure internal mixtures describe a state of mixing, where the single aerosol components form a completely new and homogeneous type of aerosol particles. Coatings provide a state of heterogenous mixing in which particles of one type inhere in others and form new, but

heterogeneous particles, where both species form two separated fractions. Usually coatings belong to internal mixtures (Bond and Bergstrom, 2006). In contrast to internal mixing, all particles in external mixtures maintain their shape and size.

2.3.3 Optical parameters for particle ensembles

For a bulk of aerosol particles, it is useful to define a new parameter, the extinction coefficient σ_{ep}. In case of a monodisperse aerosol with a particle number concentration of N particles per volume with diameter d_p, the extinction coefficient is defined as follows:

$$\sigma_{ep} = NC_{ext} = \frac{\pi d_p^2 N}{4}\, Q_{ext}, \tag{2.41}$$

with the extinction efficiency Q_{ext}

$$Q_{ext} = 4\frac{C_{ext}}{\pi d_p^2 N}. \tag{2.42}$$

Furthermore it is useful to define a scattering coefficient σ_{sp} and an absorption coefficient σ_{ap}. Thus the extinction coefficient can be described as sum of σ_{sp} and σ_{ap}:

$$\sigma_{ep} = \sigma_{sp} + \sigma_{ap} \tag{2.43}$$

Of course atmospheric aerosols are hardly ever mononodisperse. For a polydisperse aerosol integration over all particle diameters is necessary. Because of the log-normal form of size distributions the extinction coefficient takes the following form:

$$\sigma_{ep} = \int_{d_p} \frac{\pi D_p^2}{4}\, Q_{ext}\, \frac{dN}{d\,\log d_p} d\,\log d_p \tag{2.44}$$

Again the scattering and the absorption coefficient can be calculated analogously.
The extinction coefficient σ_{ep} serves as a key parameter to determine the attenuation of light referring to aerosol scattering and absorption effects. If σ_{ep} varies with height, one has to integrate σ_{ep} vertically to determine the overall attenuation. This leads to the definition of the aerosol optical depth (AOD), which describes the exponent of the Lambert-Beer law for a general case:

$$I = I_0\, e^{-AOD} \qquad\qquad AOD = \int_{h_2}^{h_1} \sigma_{ep}\,(z)\, dz, \tag{2.45}$$

Another optical parameter which has been established during the last few years is the so called *Ångström exponent of absorption*. The original meaning of the Ångström exponent results from the fact that, for a small interval of wavelength, the extinction coefficient can be approximated by the Ångström exponent of extinction:

$$\sigma_{ep} \;\propto\; \lambda^{-\mathring{a}_{ep}} \tag{2.46}$$

with the Ångström exponent of extinction $\mathring{a}_{ep}$ (Ångström, 1964). Within this thesis only the aerosol absorption ångstroem coefficient will be part of the data analysis. For a small interval of wavelength with a lower border λ_2 and an upper border λ_1 the aerosol absorption Ångström coefficient is defined as

$$\mathring{a}_{ap} = \frac{\ln \frac{\sigma_{ap}(\lambda_1)}{\sigma_{ap}(\lambda_2)}}{\ln \frac{\lambda_1}{\lambda_2}} \tag{2.47}$$

describing the approximated wavelength dependence of σ_{ap}:

$$\sigma_{ap} \;\propto\; \lambda^{-\mathring{a}_{ap}} \tag{2.48}$$

The aerosol absorption Ångström exponent $\mathring{a}_{ap}$ in general depends on the size distribution of the aerosol and the spectral dependence of the refractive index. Common values of $\mathring{a}_{ap}$ for biomass burning and combustion aerosol range from 1 to 3 for wavelengths between 300 nm to 1000 nm (Kirchstetter et al., 2004; Bergstrom et al., 2007). Because of the spectral height dependence of the imaginary part of the refractive index for iron minerals, the absorption Ångström exponent of pure Saharan dust aerosol covers a wide range from $\mathring{a}_{ap} \approx 3.5$ to values $\mathring{a}_{ap} > 7$ (Petzold et al., 2009; Linke et al., 2006). If not explicitly noticed, $\mathring{a}_{ap}$ in this work is calculated for $\lambda_1 = 660$ nm and $\lambda_2 = 467$ nm.

In connection with extinction and scattering coefficients also the single scattering albedo ω_0 (sometimes referred as "SSA") is mentionable as I will discuss this parameter in my data analysis. Besides the extinction coefficient, the single scattering albedo is the most important factor for the shortwave radiative forcing (IPCC, 2007) and describes the fraction that scattering has in extinction:

$$\omega_0 = \frac{\sigma_{sp}}{\sigma_{sp} + \sigma_{ap}} = \frac{\sigma_{sp}}{\sigma_{ep}} \tag{2.49}$$

Due to its dependence on σ_{sp} and σ_{ap}, ω_0 features a significant wavelength dependency, whereupon ω_0 increases with increasing wavelength. Within the framework of aerosol physics the single scattering albedo is usually discussed for wavelengths in the visible, but there are also publications, which touch single scatterings albedos of the near infrared (Bergstrom et al., 2007). According to Mie theory, ideal spherical combustion aerosol particles of 100 nm should have an ω_0 of approximately 0.1 for wavelengths between 450–650 nm, but typically measured values for ω_0 reach from 0.2 up to 0.3 (Bond and Bergstrom, 2006). In contrast to carbonaceous particles, mineral dust particles have much higher single scattering albedos for the mentioned wavelengths. Most recent publications provide values for ω_0 reaching between 0.90 and 0.99 depending on the origin of the aerosol and the state of pollution with carbonaceous fine mode particles (Todd et al., 2007; Linke et al., 2006; Quinn et al., 2004), but referring to Rasp (2007) even lower SSAs down to 0.75 for $\lambda \leq 500$ nm have been measured for Saharan dust aerosol.

2.4 Sea Breezes

All optical properties of the Dakar plume discussed above are sensitive to dilutions processes and thus they depend on the development of the plume structure which is determined by the meteorological conditions. For the special case of coastal regions the local circulation is often influenced by sea breeze circulations. As the urban area of Dakar is not only sited along the coast line, but on a peninsula, this phenomenon is worth a brief discussion.
Sea breezes are mesoscale (2–2000 km) phenomena, which appear along costs all over the world and show many facets like transport of aviation, pollen and air quality (Simpson, 1994; Miller et al., 2003). Especially the latter effect is a very well studied feature of sea breezes, because many growing metropolitan areas are located at the coast (Raynor et al., 1979; Melas et al., 1995; Gaza, 1998; Freitas et al., 2007; Lemonsu et al., 2006). Many of these studies provide both, detailed field experiments and numerical modeling. In this chapter I want to present a brief overview of the phenomena as such and mathematical approaches to describe these. Miller et al. (2003) defined a sea breeze system (SBS) as follows:

> *"Sea breeze circulation (SBC) is a vertically rotating mesoscale cell, with shoreward flow near earth's surface, rising air currents inland, diffuse sinking currents several kilometers out to sea, and (usually) seaward return flow near 900 hPa."*

The basic inducement for a sea breeze is always a temperature gradient between the hot land and the cool sea surface, that means a sea breeze is a mesoscale thermally induced wind due to differential heating (Simpson, 1994; Bouchlaghem et al., 2007). Referring to the definition of the sea breeze, Miller et al. (2003) designed a simplified schematic that can give an impression what a typical sea breeze looks like, see Fig. 2.7.

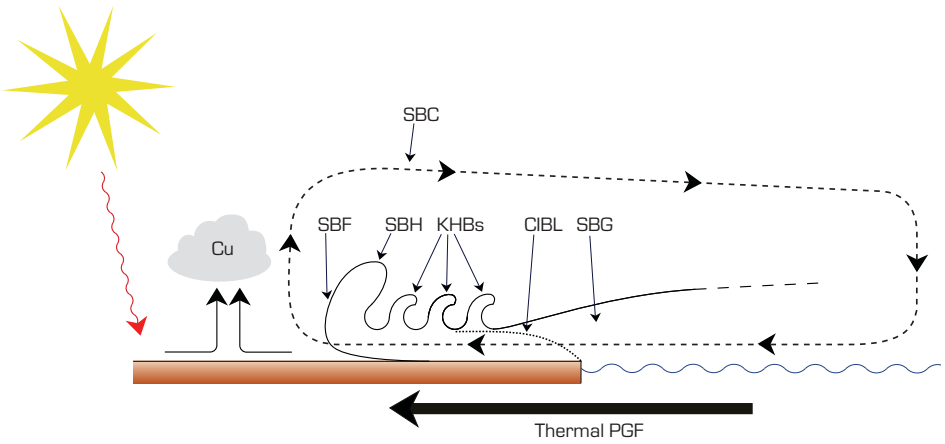

Figure 2.7: Schematics of a sea breeze system after Miller et al. (2003), see text for detailed description of given labels.

The abbreviations used in Fig. 2.7 are:

- SBC = Sea breeze circulation: see definition above
- SBG = Sea breeze gravity current: landward flow of cool, moist air
- SBF = Sea breeze front: landward edge of the SBG, often associated with sharp changes in temperature, moisture and wind
- SBH = Sea breeze head: raised head behind SBF, twice as high as the following feeder flow
- KHBs = Kelvin-Helmholtz billows: instability waves along upper boundary
- CIBL = Convective internal boundary layer: unstable region within the marine air mass

It hast to be noted, that the arrows which mark the "direction" of the sea breeze circulation in Fig. 2.7 are not necessarily equivalent to referring wind directions, because except for tropical regions and very small scale breezes, the Coriolis force leads to a rotation towards a coastline parallel flow.
In the following, a short abstract of the theoretical description of sea breezes will be given. The basic ideas follow Holton (2004).

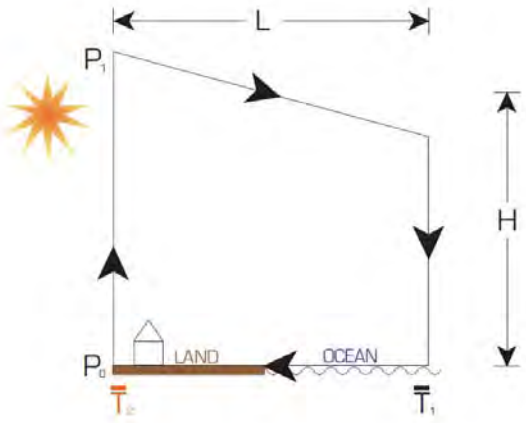

Figure 2.8: Schematics of a sea breeze system, the integration path for Equation 2.50 is indicated by arrows along the pathway; schematics was drawn after Holton (2004).

Fig. 2.8 shows a simplified pattern of the circulation. Due to diurnal variations based on a faster warming of land during daytime, the mean temperature of the air over the ocean is colder than over land. $\bar{T}_2$ and $\bar{T}_1$ are the surface temperatures over land respectively over sea, H describes the circulation height and L the cross shore length. Thus, if the pressure can be assumed to be uniform at ground level, the isobaric surfaces several hundred meters above the ground will slope downward towards the ocean. Simultaneously, the surfaces of constant density (isopycnic surfaces) will slope downward towards the land Holton (2004). Describing Fig. 2.8, it is reasonable to pick up

Bjerknes Circulation Theorem (Thorpe et al., 2003), which defines the circulation C as:

$$\frac{DC}{Dt} = -\oint \frac{1}{\rho} dp \tag{2.50}$$

using Kelvin's definition of the Circulation

$$C = \oint \mathbf{u} \cdot d\mathbf{l}. \tag{2.51}$$

In our special case of the sea breeze circulation, the path of integration is chosen along lines of constant pressure p_1 and p_0 in the land-ocean direction. Therefore, due to the definition of the temporal derivative of the circulation 2.50, only the vertical integration paths are non-zero. Assuming the validity of the ideal gas law, the resulting rate of increase in the circulation, is

$$\frac{DC}{Dt} = R\ ln\left(\frac{p_0}{p_1}\right)\left(\bar{T}_2 - \bar{T}_1\right) > 0. \tag{2.52}$$

Defining the mean tangential velocity along the circuit as follows:

$$\bar{U} = \frac{C}{2\left(H + L\right)}. \tag{2.53}$$

The temporal derivative of the tangential velocity appears to be

$$\frac{D\bar{U}}{Dt} = \frac{Rln\left(\frac{p_0}{p_1}\right)\left(\bar{T}_2 - \bar{T}_1\right)}{2\left(H + L\right)}. \tag{2.54}$$

Due to the simplicity of this 2-dimensional model neglecting non-linear effects as well as friction, this model overestimates the wind speeds one hour after onset of the breeze by a factor of 2–4 (Holton, 2004). Nowadays local circulation models with complicated boundary layer turbulence and land surface parameterizations provide handy tools for simulations of land-sea breezes.

2.5 Description of the MM5 Model

In the framework of the meteorological analysis within this case study, it turned out to be useful to run a mesoscale numerical circulation model because of the occurrence of a small scale sea breeze. Therefore the **M**esoscale **M**eteorology Model **5** (MM5) was chosen for further investigation. The modeling with the MM5 will provide substantial information for the understanding of this case study. As I will not provide any sensitivity studies or developments of new model tools, this chapter should solely serve as a brief description of the model structure which was developed by Grell et al. (1995). Specific information about the boundary layer parameterizations can be found at Troen and Mahrt (1986), Hong and Pan (1996) and Shafran et al. (2000). Furthermore descriptive explanations of the fundamental model structure are provided by Thomsen (2006) and Dudhia et al. (2005).
The spatial model build-up consists of a horizontal Cartesian x-y-grid and a vertical grid realized in σ-coordinates. With pressure p, surface pressure p_s and upper boundary pressure p_t (100 mb, assumed to be constant), they appear as follows:

$$\sigma = \frac{p - p_t}{p_s - p} \tag{2.55}$$

Sigma coordinates provide substantial advantages, because they follow the terrain and they have simple vertical boundary conditions ($\sigma_s = 1$ and $\sigma_t = 0$). They are realized on a Lorenz-grid, where the vertical velocities are calculated halfway in between the full σ-layers. The horizontal grid is realized as a B-grid, see Fig. 2.9 (Arakawa and Messinger, 1976). A more precise and graphic description for the specific grids used in our model set-up will follow in Chapter 3.2.3.

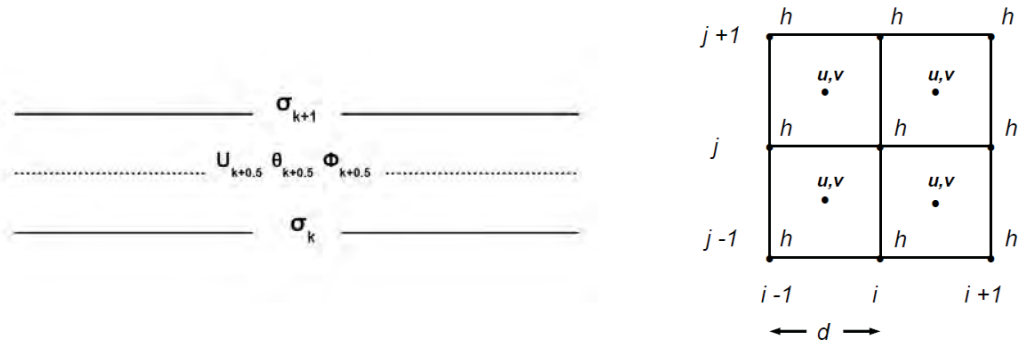

Figure 2.9: Vertical (left) and horizontal (right) grid configuration for a Lorenz and a B-grid, respectively.

To derive the basic equation used for the non-hydrostatic model, one has to consider a constant reference state (indicated by $_0$) in p, T and ρ and corresponding perturbations (indicated by $'$):

$$T(x, y, \rho, t) = T_0(z) + T'(x, y, \rho, t), \tag{2.56}$$

$$p(x, y, \rho, t) = p_0(z) + p'(x, y, \rho, t) \tag{2.57}$$

and

$$\rho\left(x,y,\rho,t\right)=\rho_0\left(z\right)+\rho'\left(x,y,\rho,t\right) \tag{2.58}$$

The derivation of the pressure and momentum equations for the perturbation parameters requires some lines of calculation and is not merely a difficult, but a time-consuming work. This procedure leads to the following equations of the MM5 model (Thomsen, 2006; Grell et al., 1995). The pressure equation is given by:

$$\frac{\partial p'}{\partial t}-\rho_0 g w+\nu p\nabla\cdot\vec{v}=-\vec{v}\cdot\nabla p'+\frac{\nu p}{T}\left(\frac{\dot{Q}}{c_P}+\frac{T_0}{\theta_0}D_\theta\right). \tag{2.59}$$

Defining $p^*=p_s-p_t$ the three equations of momentum can be written as:

$$\frac{\partial u}{\partial t}+\frac{\mathrm{m}}{\rho}\left(\frac{\partial p'}{\partial x-\frac{\rho}{p^*}}\frac{\partial p^*}{\partial x}\frac{\partial p'}{\partial\rho}\right)=-\vec{v}\cdot\nabla u+v\left(f+u\frac{\partial \mathrm{m}}{\partial y}-v\frac{\partial \mathrm{m}}{\partial x}\right)-ew\cos\alpha-\frac{uw}{r_{earth}}+D_u \tag{2.60}$$

$$\frac{\partial v}{\partial t}+\frac{\mathrm{m}}{\rho}\left(\frac{\partial p'}{\partial x-\frac{\rho}{p^*}}\frac{\partial p^*}{\partial x}\frac{\partial p'}{\partial\rho}\right)=-\vec{v}\cdot\nabla v+u\left(f+u\frac{\partial \mathrm{m}}{\partial y}-v\frac{\partial \mathrm{m}}{\partial x}\right)-ew\sin\alpha-\frac{vw}{r_{earth}}+D_v \tag{2.61}$$

$$\frac{\partial w}{\partial t}-\frac{\rho_0}{\rho}\frac{g}{p^*}\frac{\partial p'}{\partial\rho}+\frac{g}{\gamma}\frac{p'}{p}=-\vec{v}\cdot\nabla w+g\frac{p_0}{p}\frac{T'}{T_0}-\frac{gR}{c_p}\frac{p'}{p}+e\left(u\cos\alpha-v\sin\alpha\right)+\frac{u^2+v^2}{r_{earth}}+D_w \tag{2.62}$$

As described above, x and y are components of a Cartesian coordinate system (x is directed eastward, y is directed northward) and $\sigma=1$ equals the earth surface. Furthermore it's worth mentioning several notes about some single terms explicitly:

- D_u, D_v, D_w and D_θ represent the horizontal diffusion which determine effects like nonlinear instability, aliasing and dry convection adjustment just to name so of them.
- The terms r_{earth}, $u\frac{\partial \mathrm{m}}{\partial y}$ and $v\frac{\partial \mathrm{m}}{\partial x}$ represent effects attributed to curvature effects and m is a map-scale factor.
- The last term with parentheses on the right in Equation 2.59 represents a pressure increase due to heating which forces the air to expand. This term is usually negligible and therefore it is not implemented in the model.
- All three equations of motion 2.60 - 2.62 contain the typically neglected component of the Coriolis force, $e=2\ \Omega\cos\lambda$ where λ represents latitude.
- Apart from the given equations, prognostic equations also exist for water vapor and microphysical variables such as cloud and precipitation.

Beside pressure and momentum equation, a prognostic circulation model needs also a thermodynamic equation. The derivations of this thermodynamic equation starts with the gas law and the first law of thermodynamics. One form of the result is as follows:

$$\frac{\partial T}{\partial t}=-\mathbf{u}\cdot\nabla T+\frac{1}{\rho c_p}\left(\frac{\partial p'}{\partial t}+\vec{v}\cdot\nabla p'-\rho_0 g w\right)+\frac{Q}{c_p}+\frac{T_0}{\theta_0}D_\theta \tag{2.63}$$

Furthermore at this point the advection (Equation 2.64) and the divergence term (Equation 2.65) should be specified:

$$\vec{v} \cdot \nabla A \equiv \mathrm{m}u\frac{\partial A}{\partial x} + \mathrm{m}v\frac{\partial A}{\partial y} + \left(-\frac{\rho_0 g}{p^*}w - \frac{m\sigma}{p^*}\frac{\partial p^*}{\partial x}u - \frac{\mathrm{m}\sigma}{p^*}\frac{\partial p^*}{\partial y}v\right)\frac{\partial A}{\partial \theta} \tag{2.64}$$

$$\nabla \cdot \vec{v} = \mathrm{m}^2\frac{\partial}{\partial x}\left(\frac{u}{\mathrm{m}}\right) - \frac{m\sigma}{p^*}\frac{\partial p^*}{\partial x}\frac{\partial u}{\partial \sigma} + \mathrm{m}^2\frac{\partial}{\partial y}\left(\frac{v}{\mathrm{m}}\right) - \frac{m\sigma}{p^*}\frac{\partial p^*}{\partial y}\frac{\partial v}{\partial \sigma} - \frac{\rho_0}{p^*}g\frac{\partial w}{\partial \sigma} \tag{2.65}$$

The pressure and momentum equation together with the thermodynamic equation form the heart of the MM5 (Dudhia et al., 2005). Temporally, a second-order leapfrog time-step scheme is used to calculate these equations, but for some terms it turned out to be convenient to use a time-splitting scheme. Because of the extra terms on the left of the equals sign (the so called *fast terms*) in Equations 2.59 - 2.62, a shorter time step has to be used as these terms are responsible for sound waves. In contrast to that some radiation and cumulus options use a constant tendency over periods of many model time steps and are only recalculated every 30 minutes.

Chapter 3

Instrumentation and Analysis Methods

This chapter is split into a technical description of the methods, by which the data of this case study were measured, and a section about the data analyses methods which were used for investigation. As I did not develop or enhance any measurement or modeling techniques, the first section is only to serve for the understanding of the technical background. The second section of this chapter deals with the data analysis methods used in this thesis and emphasizes those parts of the data analysis which were developed and implemented by myself.

3.1 Instrumentation

The following section provides information on all measurement techniques used for the analysis of the aerosol physico-chemical and optical properties. The measurements described in the following sections were conducted with the Falcon research aircraft operated by Deutsches Zentrum für Luft- und Raumfahrt (DLR). The instrumentation was similar to the experiment SAMUM-1 (Esselborn et al., 2009; Petzold et al., 2009; Weinzierl et al., 2009). In addition to the in-situ equipment a small subsection about HSRL-remote-sensing gives a rough overview of this measurement technique to investigate optical properties of air columns. The described measurement techniques aim to achieve investigation of the following aerosol microphysical and optical key parameters:

- aerosol number concentration
- aerosol size distribution
- volatility of aerosol particles
- absorption and scattering characteristics
- chemical composition of single particles
- aerosol optical depth and extinction

As parameters like the aerosol size distribution cover a large range of particle diameters, one has to combine different measurement techniques to calculate one of the mentioned parameters. Table 3.1 shows an overview of measurement instruments and

the corresponding key parameters with respect to the different size ranges. Detailed information about all instruments mentioned in Table 3.1 are provided in the following section. Furthermore the standard aircraft equipment includes instrumentation for the measurement of the meteorological parameters temperature, relative humidity, pressure and wind speed.

In-situ aerosol measurements aboard an aircraft, which exceeds horizontal velocities of 250m/s, require specific treatment of the aerosol inlet. For this reason a special isokinetic inlet has been constructed for the specifications of the DLR research aircraft Falcon 20 (Fiebig, 2001; Hamburger, 2010). The principle of isokinetic conditions predicts that the aerosol particles passing the inlet follow the streamlines into the sampler. That means that the flow of the gas carrying the particles is not altered by any acceleration caused by the inlet itself (Addlesee, 1980). During the SAMUM-2 campaign, the isokinetic inlet for the instruments DMA, PCASP-100 and FSSP-300 were located in a wing, whereas the isokinetic inlet for the CPCs, CPSAs, OPC and PSAP was placed on top of the Falcon, see Fig. 3.1. For further information about sampling efficiencies, refer to Fiebig (2001). Additionally, the Giant Particle Collector (GPaC) is also mounted in one of the wings and the HSRL is placed in the belly pot. For a detailed description of the aerosol inlets and sampling assembly refer to Weinzierl et al. (2009), and references therein.

Figure 3.1: Photos of the isokinetic inlets used for in-situ aerosol measurements. The left picture shows inlet No.1 placed on top of the Falcon, whereas the right picture demonstrates inlet No.2 under the aircraft wing. See text for further description.

3.1.1 Particle number concentration

The number concentration of aerosol particles is typically measured by use of **C**ondensation **P**article **C**ounters (CPCs), because condensation is the only technique available for detecting gas-borne particles that are too small for detection by optical methods (McMurry, 2000). In principal CPCs consist of three divisions: a saturation chamber, a condenser tube, and the optical detection unit. The CPC determines the integral particle concentration for a large range of particle sizes, determined by the instrument's lower and upper size cut-offs, described below. Typically, a CPC detects particles in the size range between a few nanometers up to a few micrometers, and therefore the entire range of particle sizes that usually determine the atmospheric aerosol number concentration is covered by this instrument (Hinds, 1999). Moreover, continuous CPCs

Table 3.1: Overview of used measurement instruments aboard falcon aircraft during SAMUM-2 field campaign

Instrument	Measurement Physics	Size Range	measured parameter
Condensation Particle Counter			
CPC1 + TD 250	condensation + scattering	$d_p > 10nm$	non-volatile number concentration
CPC2 + TD 250 + DS4	diffusion + condensation + scattering	$d_p > \approx 100nm$	non-volatile number concentration
CPSA1 + TD250 + DS3	diffusion + condensation + scattering	$d_p > \approx 50nm$	non-volatile number concentration
CPSA2	condensation + scattering	$d_p > 10nm$	number concentration
CPSA3	condensation + scattering	$d_p > 4nm$	number concentration
Optical Particle Counters			
PCASP-100 X	Scattering	$0.15\mu m < d_p < 3\mu m$	size distribution
OPC GRIMM 1.129 + TD250	Scattering	$0.25\mu m < d_p < 2.5\mu m$	non-volatile size distribution
FSSP-300	Scattering	$0.3\mu m < d_p < 20\mu m$	size distribution
Absorption Measurement Techniques			
3-λ-PSAP	Deposition + Transmission	$D_p < 2.5\mu m$	absorption coefficient for λ = 467, 530 and 660nm
Impactor Samples			
Two-Stage Miniature Impactors + Giant Particle Collector (GPaC)	Deposition + Electron Microscopy	$0.1\mu m < D_p < 2.5\mu m$	chemical composition of single aerosol particles
Remote Sensing			
HSRL	Scattering + Photodiodes		aerosol optical depth

Abbreviations:
TD250: Thermodenuder (250.C), DSx: Number of diffusion screens

used aboard aircrafts must have a high temporal resolution in the order of seconds and are able to detect particle concentration from 0.01 to 10^5 per cm^3 (Hermann and Wiedensohler, 2001). A comprehensive review of the operating principles and the historical development of Condensation Particle Counters in general is given by McMurry (2000), whereas Hermann and Wiedensohler (2001) and Weigel et al. (2008) yield good descriptions of CPC counting efficiencies at low pressures.

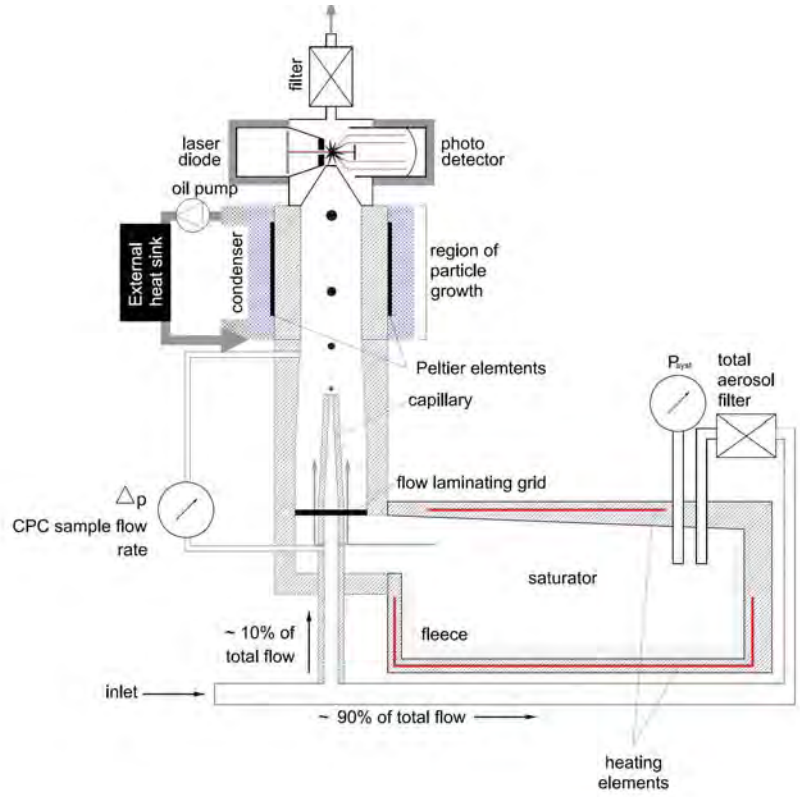

Figure 3.2: Schematics of an aircraft-borne CPC as originally developed by Wilson et al. (1983), figure adapted from Weigel et al. (2008).

Figure 3.2 shows a scheme of a CPC for typical aircraft-born application. The description of this scheme shall help to describe the three divisions of CPC measurement technique by explanation of the aerosol flow within the instrument. Having passed the inlet, the continuous aerosol flow is split into two streams. The sheath flow ($\approx 90\,\%$ of the total flow) comes to pass a filter and enters the saturator block of the CPC, a heated chamber which is saturated with butanol vapour. Downstream the saturator, this pure butanol saturated air is mixed with the actual aerosol flow ($\approx 10\,\%$ of the total flow) and cooled in the condenser block which results in high supersaturation with respect to the butanol vapour. Consequently, the particles grow by butanol condensation to particle diameters of several micrometers. After their growth the enlarged particles enter the optical detection unit where they are counted by a laser-photodiode optics next to the condenser.
When operating aircraft-borne CPCs, two issues need special attention: the pressure-dependent calibration of the lower size cut-off and the pressure-dependent particle

detection efficiency. Besides pressure, both depend on the exact geometry and flow conditions of the instrument. The temperature difference between the saturator and the condenser, the surface structure and the shape of the activated particles define the lower cut-off and the detection efficiency. Several studies have been carried out to characterize these effects (Brock et al., 2000; McMurry, 2000; Hermann and Wiedensohler, 2001; Seifert et al., 2004; Weigel et al., 2008; Giechaskiel et al., 2010).
The performance of a CPC can be characterized by its counting efficiency curve. Counting efficiency curves define the fraction of particles that are detected by the particle counter as a function of particle size. Small particles are only activated with a certain probability, as the curvature of the particle surface raises the equilibrium vapour pressure above the surface (Kelvin effect). The lower particle size cut-off d_{50} is defined as the particle diameter at which 50 % of the particles are activated, whereby the shape of the counting efficiency curve is determined mainly by the supersaturation within the condenser. Due to boundary layer effects and diffusive and phoretic particle losses, the asymptotic maximum counting efficiency is slightly below 100. A typical example of such a curve is given by Fig. 3.3:

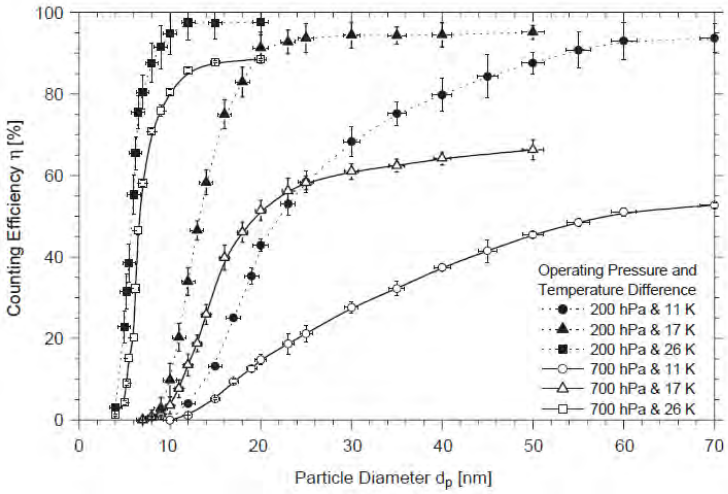

Figure 3.3: Example of a CPC counting efficiency curve. Counting efficiencies of a perfluorotributylamin CPC are presented for 11, 17, and 26 K temperature difference at 200 and 700 hPa operating pressure, respectively. All curves were obtained using H_2SO_4 particles. Adapted from Hermann et al. (2005).

Low pressures and high temperature differences offer the lowest cut-off diameters down to 3–4 nm. This behavior can be explained by theoretical considerations based on the Kelvin effect concerning the particle activation in the condenser (Hermann and Wiedensohler, 2001). At this point I want to abandon a detailed abstract of condensation and particle activation theory and refer to Seinfeld and Pandis (1996) and Giechaskiel et al. (2010).
In order to increase the lower detection limit one can use diffusion screens which are set in front of a CPC. For a detailed description, see Feldpausch et al. (2006). A diffusion screen is composed of several stainless steel meshes placed in the aerosol flow. Due to Brownian motion fine particles collide with the mesh of the diffusion screen and are deposited on the mesh and removed from the aerosol population. As a result only

particles with diameters $d_p > d_{min}$ reach the CPCs. The advantage of connection of 5–10 diffusion screens is the investigation of number concentration between 20 to 80 nm, where single CPCs are disable to measure size resolved.
It should be mentioned that during the SAMUM-II field campaign, the CPC's were operated within a CPC battery of several CPCs partly combined with upstream thermodenuders, which permit a size specific characterization of the mixing state / volatility of aerosol particles in the sub-micron range. For further information, see Subsection 3.1.4. Furthermore special configurations of CPCs allow measurements of particle size distributions in the sub-100 nm range. The so called CPSA (condensation particle size analyzer) consists of three or four CPC with adjustable cut-off diameters which can be set between 3 and 20 nm. The use of CPSAs helps to investigate the nucleation mode by providing number concentrations for differential size bins with a width of some nm.

3.1.2 Size distribution

The equipment used to measure the aerosol size distribution during SAMUM-II is based on two instruments: a **P**assive **C**avity **A**erosol **S**pectrometer **P**robe (PCASP-100) and an **O**ptical **P**article **C**ounter (OPC). The latter was only used in combination with a thermodenuder to investigate volatility aspects. I will concentrate on the PCASP-100, whereupon the basic measurement techniques are quite similar. In general terms, the operating principle of the PCASP and the OPC rests upon Mie theory, which predicts that the intensity of scattered light is proportional to the particle size.

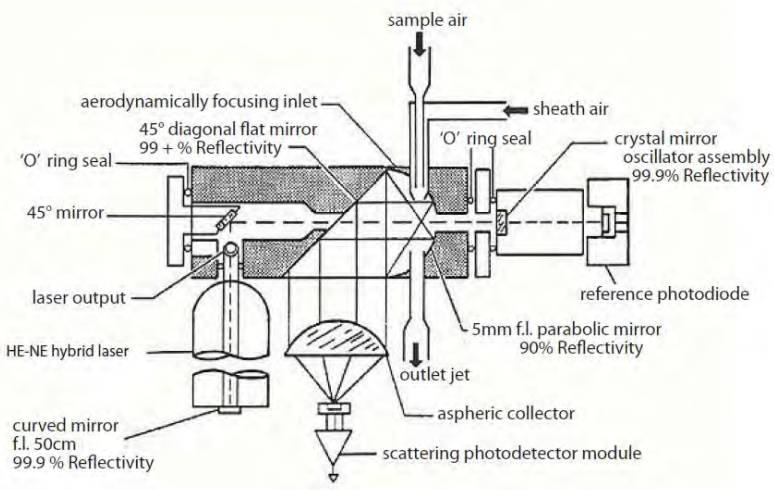

Figure 3.4: Schematics of the PCASP-100X optical system (Droplet Measurement Technologies, 2009).

Fig. 3.4 shows a schematic of the PCASP. The particle input is realized through an aerodynamically focused jet, which concentrates particle flow to a 150 μm diameter stream surrounded by a filtered sheath flow. The sample stream is positioned at the focus of a 5 mm focal length parabolic mirror. Furthermore, the laser source is a Gaussian

mode, He-Ne gas laser operating at a wavelength of 632.8 nm and the collected light is collimated by a parabolic mirror, reflected of a 45° flat mirror and then refocused by an aspheric lens onto the photodetectors (Droplet Measurement Technologies, 2009). According to Mie theory, the intensity of the scattered light depends on particle size and the refractive index (see Chapter 2.3.1 for Mie theory discussion). As Mie theory limits itself to spherical particles, a possible, non-spherical shape of particles is not taken into account by this method, but it can sometimes be an important contribution to scattering intensity distributions. I will not discuss this topic here and refer to Mishchenko et al. (2000) and references therein.
Thus particle size is derived from the measured intensity of scattered light using both, application of Mie theory and calibration with standard reference particles. This calibration is done by measuring reference particles, normally polystyrene latex beads (PSL), that come with single sizes with a very small dispersion, normally less than 2 %. The scattering cross section (see Equation 2.32) for a specific size is calculated from Mie theory for the laser wavelength, collection angle, particle diameter and refractive index (Pinnick and Auvermann, 1979; Liu and Daum, 2000). Referring to the measurement technique as such, the intensity of the scattered light measured by photodetectors depends on the laser wavelength and the detection angle. As these two instrument parameters are well known, the uncertainty of the complex refractive index and to a lower extent the particle shape determine the uncertainty of this measurement technique (Hamburger, 2010). Unfortunately a general problem occurs: scattering cross sections C_{sca} are inconclusive. On the one hand a given C_{sca} can be attributed to different diameters for different refractive indices. On the other hand Mie scattering itself leads to ambiguousness due to the so called *Mie oscillations*. An example of both effects is plotted in Fig. 3.5.

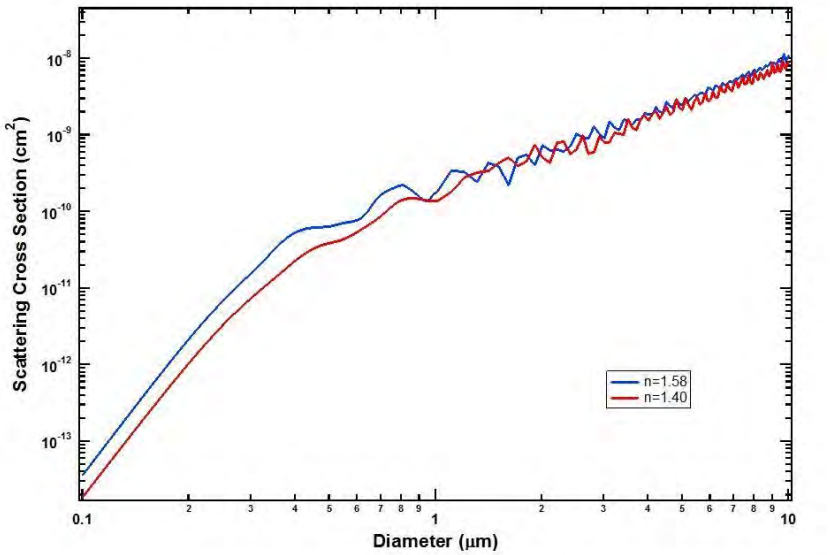

Figure 3.5: The curves show the relationship between scattering cross section and diameter for two refractive indices (according to the collection angles of the PCASP).

It has to be mentioned that the PCASP categorizes the measured intensity pulses into several count channels in order to measure the size distribution. Therefore the ambiguousness of scattering cross sections affords the necessity to group several channels

at the expense of accuracy. For the following analysis within the PSAP inversion (see Chapter 3.1.3), the PCASP channel borders were adapted to more than a hundred calculated refractive indices.

3.1.3 Absorption

In Chapter 2.3.3 we have already shown that the analysis of aerosol optical properties requires knowledge of the scattering coefficient σ_{sp} and the absorption coefficient σ_{ap}. According to Equation 2.44 the scattering coefficient σ_{sp} can be retrieved from the PCASP size distribution which has been discussed above. In contrast, the absorption coefficient has to be measured by an additional instrument. Besides in-situ photoacoustic techniques, filter-based techniques are a common mean to measure σ_{ap}. A widely used instrument is the **P**article **S**oot **A**bsorption **P**hotometer (PSAP) (Bond et al., 1999). The PSAP measurement technique rests upon the change in light transmission through a filter due to increasing aerosol deposition. Originally the PSAP was designed, modified and calibrated for the calculation of σ_{ap} for one single wavelength (Bond et al., 1999), but further development by Virkula (Virkkula et al., 2005) enables a spectral resolved measurement of σ_{ap}. In our study we used a 3-λ-PSAP measuring light attenuation at 467 nm, 530 nm and 660 nm. In general only sequences of constant altitude flight levels are suitable, because pressure changes during ascend and descend lead to measuring artefacts due to pressure changes (Petzold et al., 2009). Data analysis based on measurements with the 3-λ-PSAP form a large and important part of this thesis, therefore this measurement technique will be discussed more detailed in the following.

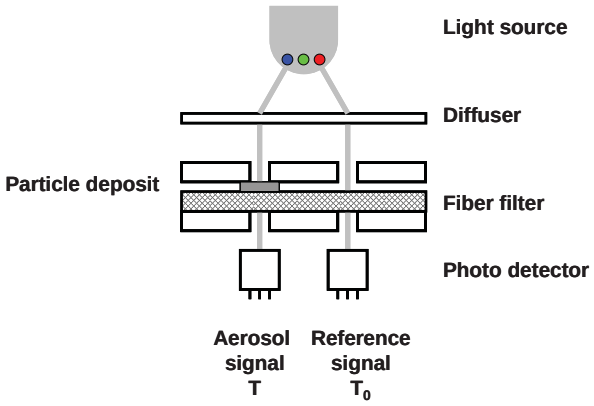

Figure 3.6: Schematic of the typical PSAP set-up, adapted from Bond et al. (1999).

Figure 3.6 shows a schematic of the used 3-λ-PSAP. Generally, the 3-λ-PSAP consists of a light source composed of three LEDs, a diffuser to create an absorption and a reference beam, the fiber filter and the photo-detector unit. Within the time interval Δt aerosol of a volume $V = Q \cdot \Delta t$ (where Q describes the flow rate) crosses the filter and approximately 100 % of the aerosol deposits on the filter fibre of area A. Simultaneously, one of the three LEDs is switched on for a short time alternately.

Therefore the absorption photodiode measures the transmitted intensity T of the light beam in intervals of Δt, so that the attenuation of light intensities (ATN) within one time interval Δt can be described as

$$\mathrm{ATN} = \ln\left(\frac{T_t}{T_{t+\delta t}}\right) \tag{3.1}$$

Thus, in principle the absorption coefficient can be derived from Lambert-Beer law using the measured attenuation ATN (Weingartner et al., 2003):

$$\sigma_0 = \frac{A}{V}\ln\left(\frac{T_t}{T_{t+\delta t}}\right) \tag{3.2}$$

The index $_0$ is chosen, because Equation 3.2 does not represent the real absorption coefficient σ_{ap}, but rather a raw form of an uncorrected direct output of the instrument as there are several error sources which are not considered in the simplified Equations 3.1 and 3.2.
First of all the transmission through the filter can be altered by purely scattering particles and therefore the measured absorption coefficient σ_0 has to be corrected by a factor $s \cdot \sigma_{sca}$, whereupon s is an empirical factor (Bond et al., 1999; Virkkula et al., 2005). Furthermore the PSAP signal has to be corrected due to the change of transmission as the filter gets darker with preceding measurement time. This approach is expressed by the empirical transmission correction function $f(Tr)$, with which the uncorrected response of the instrument σ_0 has to be multiplied. Therefore the real absorption coefficient σ_{ap} appears as follows:

$$\sigma_{ap} = f(Tr)\,\sigma_0 - s \cdot \sigma_{scat} \tag{3.3}$$

Based on Bond's investigation, the transmission correction function for a measured transmission Tr is given by:

$$f_{Bond}(Tr) = \frac{1}{0.71 + 1.0796 \cdot Tr} \tag{3.4}$$

Virkkula et al. (2005) extended the correction scheme regarding the influence of the single scattering albedo (for definition of ω_0 see Equation 2.49), because experimentally measured transmission functions $f(Tr)$ differ significantly for black and grey aerosol. During Virkkula's studies photoacoustic and nephelometer measurements served as references for the absorption and the scattering coefficients, respectively. Initially an improved transmission correction function solely for black aerosol is fitted:

$$f_1(Tr) = k_0 + k_1 \ln(Tr), \tag{3.5}$$

and thus a first attempt to calculate σ_{ap} is given by

$$\sigma_{ap_1} = (k_0 + k_1 \ln(Tr))\,\sigma_0 - s \cdot \sigma_{sp} \tag{3.6}$$

where k_0 and k_1 are wavelength-depended constants. For gray aerosol with a significantly higher ω_0 than for black aerosol two important observations can be found: the factor k_o remains nearly constant, whereas k_1 decreases with increasing ω_0 and the relationship between k_1 and ω_0 is linear (Virkkula et al., 2005). Therefore, the constant factor k_1 has to be multiplied by a correction function $h(\omega_0)$ which is defined as

$$h(\omega_0) = h_0 + h_1\omega_0 \tag{3.7}$$

Thus the final form of the absorption coefficient σ_{ap} is

$$\sigma_{ap} = (k_0 + k_1 h(\omega_0) \ln(Tr))\,\sigma_0 - s \cdot \sigma_{sp} \tag{3.8}$$

Because of inclusion of ω_0 in Equation 3.8, the absorption coefficient can not be calculated directly from the PCASP data output of σ_0 and Tr. Thus a simple iteration algorithm is necessary. This simple procedure is executed as follows:

1. Calculate an idealized absorption coefficient for soot using Equation 3.6.
2. Calculate an estimate of ω_0 using 3.7 and the result from step 1.
3. Calculate σ_{ap} using Equation 3.8.
4. Repeat the calculations of step 2 and 3 using the latest results from step 3 until σ_{ap} does not change significantly any more.

It can be shown that this algorithm scheme shows convergence after very few iterations. Iterative changes in σ_{ap} usually fall far below 1 % after the third iteration. All constants used for Equation 3.8 are provided in Tabel 3.2:

Table 3.2: Constants for calculation of σ_{ap} from PSAP raw signal (see Equation 3.8), errors are given as 95 % confidence limits. Addapted from Virkkula (2010).

Parameter	467 nm	530nm	660nm
k_0	0.377 ± 0.013	0.358 ± 0.011	0.352 ± 0.013
k_1	-0.640 ± 0.007	-0.640 ± 0.007	-0.674 ± 0.007
h_0	1.16 ± 0.05	1.17 ± 0.03	1.14 ± 0.11
h_1	-0.63 ± 0.09	-0.71 ± 0.05	-0.72 ± 0.16
s	0.015	0.017	0.022

Furthermore according to Bond et al. (1999) a flow as well as a spot correction is required, because the sample flow Q measured by the PSAP and also the spot diameter d of the filter can differ from the information given by the manufacturer. The simple correction equation for both terms is given by Equation 3.9

$$\sigma_0 = F_{flow} \cdot F_{spot} \cdot \sigma_{measured} \tag{3.9}$$

whereupon F_{flow} and F_{spot} are defined as follows:

$$F_{flow} = \frac{Q_{manufacturer}}{Q_{measured}} \quad \text{and} \tag{3.10}$$

$$F_{spot} = \frac{d^2_{manufacturer}}{d^2_{measured}} = \frac{A_{manufacturer}}{A_{measured}} \tag{3.11}$$

For the spot size correction, the filter area $A_{measured}$ was compared to the manual data and the correction factor turned out to be $F_{spot} = 0.9332$. Unfortunately no measurements of $Q_{measured}$ were available for the SAMUM-II flights discussed in this thesis. In terms of uncertainty considerations, a detection limit of $0.1 \times 10^{-6} m^{-1}$ can be considered for the absorption coefficient σ_{ap} referring to Petzold et al. (2002).

3.1.4 Volatility

The **t**hermo**d**enuder (TD) is an instrument that consists of an inert stainless steel tube where crossing aerosol is heated up to 250°C, which is sometimes followed by a denuder section of activated charcoal to remove the vapors. The overall idea of a thermo-optic technique for in situ analysis of aerosols goes back to Clarke (1991). Within the first section of a thermodenuder heating of the probed aerosol leads to evaporation of the volatile and semi-volatile compounds. To avoid recondensation during the following cooling process, activated charcoal can serve as a diffusion denuder that fixes all grown vapors, but it is only necessary for very high aerosol number concentrations of volatile particles. A schematic of a typical TD is shown in Fig. 3.7. For this case study we abandoned a charcoal denuder because of the experience from SAMUM-I.
All particles which evaporate or degenerate at 250°C are declared *volatile* particles, whereas those particles, which don't show any response to heating, are defined as *non-volatile* particles. The three most important volatile, respectively semi-volatile particle fractions are ammonium nitrate, ammonium sulphate and secondary organic particles. In contrast to the well-understood behavior of the first two fractions (Seinfeld and Pandis, 1996; An et al., 2007), the volatility of atmospheric organic aerosol is much less understood and therefore a subject of considerable attention recently (Faulhaber et al., 2009; Huffman et al., 2009).

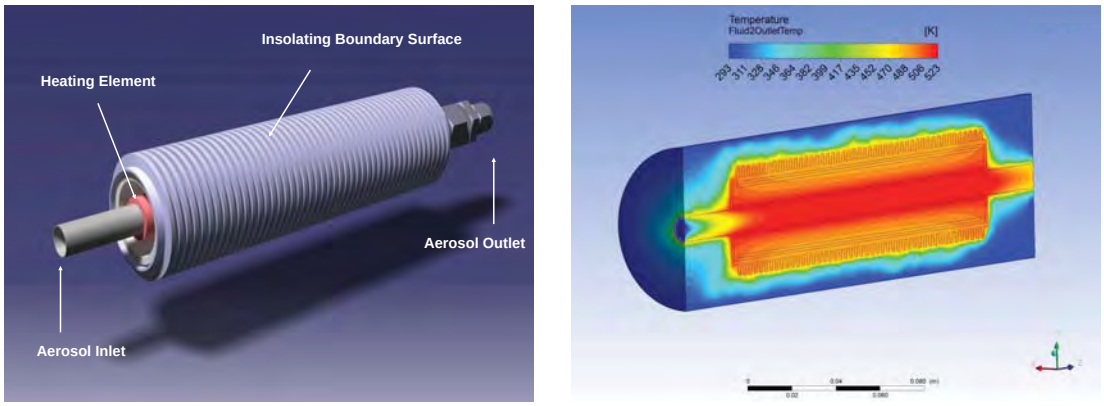

Figure 3.7: Body (left) and temperature distribution (right) of a thermodenuder used for aircraft measurements developed at DLR. Plots kindly provided by Amir Ibrahim, DLR.

As already mentioned in Chapter 3.1.1, during SAMUM-II the TD was used in combination with CPCs / CPSAs (and additionally with an OPC, but that analysis is not part of my diploma thesis). Adaptations of CPCs combined with TDs in front of the CPC are further explained by Curtius et al. (2005).

3.1.5 Aerosol optical depth and extinction coefficient

Apart from the in-situ measurements mentioned above, a **H**igh **S**pectral **R**esolution **L**idar (HSRL) was part of the Falcon instrumentation. Lidar (**Li**ght **d**etection **a**nd **r**anging) describes an active remote sensing technique, at which short laser pulses are emitted into the atmosphere where scattering by air molecules, aerosol particles and hydrometeors occurs. Detecting the atmospheric backscattering time-resolved, the location of the scattering event can be calculated by measuring the time interval each photon needs to run from the emitter to the location of scattering and back to the detector (respectively the telescope) which is located directly beside the laser source (see Fig. 3.8). Thus, a lidar is able to provide vertical profiles of different parameters.

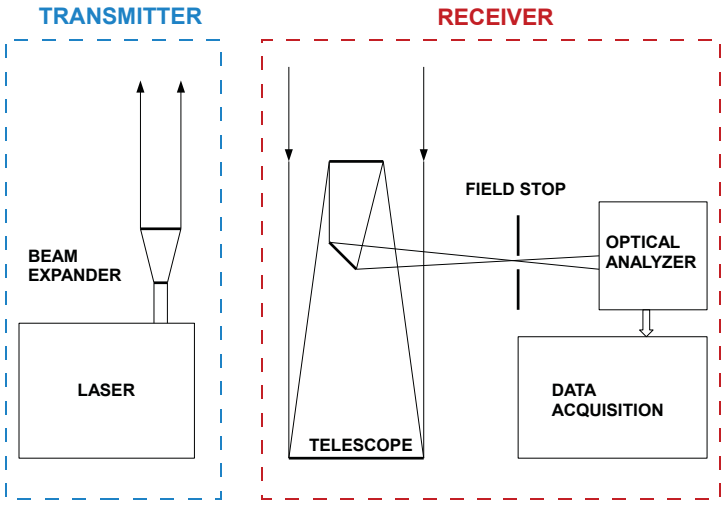

Figure 3.8: Principle set-up of a lidar system after Weitkamp (2005).

Lidar in general has been used to investigate several atmospheric phenomena like turbulence processes, water-vapor and ozone fluxes and optical aerosol parameters for many years (Weitkamp, 2005), but only two HSLR instruments have been developed to date for airborne applications. One at DLR, Germany, based on an iodine vapor absorption filter and a high power, frequency doubled Nd:YAG laser (Esselborn, 2008) and a similar one at NASA (Hair et al., 2008). Conventional backscatter lidars can only measure backscatter and need an assumption of the so called *lidar radio* S_a, which describes the aerosol extinction-to-backscatter ratio (see Equation 3.12):

$$S_a(r) = \frac{\sigma_{sp\_b}(r)}{\sigma_{ext}^T(r)}, \tag{3.12}$$

where σ_{sp_b} is the total aerosol backscatter coefficient and σ_{ext}^T is defined as the total aerosol extinction coefficient. For this study, we will concentrate on the aerosol optical depth AOD, which can easily be calculated, if the height dependent aerosol contribution τ_a is known.

$$AOD(r) = -\frac{1}{2}\ln\left[\tau_a^2(r)\right] \tag{3.13}$$

The calculation of $\tau_a(r)$ is the result of a complex retrieval combining the measured powers in the parallel-polarized and the cross-polarized channel of the detector (Esselborn et al., 2008). As the lidar ratio of tropospheric aerosol can vary over a wide range (from 20 to 100 sr), conventional backscatter lidar measurements possess a large uncertainty in the retrieved aerosol extinction (Esselborn, 2008; Hair et al., 2008; Su et al., 2008). For that reason, the main advantage of a HSRL is the fact that both, aerosol backscatter and extinction coefficients can be measured directly which leads to a significant decrease of systematic errors. Thereby the HSRL technique utilizes the spectral distribution of the lidar return signal to discriminate aerosol returns from molecular returns and calculates backscatter coefficients and aerosol extinction independently. The HSRL technique relies on the difference in spectral distribution of backscatter signal from molecules and particles, see Fig. 3.9. Furthermore the discrimination between aerosol and molecular returns in the airborne HSRL receiver is realized by splitting the returned signal into two optical channels: the molecular and the backscatter channel. An extremely narrowband iodine vapor (I_2) absorption filter serves as a key element to eliminate the aerosol returns. Therefore only the wings of the molecular spectrum can pass the molecular channel, whereas the total backscatter channel can be passed by all frequencies of the returned signal.

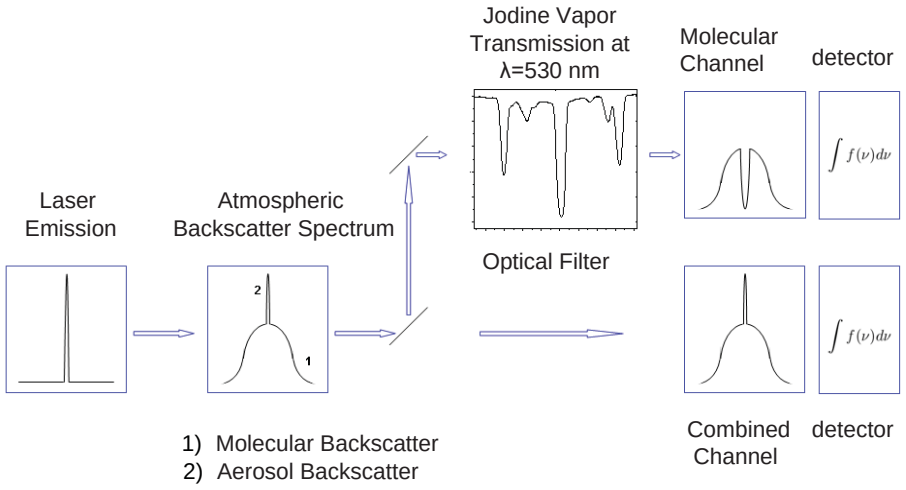

Figure 3.9: Principle set up of the HSRL, according to Esselborn (2008).

The general theoretical treatment to calculate optical depths by lidar measurements is to invert the "lidar equation". For a detailed discussion of the lidar equation for conventional backscatter lidars and the HSRL, refer to Klett (1981), Wandinger et al. (2002), Esselborn et al. (2008), Hair et al. (2008) and Rogers et al. (2009). All mentioned authors show detailed descriptions of their inversion algorithms and the corresponding uncertainties.
The key parameters of the HSRL used for the SAMUM-II measurements are as follows:

- The airborne HSRL is a 532-nm-HSRL with polarization-sensitive detection at 532 nm and 1064 nm realized by photodiodes.
- The returned signal is collected by a 350 mm Cassagrain telescope with an acceptance angle limitation of 1 mrad.
- The laser used in our HSRL is a high-power, Q-switched Nd:YAG s laser with a pulse energy of 200 mJ at 1064 nm and a repetition rate of 100 Hz.
- Iodine vapor filters serve as splitters for the returned signal (molecular spectrum/ aerosol + molecular spectrum).

3.1.6 Single particle chemical analysis

The complete analysis of all impactor samples of this study was conducted by the Institut für Angewandte Geowissenschaften, Technische Universität Darmstadt. Kirsten Lieke and Konrad Kandler kindly provided the results of their analysis for use within my diploma thesis as a good amendment to my results from the PSAP Inversion (see Subsection 3.2.2). Since I was neither involved in the measurement nor the analysis, I will only tender a short abstract about this measurement technique and refer to literature for further information.
All samples discussed in this thesis were collected with a set of six two-stage (0.1–1 and 1–3 μm aerodynamic diameter) miniature impactors (Kandler et al., 2007) and a body impactor mounted in a wing station of the aircraft (**G**iant **Pa**rticle **C**ollector, GPaC). The assembly and sampling conditions for the small particles (up to $d_p \approx 3\,\mu$m) were the same as during the SAMUM-I campaign (Kandler et al., 2009). Particles were collected on nickel grids for **T**ransmission **E**lectron **M**icroscopy (TEM), coated with formvar-carbon-foil, and on adhesive carbon substrate mounted on nickel disks. The aerosol inlet of the DLR Falcon research aircraft reduces the maximum particle size of collected particles to a diameter of 3 μm (Petzold et al., 2009). But in airborne desert dust, much larger particles with diameters up to tens of microns can be expected. As no sampling equipment for these large particles is commercially available, it was necessary to develop a new particle sampler to collect large airborne particles. The GPaC has a substrate diameter of approximately 9 mm. Through the interaction of the air flow velocity at the airplane (200 ms^{-1}) and the mass inertia of the airborne particles, particles collide with (or impact on) the substrate.

In the present study, an environmental scanning electron microscope "ESEM Quanta 200 FEG" equipped with a field emission gun and an EDAX energy-dispersive X-ray detector was used. Based on the X-ray count rates, particles were classified into different groups. In order to recognize soot particles on a carbon coated substrate, all small stage samples had to be investigated manually. Soot and other small particles ($30\,\mathrm{nm} \leq d_p \leq 500\,\mathrm{nm}$) were characterized based on their characteristic morphology. An example of TEM images is presented in Fig. 3.10, where external and internal mixtures of soot are shown. In general the chemical composition of the particles is expressed as element index. This index is defined as the atomic ratio of the concentration of the element considered and the sum of the concentrations of the elements Na, Mg, Al, Si, P, S, Cl, K, Ca, Ti, Cr, Mn, and Fe. Element indices and ratios between different element indices are used to describe the complex composition of the particles. More detailed

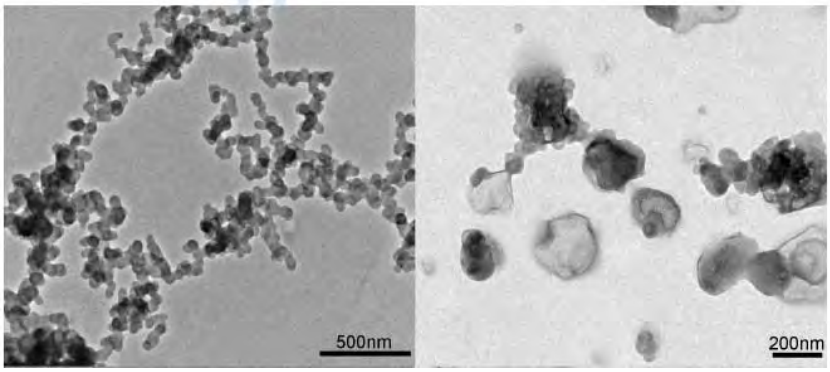

Figure 3.10: TEM bright field images of pure and externally mixed soot agglomerates (left) and internal mixtures of soot and sulphates (right); images provided by Kirsten Lieke.

information on this measurement technique will be available in Kandler's distribution to the Tellus B - special issue for the results of SAMUM-II, which will be published in Vol. 63, 2011. In summary, the combination of a two-stage impactor and a giant particle collector allows sampling of particles over a wide size range from below hundred nanometers to some tens of microns.

3.1.7 Meteorological data

According to meteorological parameters particularly relative humidity, temperature and especially wind speed and direction are the key objects of investigation. The meteorological data is based on three sources:

- ***Synoptic data from Dakar Yoff airport(WMO 61641)***
  Unfortunately only this one synoptic station is available for the region of interest.
- ***In-situ data from the Falcon***
  The falcon in-situ data includes recent temperature, wind speed and wind direction. Additionally the relative humidity is measured by a humicap sensor.
- ***Analysis data from the ECMWF***
  The ECMWF data has a horizontal resolution of $0.225° \times 0.225°$ and is provided for intervals of three hours.

In addition to that, the MM5 mesoscale meteorology model will be part of the meteorological analysis (see Chapter 3.2.3).

3.2 Data Analysis Methods

In this section a short abstract about the general data analysis scheme is given, because the master plan of different data anaylses serves as a body for this thesis. In addition to the more technical descriptions in Section 3.1, a detailed description of the PSAP-Inversion scheme and the meteorological models used for the analysis is provided.

3.2.1 Overall analysis scheme

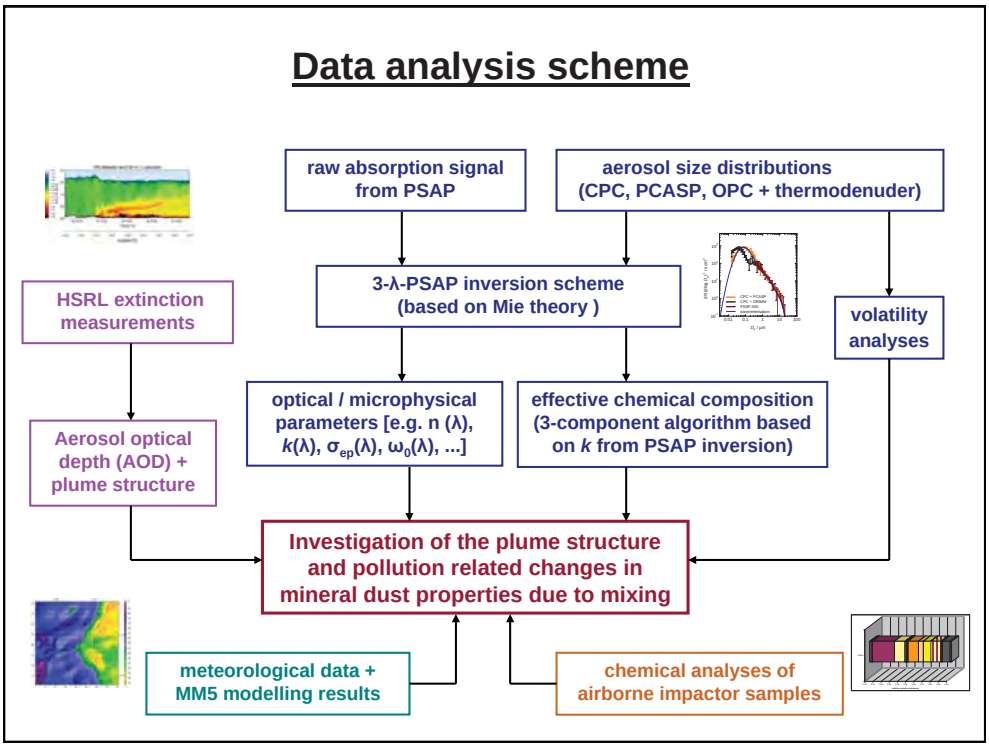

Figure 3.11: Principle data analysis scheme of this case study

The basic questions as well as the key parameters of this study have been presented in Section 1.2. Now, as a detailed description of the measurement techniques has been provided, a framework of the analysis scheme shall be given. Figure 3.11 shows an overview of the principle data analysis scheme of this case study using data from the instruments described in Section 3.1. The overall goal of the different analysis methods is the investigation of the changes in microphysical and optical dust properties due to mixing with Dakar's urban pollution plume. Thus, various fields of investigation are necessary to approach a detailed picture of the plume and its characteristics. First of all, appearance and extension of the plume crucially depend on the meteorology. Therefore in-situ data as well as the MM5 mesoscale model are used to get a rough picture of the plume dynamics. In addition to the meteorological data, also remote sensing data of the HSRL provides information about the plume structure and beyond that the optical depth can be calculated for the plume as such and the surrounding. The aerosol in-situ part of the analysis is particularly based on the PSAP, PCASP and

CPC data, whereupon the PSAP data analysis scheme affords the lion's share of the optical and microphysical parameters including absorption and scattering coefficients, refractive indices and single scattering albedo. Moreover, a volatility analysis which rests on the size distribution data permits conclusions about the mixing state of the aerosol. The last part of the overall analysis scheme takes into account the single particle chemical analysis from the Technische Universität Darmstadt, which amends the results from the other analysis methods.

3.2.2 PSAP data analysis scheme

The PSAP data analysis was the most time-consuming part of my work and thus it requires special discussion. Apart from the HSRL data and the size distributions, all results referring to microphysical and optical parameters were calculated with this analysis method. The basic design of the analysis scheme was adapted from the PSAP data analysis scheme shown in Petzold et al. (2009). The code as such was written by myself (programmed in Python) and, compared to Petzold et al. (2009), there are several significant simplifications and changes, which I developed and implemented within this diploma thesis.

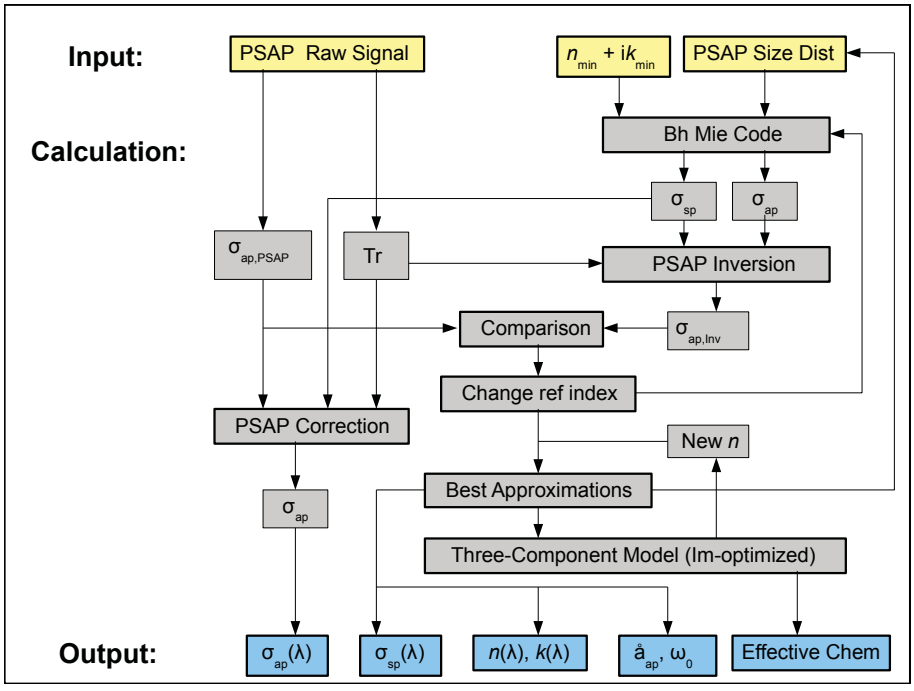

Figure 3.12: Iterative data analysis algorithm for PSAP and PCASP data

Fig. 3.12 shows a schematic of the data analysis algorithm which I will discuss in the following.

The input

The PCASP size distribution data and PSAP raw data serve as main input for the algorithm. Additionally a first guess of the complex refractive index is needed. According

to Petzold et al. (2009) and these refractive indices measured during SAMUM-I, a minimum real part of $n_{min} = 1.540$ and a maximum real part of $n_{max} = 1.570$ appears to be appropriate to choose, because all source regions of Saharan dust measured during SAMUM-I (which are not far away from those of SAMUM-II) provide real parts in this range. The minimum imaginary part is always chosen $k = 0$ for the first iteration and increased thereafter. However, a good choice of the first refractive index does not influence the results in any way, but it can diminish the calculation time significantly. In contrast to Petzold et al. (2009) the size distribution data is limited to the PCASP size range of 0.15–2.5 μm using a 10-s moving average and does not include CPC measurements because of the size distribution maximum of dust aerosols which lies at diameters $>>$ 0.1 μm and the less relevant importance of sub-100 nm particles to Mie scattering of visible light. Therefore we passed on the CPC data, which would have added up large additional work expenses.

The calculation steps

The PSAP data analysis scheme consists of a sequence of several programs which will be discussed briefly in the following. Until iteration step 5 the procedure is done analogous for all three PSAP wavelengths (467 nm, 530 nm, 660 nm).

1. ***BHMIE Code***
   Since no direct measurement of σ_{sca} was available, the scattering coefficient was calculated by Mie theory using the BHMIE code of Bohren and Huffman (1983) with PCASP size distribution data as input. The calculated scattering and extinction cross sections are directly converted to scattering and absorption coefficients which serve as input for the PSAP Inversion and the PSAP Correction program.

2. ***PSAP Inversion***
   The PSAP Inversion program uses the directly measured transmission Tr as well as the BHMIE output of absorption and the scattering coefficients (σ_{ap} and σ_{sp}) to recalculate the uncorrected absorption coefficient of the PSAP, $\sigma_{ap,Inv}$.

3. ***Change Ref Index***
   Then the directly measured absorption coefficient $\sigma_{ap,PSAP}$ is compared to the inverted absorption coefficient $\sigma_{ap,Inv}$ and the deviation is saved. After that the refractive index n_{min} is increased by Δn and the iteration steps 1 to 3 are repeated several times until $n = n_{max}$ and the same process is realized for the imaginary part k. Thus up to several thousand combinations of n and k and the corresponding inverted absorption coefficients are available.

4. ***Best Approximations***
   After one run through all predetermined refractive indices several combinations of n and k are chosen, for which the sum of the squared deviation of the (measured and inverted) PSAP absorption coefficients for all three wavelengths is a minimum. Typically the result of this search is ambiguous, but as the imaginary part is the far more sensitive parameter and does not differ too much within the real parts of Saharan dust, one can define a λ-dependent choice of real parts taken from SAMUM-I due to source regions. The next iteration step uses the chosen n and k for a new calculation of the size distribution, because the response of the PCASP depends on the refractive index as well (see Subsection 3.1.2). Then the

iteration steps 1–4 are repeated until the refractive indices respectively the size distribution do not change any more. Usually convergence can be observed after 2–5 iterations.

5. ***Three-Component Model***
   The three-component model is not part of the main algorithm consisting of steps 1–4. It is based on the assumption that the probed dust aerosol forms an external mixture which can only be proofed by chemical analysis. For external mixtures Ackerman and Toon (1981) and Quimette and Flagan (1982) showed that the optical properties of a mixture of aerosol particles can be described as the sums of the optical properties of the individual distributions. Therefore I designed a simple python program that reconstructs the imaginary part of the refractive index for all three wavelengths by a certain (volume) composition of three components: quartz, soot and iron oxide (a detailed description is given in the subsection "discussion". The k-optimized algorithm runs 1000 iterations and outputs volume fractions of the three components as well as the performance of the k-reconstruction. Usually k differs less than 5% for every of the three wavelengths. As the real part n of the refractive index is not indepent from k due to the special effective chemical composition within the model, the output of this additional algorithm provides real parts n for all three wavelengths. Thus the ambiguousness of the PSAP Inversion can be solved by using these real parts. Therefore the algorithm steps 4 and 5 have to be repeated. Usually a maximum of two iterations is necessary for convergence of this scheme.

6. ***PSAP Correction***
   After convergence of the algorithm step 4 and 5, the last step is to calculate the real absorption coefficient using the optimized scattering coefficient of the last iteration. Coming from the PSAP raw data input, the absorption and scattering coefficients σ_{ap} and σ_{sca} are calculated following Bond et al. (1999) and Virkkula et al. (2005), respectively Virkkula (2010) as described in Subsection 3.1.3.

The output

The output of the PSAP analysis scheme consists of many parameters. Besides meteorological and technical data like altitude and gps coordinates, the optical parameters σ_{ap}, σ_{sp}, $\mathring{a}_{ap}$, ω_0, the refractive indices n and k and the simulated effective chemical composition (volume fractions of quartz, soot and iron oxide) are provided.

Discussion

The main difference to the PSAP data analysis scheme given by Petzold et al. (2009) is the simplified chemical analysis scheme. At first glance the assumption to use a non-size-resolved effective chemical component model could be interpreted as a regression. Particularly the inclusion of quartz instead of the kaolinite and the negligence of ammonium-sulphate are points of critique. But there are several arguments for the use of our PSAP data analysis scheme. At first, the main advantage is the indepedence from any priori assumption of n for all three wavelength. The idea is to model the refractive index with three idealized components: a nearly exclusively light scattering component (quartz), one light absorbing component with weak spectral dependence (soot) and one light absorbing component with strong spectral dependence (iron oxide). This is

a completely new approach of a PSAP data analysis and it forms a major part of my thesis. The reason for a limitation to three components is forced by the maximum of three degrees of freedom given by the input parameters which are available for three wavelengths. Otherwise the independence on further assumptions or a known chemical composition would not be given anymore. The idealized model components quartz, soot and iron oxide were chosen because of several reasons. Si is the dominant component of Saharan dust and it is incorporated in many minerals, namely in ilite, albite, kaolinite, quartz and many others (Formenti et al., 2003; Krueger et al., 2005; Kandler et al., 2007). Due to the exact atomic structure and composition these minerals show large variations due to the refractive index. According to Sokolik and Toon (1999) and Kandler et al. (2007) the real part n of the Si-containing species mentioned above varies far more than the range of $1.545 < n < 1.565$ measured during the whole SAMUM-I campaign not to mention the much larger variations in k. Therefore the simplification to only one (mainly) scattering component quartz with $1.541 < n < 1.545$ (for the PSAP wavelengths) seems to be reasonable, even if the real quartz fraction usually does not exceed a maximum of 20 % vol. Iron oxide (Fe_2O_3) was chosen, because hematite fractions are the main absorbing mineral dust component. Moreover soot represents the anthropogenic component of this case study and even if there are plenty of organic carbon species, soot dominates the radiative forcing due to its highly absorbing features. Table 3.3 provides an overview of the spectral resolved refractive indices which solve as input for the three-component model within the PSAP data analysis scheme. See also Fig. 2.5, where the refractive index for the three components is described for the whole visible spectrum.

Table 3.3: Spectral dependence of the refractive indices used in the three-component model in the PSAP data analysis scheme, data is adapted from Sokolik and Toon (1999) for quartz and iron oxide and Shettle and Fenn (1979) for soot.

material	Re(467 nm)	Im(467 nm)	Re(530 nm)	Im(530 nm)	Re(660 nm)	Im(660 nm)
quartz	1.545	1e-6	1.543	1e-6	1.541	1e-6
soot	1.7456	0.4412	1.7456	0.4392	1.7456	0.4216
iron oxide	3.0872	1.0165	3.173	5.77e-1	3.095	2.29e-2

This analysis scheme is adapted to the mixture of mineral dust with anthropogenic soot emissions and will fail for any other approach. Nevertheless, for other types of aerosols three different components can be chosen and therefore the analysis scheme as such can also serve as a more general method to investigate the parameters mentioned above.

Error Sources

There are several error sources which appear due to measurement uncertainty and methodical errors. In the following I will provide a list of all known error sources and discuss the most important ones in detail afterwards.

Measurement Uncertainties:

- *Size distribution uncertainties measured by PCASP*

- *PSAP transmission Tr and raw absorption coefficient* $\sigma_{ap\_PSAP\_meas}$
- *Lack of flow measurements / flow correction of the PSAP data*

The uncertainty of the size distribution can be estimated by the standard deviation of the mean count numbers during a flight sequence of some minutes, if the aerosol layers do not change significantly. For the PSAP data the process works simultaneously, but additionally the lack of implementation of the flow measurements contributes to the measurement uncertainties.

Systematical Uncertainties:

- *Lack of sub-100 nm particle data*
  As mentioned above, the maximum of the size distribution for mineral dust is situated at particle diameters $d_p >> 0.1\,\mu$m and an artificial addition of a typical mineral dust fine mode to the PSAP analysis scheme showed only very small influence on all output parameters. Therefore one can neglect this effect for the dust dominated measurement sequences.

- *Deviation of inverted and measured* $\sigma_{ap,PSAP}$
  The PSAP data analysis scheme contains the comparison of the inverted and the measured $\sigma_{ap,PSAP}$. This parameter basically depends on the calculation intervals for the refractive index and the deviation of both $\sigma_{ap,PSAP}$ yields less than 1 %, if the calculation intervals are chosen small enough.

- *Mie theory (mainly the effect of non-spherical particles)*
  Uncertainties caused by the use of Mie theory can be assumed to be small, for more information see Petzold et al. (2009). A detailed error analysis of the Mie calculation would go far beyond the scope of this diploma thesis.

- *Refractive index / three-component model calculation errors*
  The complex refractive index modeled by the three components usually fits in the given refractive index from the PSAP data analysis within 5 % for every single wavelength and less for the average of all three.

- *Refractive index / three-component model systematic errors*
  Referring to the simplicity of the three component model it has to be mentioned explicitly that our results for volume fraction of soot, quartz and iron oxide are no chemical analysis in the classical meaning. The model output for the effective chemical composition can only serve as a rough estimate, but it will turn out to be very useful for this case study, because the relative changes of the effective chemical composition allow important conclusions. Nevertheless, although the effective chemical composition has a high uncertainty, the output of the real part of the refractive index used for calculation of all other parameters has only a small dependence on the effective chemistry. More about the sensitivity due to the optical parameters will be discussed within the results of this study.

Taking into account the error sources mentioned above, the most important quantifiable uncertainties arise from the errors in measurement. The detection limit of this method in terms of an absorption coefficient can be estimated as $0.1 \times 10^{-6}\,\mathrm{m}^{-1}$ at standard conditions referring to Petzold et al. (2009) as the detection limit is rarely influenced by the PSAP Inversion Scheme.

3.2.3 Set-up of the MM5 model

The theoretical background of the non-hydrostatic PSU-NCAR MM5 has already been described in Section 2.5. In this chapter an overview of the chosen basic model parameters including grid positions, grid sizes and boundary layer parameterization will be provided. All in all the description is limited to the most important parameters, because a detailed discussion of any single model parameter would go beyond the scope of this diploma thesis. Nevertheless, all necessary model adjustments to re-model the basic results of this case-study will be provided.

The aim of the MM5 model configuration is the alignment of model parameters to the special aims of our study. On the one hand an analysis of small scale aerosol plume structures and local sea breezes requires a high resolution horizontal grid that reaches the microscale, defined as the scale < 2 km (Orlanski, 1975; Markowski and Richardson, 2010). On the other hand the large distances of flight paths and backward trajectory calculation demand extended grids of the mesoscale up to some hundred kilometers. Against this background a set up of three model domains with horizontal grid distances between 1.0 and 9.0 km and horizontal extensions from 52 km up to 1080 km were chosen (see Fig. 3.13).

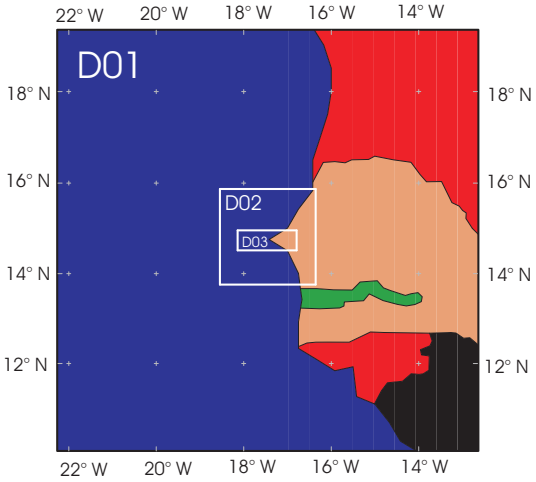

Figure 3.13: MM5 terrain model set up for the West African coast, the Dakar peninsula is centered in the middle of all three domains. For further description of domains D01–D03, see Table 3.4.

Because this case study focuses on the 29th of January 2008 only, the MM5 calculation were limited to the period from 00 UTC 28/01/08 to 00 UTC 30/01/08. For all three domains the coordinates 14.73° N and -17.45° W (located in the middle of the Dakar peninsula) form the central grid latitude and longitude, respectively. The choice of the Mercator map projection reflects the proximity to the equator. As the mesoscale flow is directed westward, domain D03, which serves as the key domain for sea breeze characteristics in the urban area of Dakar, is oblong and not quadratic. Figure 3.14 shows that the relief of west Senegal is affected by shallow hills and spacious plains.
The vertical grid contains a total of 23 layers and 5 layers within the first 1 km above the surface, a detailed list of the used σ-levels is given in the appendix, see Section A.

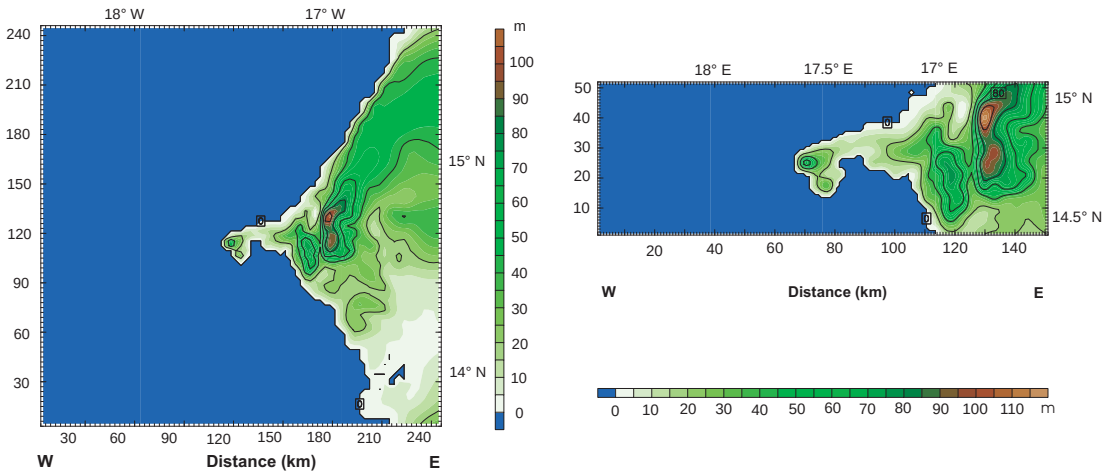

Figure 3.14: Terrain heights of MM5 model domains D02 (left plot) and D03 (right plot). Units for x- and y-axes are given as grid point of the referring domain. For conversion into distances, see Table 3.4.

At this point it has to be mentioned that the attempt to run a 30-layer model with 10 layers between ground level and 1 km failed because of numerical problems. A general overview of the most important model parameters is given by Table 3.4:

Table 3.4: Set up of MM5 model domains

Parameter	Domain D01	Domain D02	Domain D03
Grid dimensions in y direction	120	82	52
Grid dimensions in x direction	120	82	151
Number of vertical layers	23	23	23
Horizontal grid distance	9.0 km	3.0 km	1.0 km
Terrain input data resoultion	2 min (4 km)	2 min (4 km)	2 min (4 km)
Type of nesting	One way	Two way	Two way

"Nesting" describes the transfer of parameters at the domain boundaries. In one-way nesting, the coarse-resolution domain simulation is run independently of the nest. Here D01 serves as the mother domain which is initializes with data input from ECMWF analysis data, but there is no feedback between the nest (D02 and D03) and the coarse domain D01. In contrast two-way nesting is interactive and allows feedback to occur between the coarse-resolution domain and the nest throughout the simulation. The two domains are run simultaneously to enable this feedback (Dudhia et al., 2005). Concerning the terrain and landuse for all three domains, the input data are taken from USGS data. They contain 15 landuse categories, 25 vegetation categories and 17 soil categories. For more information about these categories and all other parameters, see Grell et al. (1995).
I will not discuss the cumulus parameterization here, because it is only suitable for

grids $\geq$ 10 km what is far more than those grids used in this thesis. A last point relevant for my studies is the planetary boundary layer (PBL) parametrization scheme. An appropriate scheme for small scale see breezes is the Gayno-Seaman scheme (GS), which is based on the Mellor-Yamada turbulence closure scheme, a higher order complex turbulence scheme (Janjić, 1990). The GS is determined by the use of liquid-water potential temperature as a conserved variable (Shafran et al., 2000). According to the special case of sea breezes Srinivas et al. (2007) and Miao et al. (2009) present extensive comparisons of several PBL scheme performances for small scale MM5 grids.

3.2.4 Back trajectories

For the interpretation of aerosol in-situ measurements, air mass transport analyses by means of trajectory models supply important information about aerosol source regions and the meteorological conditions along the transport path way. Although precision and availability of the meteorological input data have increased during the last years, single trajectories have position errors in the range of 20 % of the transport distance (Stohl et al., 1998). Trajectory ensembles help to estimate the sensitivity of the calculated transport path ways, even if they do not improve the accuracy as such. In our case study we applied a flight-analysis tool Hamburger et al. (2010), which is based on the Lagrangian Analysis Tool LAGRANTO developed by Wernli and Davies (1997). A bunch of 100 trajectories is started from a predefined box, which is centred on the starting point. The box has a horizontal radius of 500 m and a vertical depth of 200 m. Meteorological data used for the trajectory calculation is retrieved from the ECMWF operational archive. The data have a horizontal resolution of $0.225° \times 0.225°$ and a vertical resolution of 91 levels. Prognostic data (+3h) complement the temporal resolution of the operational archive of six hours. Thus, a temporal resolution of three hours can be provided for the trajectory calculation.
In addition to the back trajectories based on the ECMWF analysis data, the results from the MM5 provide single back trajectories with a considerably higher resolution.

Chapter 4

Results

In the following the results of this case study will be presented. Preliminary a short section about the flight strategy is given to draw a rough picture of the overall attempts for the flights #290108a and #290108b. All in-situ and HSRL data are referred to these two flights which took place on 29 January 2008. In Section 4.2 results from the basic data analysis and observed indications for the detection of the Dakar plume will be presented. In order to develop an appropriate basis for the interpretation of the further, more detailed data analysis, the third section provides a large investigation about the plume structure and the local circulation pattern. Thereafter particle microphysical and optical properties are characterized in detail, followed by the results from chemical analysis and refractive indices. At this point it has to be mentioned that the HSRL results had been part of the basic data analysis of SAMUM-II and were kindly provided for this case study by Dr. Christoph Kiemle and Dr. Michael Esselborn (both DLR). Additionally to the basic HSRL data, additional plume specific figures were for the Dakar region were created. Apart from results of the in-situ basic data analysis and the single particle chemical analyses, which were accomplished by Dr. Konrad Kandler and Dr. Kirsten Lieke (both TU Darmstadt), all other results were calculated, analyzed and interpreted by myself.

4.1 Flight Strategy

This section about the flight strategy is placed in the results chapter, because the reasons for the choice of the flight pattern include important results referring to satellite pictures and trajectories. In general a flight strategy for airborne aerosol measurements depends on the meteorological situation and the aims of studies. The key objects of this study have already been discussed in Chapter 1.2. In the period from 28 to 30 January 2008 a strong Western Sahara dust outbreak extended from the Western African coast to the Cape Verde Islands. During this episode the airflow between the surface and ca. 1.5 km a.s.l. was characterized by a strong zonal flow from east to west. Satellite pictures from EUMETSAT and MODIS (`http://earthobservatory.nasa.gov/images/imagerecords/19000/19569/nafrica\_tmo\_2008029\_lrg.jpg`), here for 29 January 2008, illustrate this dust outbreak featuring a nearly cloudless region with significant dust layers between the West African coast and the Cape Verde Islands, see Fig. 4.1.

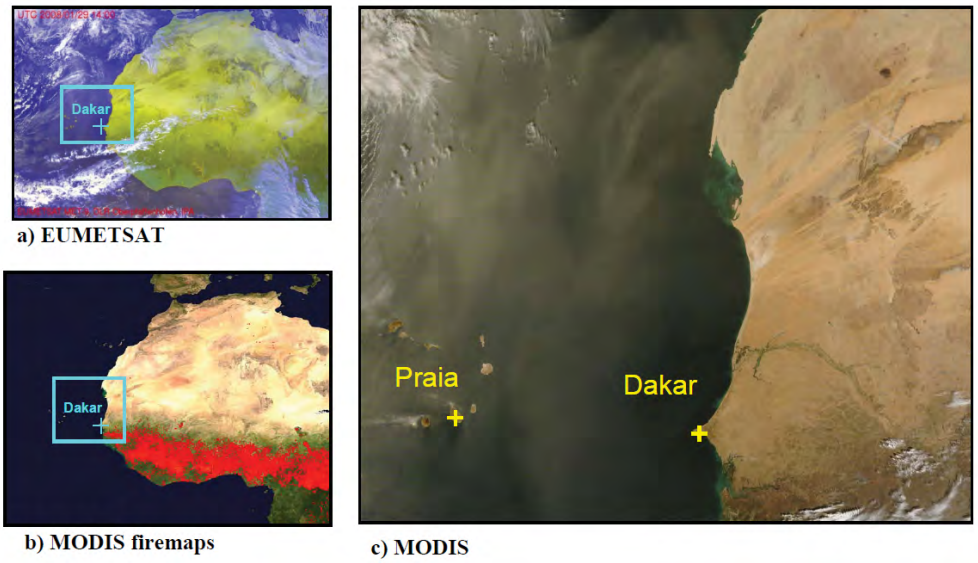

Figure 4.1: Satellite pictures of the Western Sahara dust storm episode 28 - 30 January 2008: (*a*) EUMETSAT for 29 January 2008, 14 UTC, (*b*) Modis Firemap 21 - 30 January 2008 , (*c*) MODIS for 29 January 2008, 1145 UTC ; See text for further description.

The MODIS Fire Map (`http://earthobservatory.nasa.gov/NaturalHazards/view.php?id=19569`) provides additional information about bush fires (marked in red) during the dust outbreak. Widespread biomass burning was observable in the wet-savanna south of the Sahel, but there were no significant bush fires within the dust outbreak region east or northeast of Dakar. This information is important with respect to the characterization of the measured aerosol within the Dakar plume. If there had been bush fires upstream the Dakar area, it would have been challenging to assign the contribution to different sources. For further information on the MODIS Rapid Response Algorithm, refer to Giglio et al. (2003) and Pinheiro et al. (2007).

Backward trajectories for 30 January 2008, 21 UTC, starting at Cape Verde Islands in 950 hPa and 775 hPa, respectively, show that the mesoscale flow during the dust storm episode (28 - 30 January 2008) varied significantly between the mentioned pressure levels, see Fig. 4.2 and 4.3. The low level Cape Verde air masses are determined by a strong westerly flow during the entire dust storm episode. Therefore these air masses are not influenced by biomass burning, whereas air masses of greater heights originate from the bush fire regions. That means that the zonal flow is limited to the lower boundary layer, but in this study all analyzed flight sequences are located within the first km above the surface. The specific meteorological situation consisting of a strong zonal flow within the boundary layer allowed a quasi-Lagrangian study of mineral dust transported from Western Africa across the coastline over Dakar (Dakar airport DKR: 14° 44' 23" N, 17° 29' 25" W; 26 m a.s.l.) to the Cape Verde islands (Praia airport RAI: 14° 55' 28" N, 23° 29' 37" W; 70 m a.s.l.).

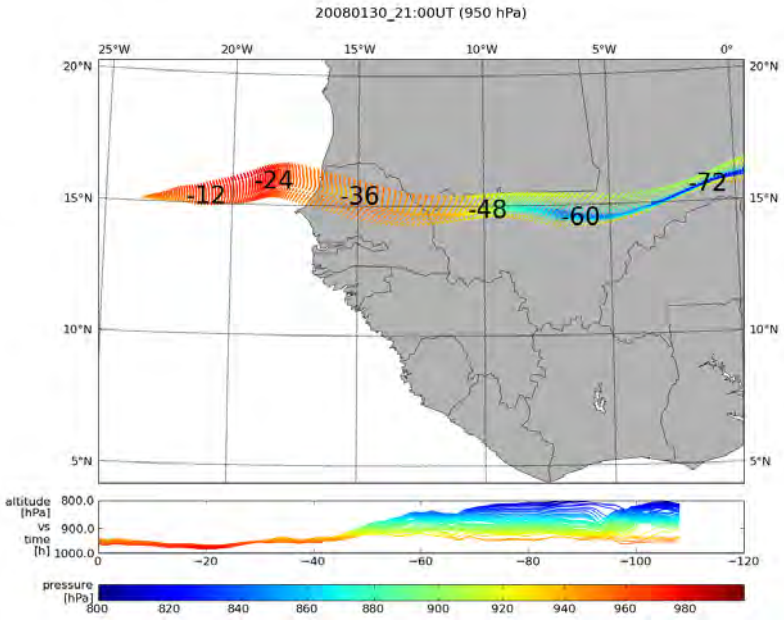

Figure 4.2: Back trajectories for 15.1° N, -23.5° W (near Praia) starting on 30 January 2008, 21 UTC, at a 950 hPa starting-level. Black labels along the trajectories show backward times in hours.

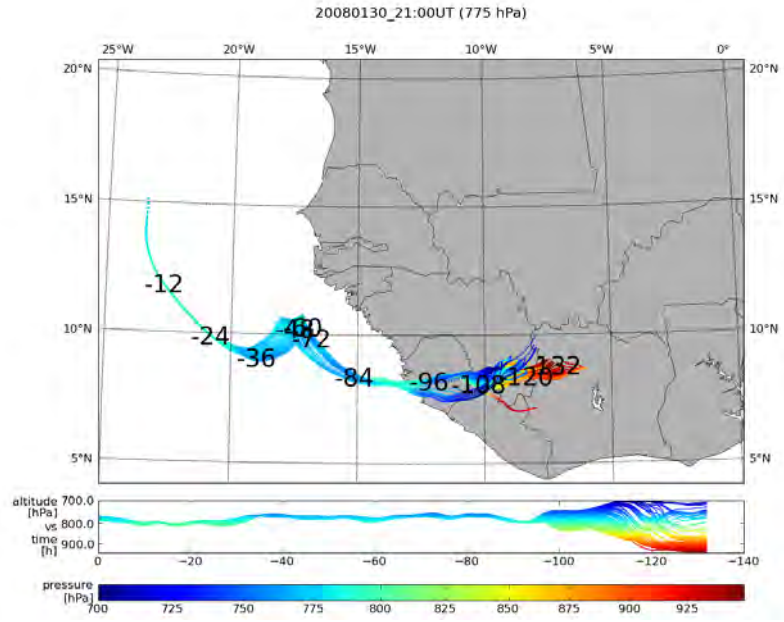

Figure 4.3: Back trajectories for 15.1° N, -23.5° W (near Praia) starting on 30 January 2008, 21 UTC, at a 775 hPa starting-level. Black labels along the trajectories show backward times in hours.

The flight strategy was set in a way that the aircraft was flying from Cape Verde Islands following the 15° North meridian towards the African coast (see Fig. 4.4). The coastline of Senegal was crossed north of Dakar in an altitude of approx. 9 km a.s.l. to obtain HSRL data of the Saharan dust layer at the land-ocean transition without major contributions of anthropogenic pollution. Close to the eastern border of Senegal the Falcon left the lidar flight altitude and descended into the mineral dust layer at a distance of approx. 200 km east of Dakar over rural area. Within this layer the dust was probed in-situ upstream of Dakar and over the city area during the approach into DKR. Thereby flight altitudes for in-situ measurements reached from 900 m a.s.l. about 100 km east of Dakar to 400 m a.s.l. above the southern peninsula of Dakar, straight before the approach. After refueling the mineral dust loaded boundary layer was probed in-situ over the ocean downstream of Dakar. Then the Falcon climbed to the lidar altitude and measured the mineral dust layer from upstream of Dakar over the city area to the ocean. During the ascents to and the descents from the lidar flight altitude, a thin layer of biomass burning aerosol which extended from 2000 to 3500 m a.s.l. was traversed. The outgoing flight and the returned flight were labeled #290108a and #290108b and the further analysis will refer to these two flights.

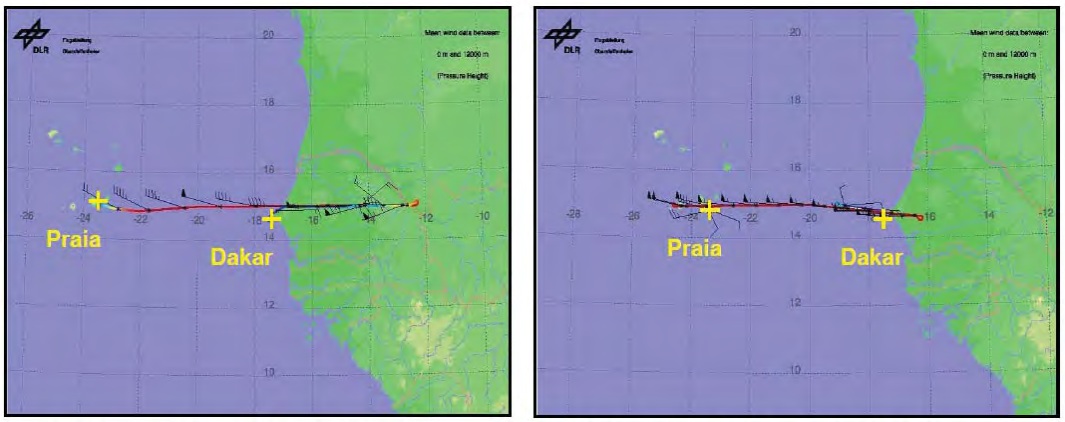

a) Flight pattern Praia - Dakar #290108a

b) Flight pattern Dakar - Praia #290108b

Figure 4.4: Flight Pattern for Falcon flight IDs #290108a (a) and #290108b (b): Vanes show wind speed and direction for recent flight level, flight track colors indicate flight altitude.

4.2 Results from the Basic Data Analysis

In this section data from the basic data analysis (which I made use of, but did not implement myself within this case study) are presented. The basic data analysis was created directly after the field experiments of the SAMUM-II measurement campaign and provides a composition of data plots for the entire flights. They form the mesoscale framework for the far more detailed analysis of this case study.
Besides the aerosol optical depth and extinction coefficient profiles, results from the in-situ basic data analysis show that there are indications for the detection of the Dakar plume. Those in turn serve as motivation for a detailed meteorological analysis.

4.2.1 HSRL data

Figure 4.5 shows a map of the flight path and the observed aerosol optical depth (AOD) data at 532 nm measured by the HSRL. Detailed values are compiled in Table 4.1. In all cases the HSRL extinction profile analysis was restricted to a minimum altitude of 200 m a.s.l. (for excluding ground return effects), whereas the maximum measurement altitude was determined by the flight altitude. These two levels form the upper and lower integration boundary of the height-dependent extinction coefficient to calculate the aerosol optical depth, see Equation 2.45.

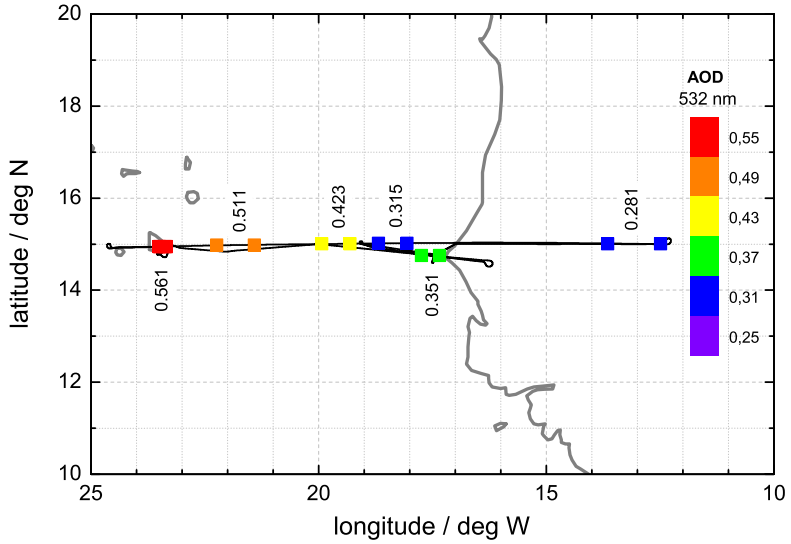

Figure 4.5: Flight patterns (black lines) and aerosol optical depth (AOD) values calculated from selected HSRL profiles for flights #290108a and #290108b, see Table 4.1 for measurement sequences and locations.

The aerosol optical depth of the mineral dust layer varies from 0.423 ± 0.081 at approx 300 km off the coast to 0.315 ± 0.057 at 120 km off the coast, and finally to 0.281 ± 0.055 over land 550 km away from the coastline, whereupon the layer height varies from 1.2 km over sea to 1.6-1.7 km over land. The increase in layer height and AOD from the West African coast towards the Cape Verde Islands is confirmed by satellite images of the dust outbreak which shows a clearly visible dust plume extending from about 20°W

towards the west while the and areas show less dust loadings (see also Fig. 4.1). Over the area of Dakar, an AOD of 0.351 ± 0.045 is measured which is significantly enhanced compared to the value of 0.281 measured over the rural area east of Dakar. Compared to the next western extinction profile of about 120 km off the coast (providing an AOD 0.315 ± 0.045) the enhancement in AOD over the Dakar area is less significant. But it has to be mentioned that the Dakar profile was measured at 17.55 UTC (during the return flight), whereas the off-shore and the rural area profiles were measured at about 13.25–14.40 UTC (during the outbound flight), some hours closer to the maximum of the dust storm episode.

Table 4.1: Location, dust layer height and aerosol optical thickness for selected positions of the dust plume probed during the flights on 29 January 2008 between Praia (Cape Verde) and Dakar (Senegal), minimum height used for the AOD analysis is 200 m a.s.l. The error refers to the statistical error of the extinction profile.

Location	Time UTC	Latitude deg N	Longitude deg W (start)	Longitude deg W (stop)	Layer height km a.s.l.	AOD (532 nm)
E Senegal	14.40	15.007	13.656	12.491	1.68	0.281 ± 0.055
Dakar	17.55	14.753	17.741	17.346	1.59	0.351 ± 0.045
Ocean 1	13.25	15.018	18.686	18.062	1.14	0.315 ± 0.057
Ocean 2	13.40	15.006	19.934	19.311	1.41	0.423 ± 0.081
Ocean 3	19.15	14.979	22.240	21.414	1.43	0.511 ± 0.037
Praia	20.00	14.947	23.490	23.349	1.16	0.561 ± 0.095

Besides the optical depth, extinction profiles provide further information about changes in mineral dust optical properties over the urban agglomeration of Dakar. Figure 4.6 depicts the profiles of extinction coefficients (at 532 nm) based on HSRL data over the Atlantic west of Dakar, over the region east of Dakar, and over the city of Dakar. These profiles reflect the different vertical extents of the dust layer over sea and over land. In comparison to the reference state over land ($\sigma_{ep,max} = 0.225\,\mathrm{km}^{-1}$ at approximately 500 m a.s.l.) the Dakar region shows a significant increase in σ_{ep}, especially within the lower boundary layer (250–500 m a.s.l.) featuring a $\sigma_{ep,max} > 0.275\,\mathrm{km}^{-1}$.

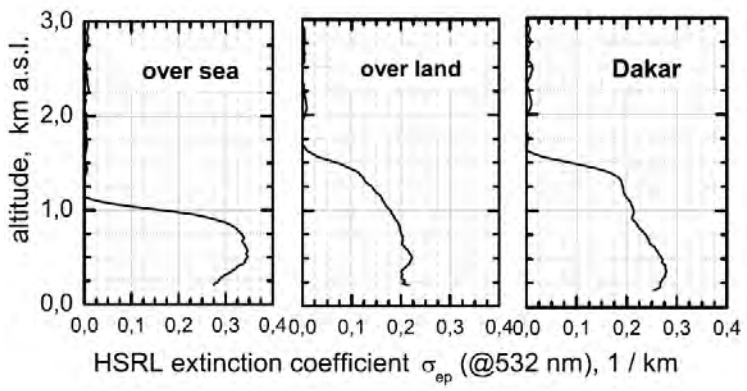

Figure 4.6: Profiles of the extinction coefficient from HSRL for selected sequences over sea, over land, and over the city of Dakar.

In summary both, AOD as well as extinction profiles, show significant changes in the mineral dust layer properties over the urban area of Dakar. This observations claims for a small scale analysis of the in-situ results in order to describe the local and mesoscale mixing effects of urban pollution with mineral dust.

4.2.2 In-situ measurements

During the approach into Dakar airport, signatures of an urban plume were crossed two times with pure mineral dust layer encounters in between. The very sharp changes with respect to total number concentrations, size distributions, volatility and absorption coefficient force the assumption that mineral dust and urban plume are clearly separated. Figure 4.7 summarizes the changes in total aerosol number concentration N4 ($d_p > 4\,\mathrm{nm}$) and N10 ($d_p > 10\,\mathrm{nm}$), number concentration of non-volatile particles with $d_p > 10\,\mathrm{nm}$ (nonvol N10), the fraction of non-volatile particles, i.e. the ratio (nonvol N10)/(N10), see cross-hatched area, and the PSAP raw signal at 660 nm for the approach into (left section) and the climb-out from (right section) Dakar airport. The flight altitude is added as thick gray line to exclude altitude related effects.

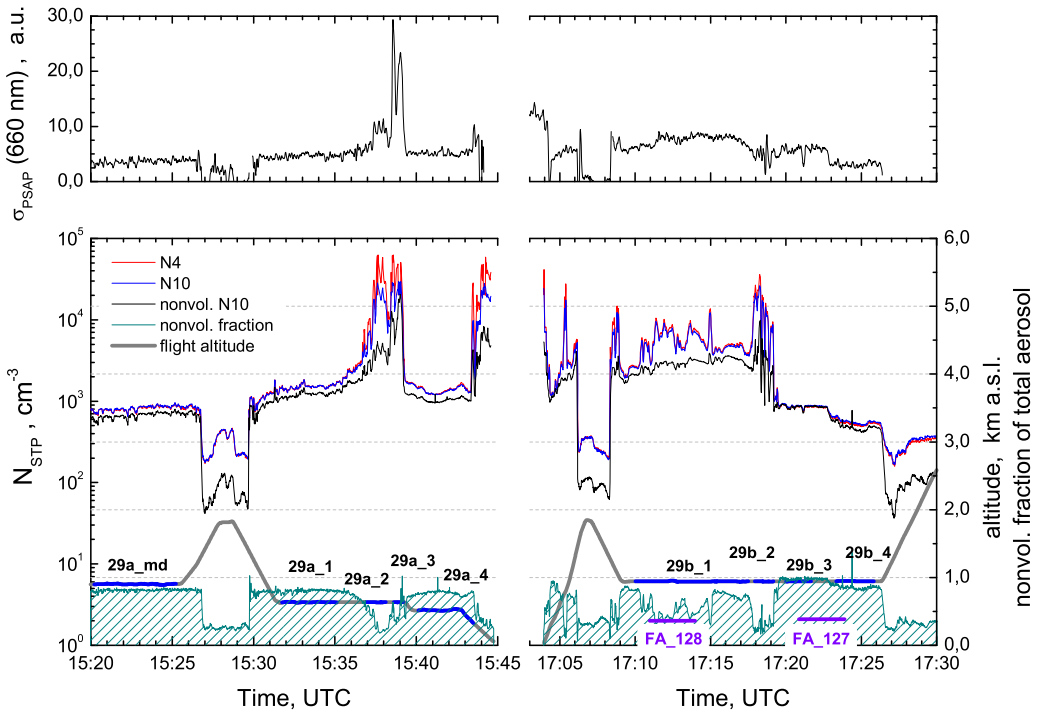

Figure 4.7: Total aerosol number concentrations N4 (all particles with $d_p > 4\,\mathrm{nm}$) and N10 ($d_p > 10\,\mathrm{nm}$) for approach and climb out Dakar. Shaded area shows fraction of non-volatile particles, sequences for chemical impactor samples are marked green. Additionally the gray line describes flight altitude to point out altitude effects.

In order to localize those flight sequences, where clear indications for the crossing of the Dakar plume are detectable, several flight sequences were marked in Fig. 4.8. This map of the Dakar agglomeration presents an overview of the geographical location where in-situ measurement sequences are located referring to the approach (labels 29_a). A

separate illustration of the return flight sequences (labeled 29_b) is not shown, because they all refer to measurements over sea, 10–50 km west of Dakar.
A detailed analysis of all these sequences will be presented in Subsection 4.3, but first it has to be analyzed, if the detected changes in aerosol microphysical and optical properties are really assigned to Dakar's urban pollution plume. Therefore a detailed meteorological analysis was elaborated to classify the measured aerosol and to assess the extension and the structure of Dakar's urban pollution plume.

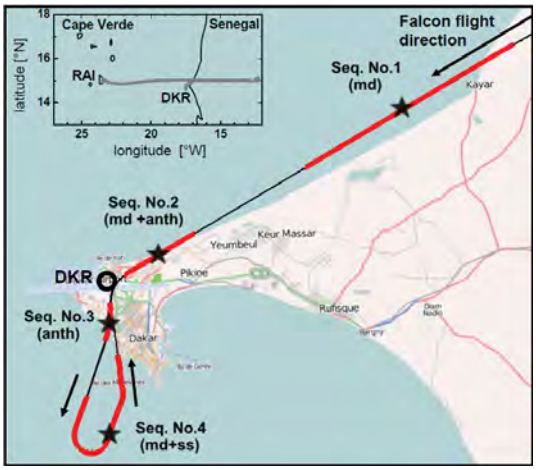

Figure 4.8: Map of the region of Dakar (www.openstreetmap.org) including the flight path during the approach to the airport; indicated are the sequences where different aerosol types like mineral dust (md), mineral dust mixed with anthropogenic pollution (md+anth), anthropogenic pollution (anth) and mineral dust mixed with marine aerosol (md+ss) were encountered. The Classification of the marked sequences is provided in Section 4.4, see Table 4.3.

4.3 Meteorological Analysis and Plume Structure

The characterization and investigation of the plume structure is an important part of this thesis, because the knowledge of extension and location of the plume forms the background for further investigation of the physico-chemical parameters. The detection of the plume source regions shall show evidence for the anthropogenic origin of the in-situ probed plume aerosol. As the plume is crucially influenced by the meso- and microscale circulation, the main focus of this chapter lies on the meteorological data analysis including in-situ measurements as well as backward trajectories and model results from the MM5. Furthermore the HSRL provides additional information on the appearance of the plume and the local circulation.

4.3.1 HSRL data and the local circulation pattern

The HSRL provides vertical cross sections of the aerosol backscatter and extinction coefficients as well as aerosol depolarization and lidar ratios. All mentioned parameters reflect variations of aerosol concentrations and types, but we will limit our considerations to backscatter ratios and aerosol depolarization at 532 nm. Additional cross section data of the other parameters can be found in the appendix.

As described above, flight #290108a crossed the coast line ca. 40 km north of Dakar, where the coast is sparsely populated. Thus measured values of aerosol backscatter and extinction can serve as an unpolluted reference state for the quantification of the Dakar plume. Figure 4.9 shows the HSRL backscatter profiles for the crossing of the coastline 40 km north of Dakar and directly above the urban area of Dakar.

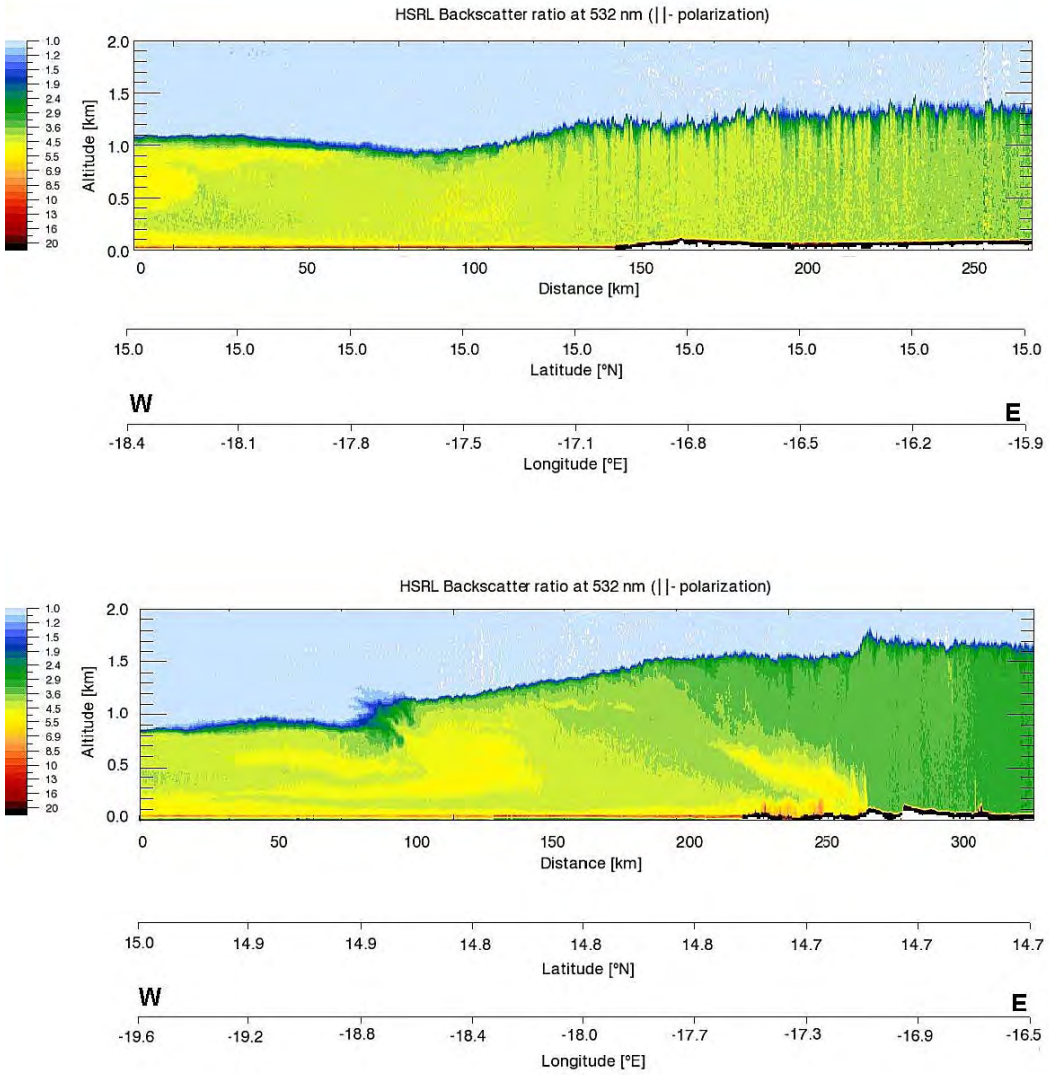

Figure 4.9: HSRL backscatter ratio coast line cross section for the region 40 km north of Dakar (upper) and straight over Dakar (lower). Viewing direction is south; see longitude and latitude information below the plots.

The northern profile represents homogeneous backscatter ratios of 3.5–4.5 including a zonal gradient but no evidence for urban pollution. In contrast the Dakar profile contains a lower background backscatter ratio of 2.5–3.5 and a clear plume signature with values up to 6.0 over the eastern part of the Dakar agglomeration. The lower (dust contributed) background backscatter ratio for the Dakar region is attributed to

the meteorological situation as the dust outbreak had already exceeded the climax on 29 January 2008 and the return flight crossed the coast line approximately 6 h after the outward flight. Furthermore a boundary layer height increase of 200 m depth can be observed over land during this period of time because of diurnal warming. The general zonal gradient of dust concentrations with the highest values near the Cape Verde Islands and the lower dust loadings over the continent is also detectable in the satellite images of Fig. 4.1. Moreover HSRL cross sections of the aerosol backscatter extinction and the aerosol lidar ratio (both at 530 nm) demonstrate similar results referring to the unpolluted reference state and the Dakar plume, see appendix Section B.

However, the observed structure of the coastal cross sections is worth a closer look at the urban area of Dakar. Figure 4.10 shows an enhanced section of 80 km distance reaching from the rural areas east of Dakar to the Atlantic Ocean west of Dakar.

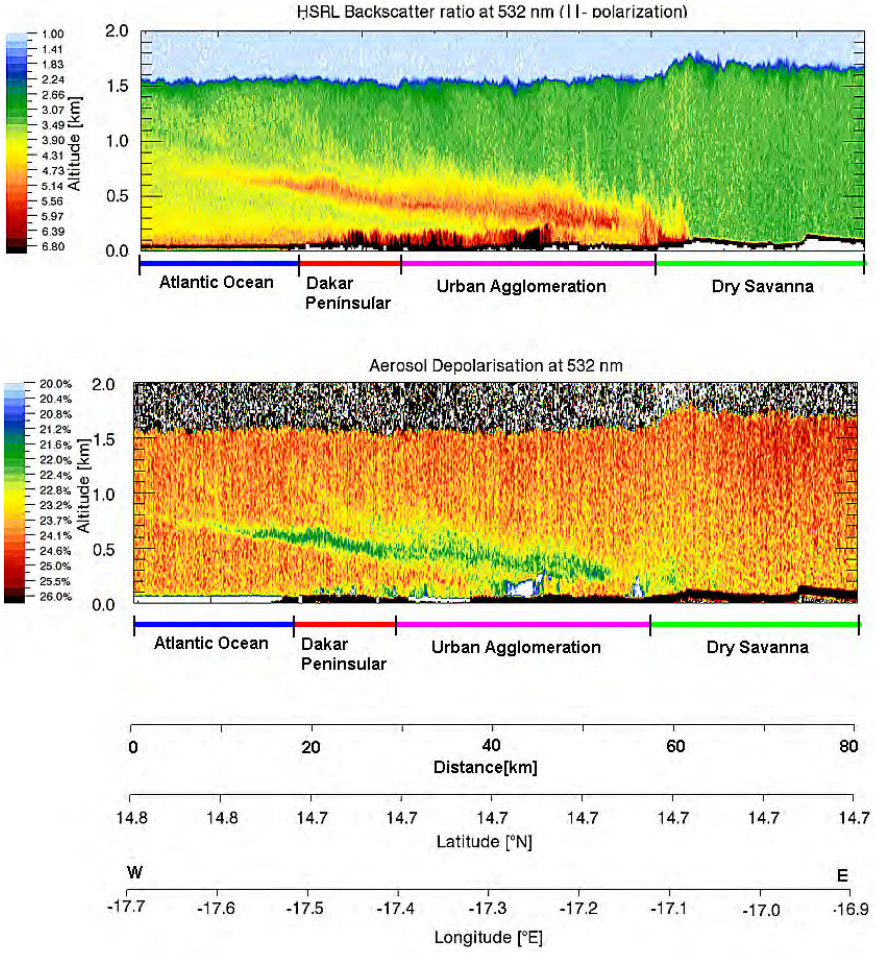

Figure 4.10: HSRL data shows the Dakar plume mixing into the mineral dust layer; the plume originates from an area east of Dakar; viewing direction is south.

The signature of the Dakar plume is clearly detectable in terms of the HSRL backscatter ratio. Thus the plume center is characterized as a layer of about 100–300 m depth ranging from 400 to 700 m a.s.l. located above the urban area of Dakar. Over the Atlantic, some km west of Dakar, the plume features effective dispersion. Even if a

Doppler lidar would be the preferred instrument to analyze mesoscale circulation patterns, in this case the HSRL backscatter ratio at 532 nm gives a good impression of the circulation pattern. It indicates stable conditions in the 0–200 m layer above the urban region of Dakar and reasonable convection 10–15 km east of Dakar (between 17.1° W and 17.2° W). While depolarisation ratios for dust background conditions indicate values $\geq 25\,\%$, depolarisation ratios within the plume show significantly lower values of approx. 21–22 %. The decrease in depolarisation can be attributed to the addition of sea salt and primarily anthropogenic sulphate aerosol particles which are closer to spherical shape than mineral dust. However, the indicated convection east of Dakar requires convergence in that region and this in turn means that the mesoscale westerly flow was replaced by an easterly flow within the lowest 200–300 m a.s.l. over sea. In combination with the stable layer above the western part of Dakar and the sea surface, one can assume the existence of a sea breeze circulation. Another feature of the circulation pattern can be observed west of Dakar in 700-800 m a.s.l. at 17.7° W (according to Fig. 4.10), where the plume gets significantly diffused and becomes rarely detectable at all. Because of the strength of the mesoscale flow and the mentioned structure of the HSRL profile, the observed sea breeze seems to appear only for some hours during the afternoon / early evening, whereas the strong mesoscale flow dominates the rest of the day and during nighttime. Furthermore the topography of the Dakar peninsula with hills up to 60 m can be assumed to influence the detailed structure of the sea breeze circulation and the Dakar plume to a certain extent.

4.3.2 ECMWF analysis data, synoptic data and Falcon in-situ data

Apart from the HSRL profiles, ECMWF analysis data offers a good estimation of the general circulation patterns in 925 hPa and 1000 hPa. These pressure levels were chosen according to the structure of the HSRL data and the supposed stratification described above. A closer look at the wind charts in Fig. 4.11 shows a significant suppression of the mesoscale westward flow in the lower level (1000 hPa) along the coast line. This feature is less distinctive at 15 UTC than at 18 UTC, when nearly calm conditions as well as northerly winds can be observed near Dakar. Furthermore convergence is detectable all along the coast line in the lower level. In the upper level (925 hPa) stronger easterly winds than in the vicinity are observed along the seaside of the coastline especially north of Dakar, where an increase of wind speed about up to 3 m/s (at 15 UTC) is observed. In contrast to the lower level, the occurrence of this phenomenon is limited to the 15 UTC analysis. Nevertheless, the observation of a stronger upper and a weaker low level flow linked to low level convergence indicates a typical sea breeze circulation that weakens the mesoscale flow near surface and enforces the mesoscale flow in the upper boundary layer. Moreover the Dakar peninsula and its special geographical position evokes a significant small scale structure of the circulation.

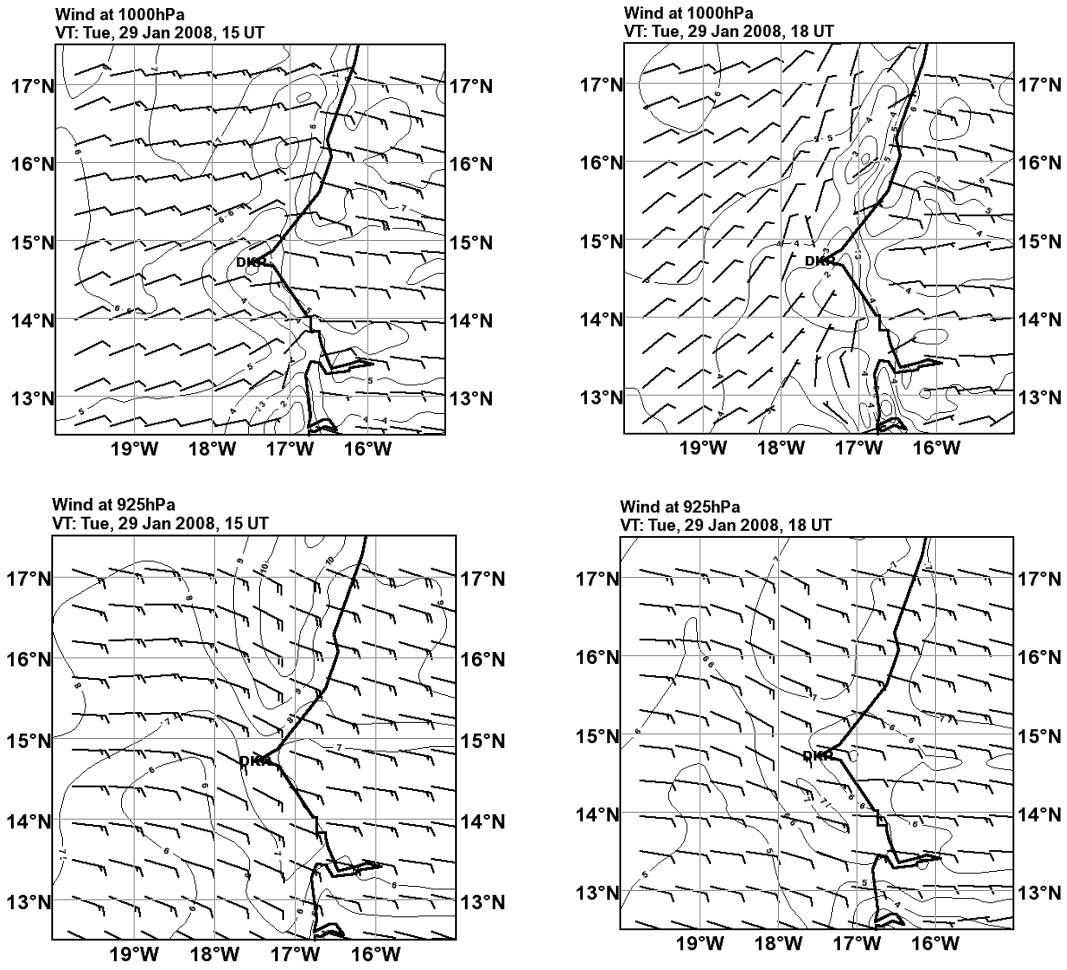

Figure 4.11: 1000 hPa (upper) and 925 hPa (lower) wind fields of the coastal region near Dakar (DKR) with a contour interval of 1 m/s. Data source: ECMWF analyses.

Table 4.2: ECMWF analysis and synoptic data for Dakar airport (WMO 61641), 29 January 2008, 15 UTC.

Data Source	Temp / °C	Rel Hum / %	Wind Speed / ms^{-1}	Wind Dir / °
Synops	28.6	31	4.1	15-24
ECWMF	23.8	61	2.5	63.5

The only synoptic measurements that are available for the region of greater Dakar are from Dakar Yoff airport (WMO 61641), which is situated at the north western edge of the Dakar peninsula 26 m a.s.l. and less than three km away from the sea. A comparison of synoptic data from Dakar airport and the corresponding ECMWF analysis data grid point for 15 UTC (which is 45 min before the Falcon approach) is shown in Table 4.2. All parameters show large differences between the extrapolated ECMWF and the measured synoptic data. The synoptic data present features of continental, dry and warm air masses, whereas the ECMWF data suggest that the sea breeze should already have flooded Dakar. However, the synoptic data for 12 UTC which hold temperatures of 31.5 °C and a relative humidity of 12 % together with northerly winds at 15 UTC force the conclusion that the maritim air masses have already entered the Dakar peninsula, but due to friction imposed by buildings and the hilly orography the warm air masses are not yet completly suppresed. Thus, even if the ECMWF data proofs the existence of the mesoscale sea breeze circulation in general, the analysis data of this scale (horizontal grid resolution of $0.225° \times 0.225°$) neglects microscale features of the sea breeze circulation as one can see according to the comparison with synoptic data. The disability of a correct representation of the sea breeze within the ECMWF data leads to a significant uncertainty of short scale back trajectories based on this data. As the following interpretation of aerosol in-situ data is crucially dependent on the exact characterization of the source regions and the structure of the plume within the context of back trajectories, it is worth investigating further effort to get a more precise picture of the circulation pattern.

Additionally to the ECMWF analysis and the synoptical data, meteorological in-situ data from the Falcon are available for approach into and climb out from Dakar airport (for approach at about 15.30 UTC, see Fig. 4.12. The potential temperature profile provides evidence for the lidar profile based suggestion of a stable layer from 0–250 m. Above that layer a well-mixed, statically neutral boundary layer indicates the continental origin of these air masses determined by mesoscale westward flow. Strong wind shear as well as large variations in wind speed can be observed from the surface up to about 300 m a.s.l. The anticlockwise rotation of the wind direction with height indicates cold air advection which is in agreement to our previous estimation of the cool sea breeze that enters the land surface.

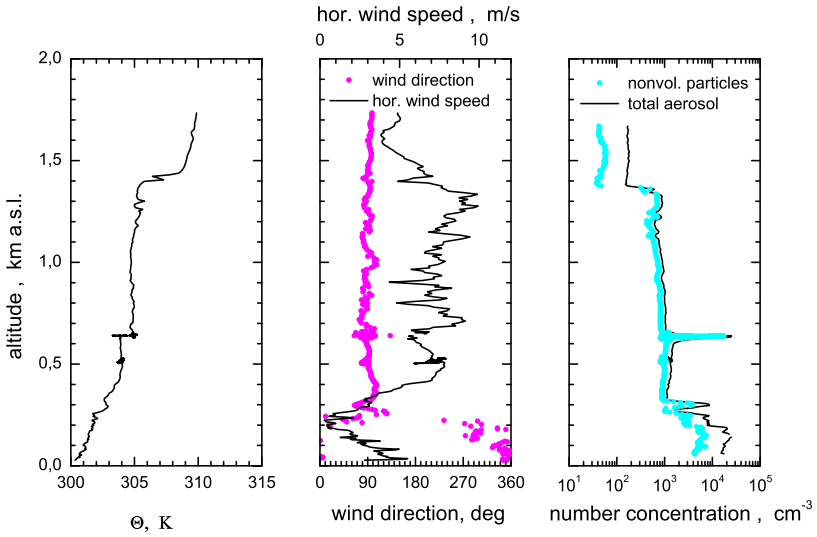

Figure 4.12: Vertical profiles of potential temperature Θ (left), horizontal wind speed and wind direction (mid) and of particle number concentrations ($d_p > 10\,\mathrm{nm}$) and accumulation mode ($d_p > 0.1\,\mu\mathrm{m}$) measured during the approach into the airport of Dakar at about 15.45 UTC, 29 January 2008.

The right plot in Fig. 4.12 shows a vertical profile of the aerosol particle number concentration. At an altitude of 640 m a.s.l. the flight pattern possesses a constant level sequence, whereupon the Dakar peninsula was crossed. The fact that a strong variation of aerosol particle number concentration is observed at this flight level demonstrates that the Dakar plume was crossed during this sequence. It has to be noted that the maximum number concentration measured at the altitude of 640 m a.s.l. coincides with the maximum number concentration measured during the approach to Dakar airport at an altitude of 200 m a.s.l. This finding is in line with the HSRL profile shown in Fig. 4.10, which locates the lofted urban pollution plume over Dakar at the same altitude as in-situ measurements. Furthermore the small scale variations due to air mass origin over Dakar can also be observed in terms of the potential temperature, which varies about 2 K during the crossing of the Dakar peninsula.

In summary the inaccuracy of the ECWMF wind charts shows that there are open questions referring to the strength and appearance of the sea breeze. Besides the inset time of the sea breeze, the detection of convective areas responsible for vertical transport of urban pollution and the range of the inland penetration form the key questions according to further investigation of the the plume. Therefore the high resolution weather prediction model MM5 was run. The model results will be described in the next Subsection 4.3.3. Nevertheless, ECMWF data and Falcon in-situ data give evidence of the existence and the general structure of the sea breeze circulation.

4.3.3 MM5 model results

The results from the MM5 modeling form an important part of this thesis, because they provide a considerable contribution to the understanding of the plume structure. A detailed description of the model set-up adapted to the special requirements of this study has already been provided in Chapter 3.2.3. It has to be mentioned that Domain D02 was chosen for all of the following plots for two reasons: On the one hand domain D02 has a resolution high enough to study small scale features and on the other hand flight tracks and trajectory calculations exceed the borders of domain D03 (providing the highest resolution) very often, whereas domain D02 offers a good basis for these investigation. Nevertheless, the results of D02 are of course related to the even higher resolution domain D03 by two-way nesting. Furthermore data plots of domain D03 (for vertical velocity at $\sigma = 0.985$ can be found in the appendix. Taking into account the in-situ aerosol measurements which refer to flight altitudes of 400–900 m a.s.l. as well as urban emissions originating from the surface, all parameters are discussed for the altitudes between the surface and 1 km a.s.l. In regard of the sea breeze features, the following parameters were selected for discussion: Horizontal wind speed and direction, vertical velocity and relative humidity. Furthermore trajectories for specific flight levels and vertical soundings for Dakar airport (DKR)were calculated.

Vertical Velocity

Low level convection over Dakar is a necessary condition for vertical transport of Dakar's anthropogenic pollution and therefore it requires special attention. Figure 4.13 shows the development of the sea breeze in terms of vertical velocity and horizontal wind speed and direction at $\sigma = 0.985$ which is equivalent to about 150 m above the surface. Time intervals of 2 h were chosen for this summary figure, but the appendix provides also half hourly data. At 11 UTC (3.5 h after sunrise) the circulation is dominated by the mesoscale westward flow. Significant subsidence is observable at the lee side along the ridge 30 to 50 km east of Dakar, whereas there is no evidence for the existence of a sea breeze. Two hours later significant low level convection is observable over the northern part of the Dakar peninsula with mean vertical velocities up to $10\,\mathrm{cm\,s^{-1}}$. Further convective regions are located along the seaside north and south of Dakar, but vertical velocities are nearly everywhere considerably smaller than over Dakar and the regions of ascent are to a large extent seated over sea. There are two reasons that serve as explanations for the early and extensive inset of the sea breeze over the Dakar peninsula: orographic effects (the Dakar peninsula includes hills up to 60 m) and the existence of an urban heat plume of Dakar implemented by the land use parametrization. At about 13 UTC at least parts of the urban pollution from Dakar are transported into greater heights and contribute to the urban pollution plume. Along the ridge of the hilly interior subsidence is still present at the lee side, but with weaker occurrence than at 11 UTC. Moreover the mesoscale flow decreases because of mesoscale effects, whereupon the wind direction over land remains the same. In contrast there is significant rotation observable along the coast line over the sea with clockwise rotation south of Dakar and anti-clockwise rotation north of Dakar (attributed to the slope of the coast-line). All these observations are contributed to the development of the sea breeze circulation which is not yet distinctive but rudimentary existent at 13 UTC.

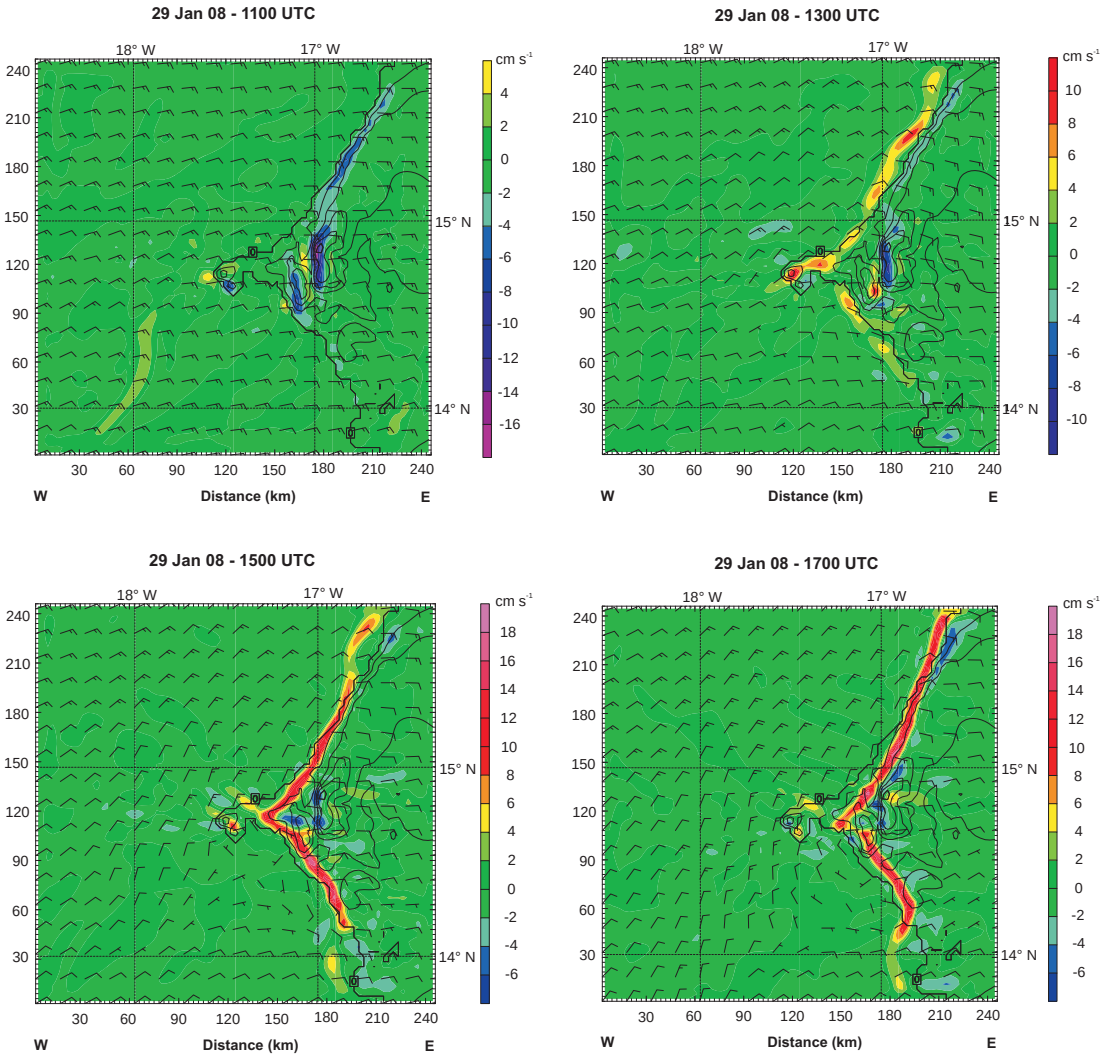

Figure 4.13: MM5 results for vertical velocity (contours) and horizontal wind (black vanes) at $\sigma = 0.985$ on 29 January 2008, 11 UTC (top left), 13 UTC (top right), 15 UTC (bottom left) and 17 UTC (bottom right); black lines show orography in intervals of 20 m.

Two hours later, at 15 UTC, low level convection is fully developed nearly all along the coast line. The region of significant ascend moves inland and forms a belt with mean vertical velocities up to 16 cm s^{-1}. The low level convection is nourished by low level convergence clearly detectable by the oppositional direction of wind vanes along the coast line north and south of Dakar. Especially southeast of Dakar there is a region where the mesoscale flow at $\sigma = 0.985$ is completely suppressed and easterly winds predominate. All in all the sea breeze circulation is now (7.5h after sunrise) completely developed. As the sea breeze has already exceeded the Dakar peninsula, there is no significant vertical velocity observable apart from a small region located straight in the middle of the peninsula. The absence of significant lifting is attended by northerly winds over the northern part of the peninsula and indifferent wind conditions over the southern part. Therefore pollution within the plume which is attributed to convection around 15 UTC originates from the regions 10–30 km east of the Dakar peninsula. These region are part of the Dakar agglomeration and the bay east of Dakar is densely populated. Furthermore it contains several industrial pollution emitants (a big oil refinery, a cement factory and others).
At 17 UTC the structure of the sea breeze does not differ significantly from the situation at 15 UTC. The zone of low-level convection has moved some km inbound and the mean vertical velocity shows maxima of 18 cm s^{-1}, but the structure of convergence is quite similar to 15 UTC. Furthermore the sea breeze appears to diffuse at the ridge of the hilly area east of Dakar and the northerly winds north of Dakar increase in speed. The Dakar peninsula as such features no significant descending or lifting any more and therefore one can assume that only pollution from the areas east of Dakar can contribute to the aerosol plume. 17 UTC was chosen as the last point in time in Fig. 4.13, because the data analysis of in-situ measurements is limited to the time before 18 UTC. All in all the parameters vertical velocity and horizontal wind speed and direction provide a detailed impression of the modeled sea breeze circulation. Thus these parameters clarify the special importance of the Dakar peninsula: The sea breeze starts and collapses significantly earlier than north and south of the peninsula.

Relative humidity of different height levels

Relative humidity does not only serve as tracer for the transition of the sea breeze near surface, but it also provides a tracer for low level convection and thus for the appearance of Dakar's urban aerosol plume. Since the results from the relative humidity near the surface support the vertical velocity data, no completely new conclusions can be drawn. Therefore relative humidity at ground level will not be discussed here, but half hourly data is available in the appendix.
Figure 4.14 shows a sounding of the grid point Dakar airport (at 15 UTC) that explains why relative humidity can serve as a tracer for convection. The layer from the surface up to 200 m a.s.l. is characterized by a narrow temperature inversion and increasing dew points with height. Above that layer, from 980 to 820 hPa the dew point decreases rapidly from over 10 °C to -20 °C, whereupon at the same time the temperature decreases only about 5 K. That means that the stratification is quite stable and air parcels need significant dynamically induced lifting for ascend. If air masses are lifted by the sea breeze circulation, they carry moist air into the much dryer layers of the upper boundary layer. Additionally dry adiabatic cooling leads to a further increase of the relative humidity. Thus the observation of moist bubbles in levels from 950 to 850 hPa can serve as a detection method for surface-near air that was raised up to these levels.

If these bubbles in turn originate from a region of large urban pollution, this pollution is lifted and accounts for the Dakar plume which was detected by the HSRL (see Fig. 4.10).

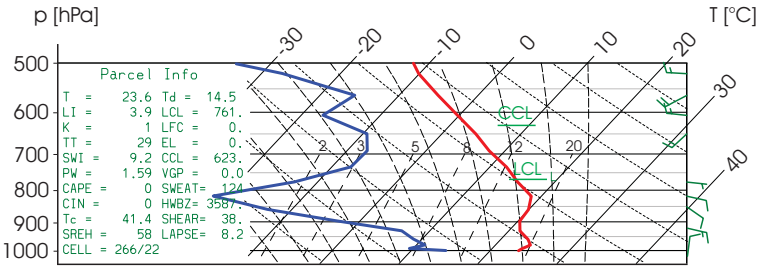

Figure 4.14: MM5 modeled vertical sounding for Dakar airport. The red and blue lines demonstrate the vertical temperature respectively the dew point profile.

In order to investigate the bubble-like structure of convection it is worth taking a look at horizontal distributions of relative humidity at different pressure levels first. Referring to the Falcon flight levels of in-situ measurements, modeled relative humidities for 900 m respectively 640 m a.s.l. were chosen for this analysis. The point in time (15.30 UTC) corresponds to the Falcon overflight of the Dakar peninsula at about 15.30–15.45 UTC. Figure 4.15 shows where the sea breeze induced low level convection carries up moist air from the ground level to greater heights. In general the most humid air can be found seaside along the coast line with higher values of relative humidity in 640 m a.s.l. than in 900 m a.s.l. (as expected due to the sounding). Furthermore the maximum values are observable around the southern part of the Dakar peninsula reaching relative humidities up to 40 % in 900 hPa and 50 % in 640 hPa, respectively. Apart from the sea breeze related increase of moisture along the coast-line, also several interior regions posses increased relative humidities, which are related to convection in the context of diurnal variations. The dry continental "background" air provides very low relative humidities between 5 and 20 % in 900 hPa. Both levels show westerly winds all over the domain with no significant deviation near Dakar. That means that once pollution from the ground has reached these heights it is directly transported westward by the mesoscale flow. However, the high relative humidity over the Dakar peninsula does not originate from the Dakar peninsula because of the superposition of the mesoscale flow and the sea breeze circulation. To prove this assumption, back trajectories will be presented in the following.

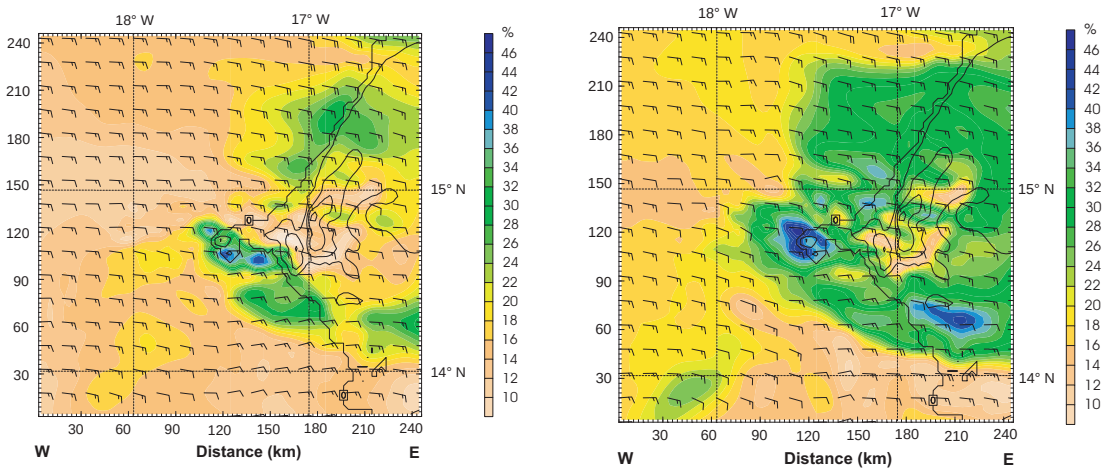

Figure 4.15: Contour plots for relative humidity 900 m a.s.l. (left) and 640 m a.s.l. (right) for 29 January 2008, 15.30 UTC. Additionally wind speed and direction in the particular heights are given.

Back trajectories

Based on the MM5 model output also back trajectories can be calculated. According to the Falcon in-situ measurements over the Dakar peninsula, a starting level of 640 m a.s.l. was chosen for discussion. The calculated trajectories reach back from 15.30 UTC to 11.00 UTC in order to include all relevant convective processes. Fig. 4.16 shows a composition of 20 back trajectories starting along the flight pass of the Falcon aircraft during approach to DKR. Blue and green trajectories refer to starting points north of the Dakar peninsula, whereas the reds are related to trajectories starting directly over the Dakar peninsula.

The left plot reflects the (south) easterly mesoscale flow, whereupon three of the red trajectories slightly drop out of the bulk. Those three trajectories can be retrieved nearest to the ground in the vertical cross section. They show extensive lifting 20–40 km east of central Dakar and can serve as representatives for air parcels which carry up polluted air from the surface to the level of airborne measurements. All of the red trajectories represent reasonable ascend, but only a few of them touch those layers near the ground (0–200 m) where uptake of local urban emission is reasonable. Fig. 4.16 shows small scale differences within the bulk of the red trajectories. That in turn means that the measured in-situ data crucially depends on the exact location of measurement. In contrast the blue and green trajectories starting north of the Dakar peninsula never touch pressure levels higher than 975 hPa. Along with the horizontal movement over less populated areas no significant pollution is expected for these Falcon in-situ sequences.

Similar considerations for the return flight in-situ sequences west of Dakar also show upward motion east of central Dakar, but the backward trajectories do not descend as low as for the approach sequences (two plots analogous to the approach section are presented in Fig. 4.17). Therefore one can assume that less anthropogenic pollution is found in the aerosol in-situ measurement for the return flight sequences, because the air masses west of the sea breezes are far more stable and convection, which raises highly polluted air, is suppressed.

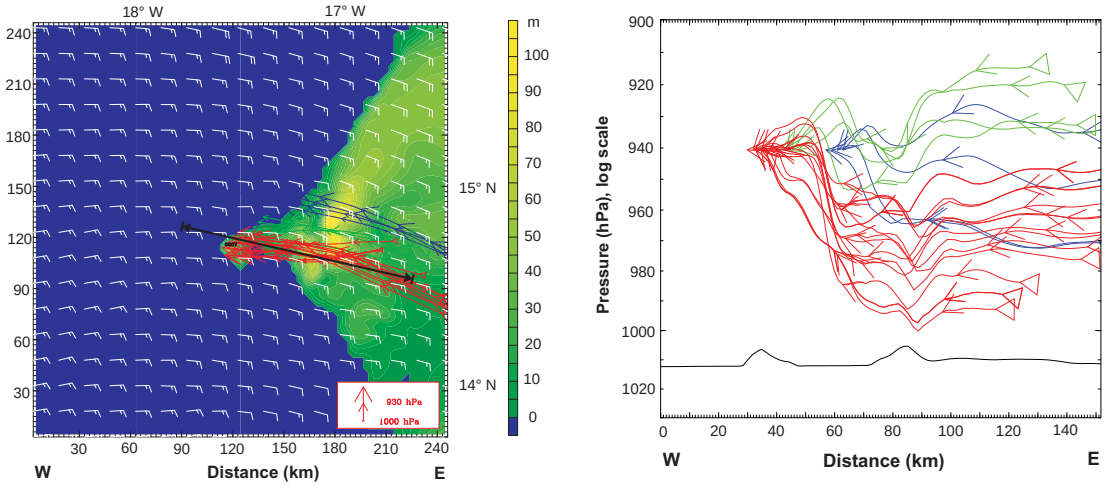

Figure 4.16: Back trajectories for in-situ measurement sequences starting on 29 January 2008, 15.30 UTC at 640 m a.s.l. The left plot shows a horizontal illustration of the trajectories. Trajectory colors refer to measurement sequences along the flight path. On the right hand side a vertical cross section for all trajectories marked in the left plot is given. The cross section demonstrates an excerpt of DOMAIN D02, which is marked in the left plot by a black line.

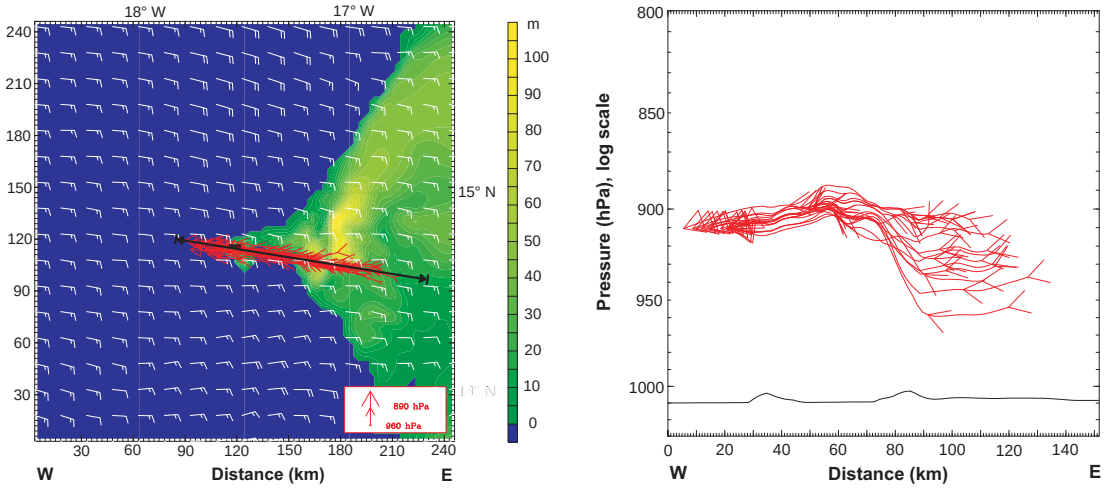

Figure 4.17: Back trajectories for in-situ measurement sequences starting on 29 January 2008, 17.30 UTC at 900 m a.s.l. The left plot shows a horizontal illustration of the trajectories (marked in red). On the right hand side a vertical cross section for all trajectories marked in the left plot is given. The cross section demonstrates an excerpt of DOMAIN D02, which is marked in the left plot by a black line.

It has to be mentioned that the exact appearance of convection is based on the Gayno-Seaman planetary boundary layer (PBL) parametrization scheme and the use of other parametrization schemes leads to small scale differences. Running the MM5 model with a MRF PBL scheme (see Section Dudhia et al. (2005) for explanation) carried out results which did not differ much, but the resolution of the moist bubbles was significantly smaller. For this reason and as Gayno-Seaman can be estimated as state-of-the-art all considerations are limited to the Gayno-Seaman PBL.

Summary of the model results

Modeling of the small scale sea breeze circulation with the MM5 turned out to be a helpful and innovative tool for investigation of the plume structure. In contrast to in-situ and ECMWF data, the model results provide high resolution data for the whole region of interest. The parameters relative humidity, wind speed and direction and vertical velocity serve to determine the local circulation as well as soundings and back trajectories. The results are listed in the following:

- The MM5 output confirms the existence of the sea breeze circulation. It forms between 11–13 UTC all along the coast line north and south of Dakar and moves inbound during the afternoon. Locally the sea breeze is able to suppress the westward mesoscale flow completely so that eastward winds are observable at the western edge of the sea breeze.
- The Dakar peninsula takes a special position as the extensive low level convection appears and disappears first in this region.
- In terms of the mean vertical velocity the sea breeze possesses a line-like structure apart from punctual convection over the Dakar peninsula. Furthermore relative humidity serves as a good tracer for convective bubbles.
- Mean vertical velocities up to $18\,\mathrm{cm\,s^{-1}}$ are detectable within the convective region of the sea breeze, relative humidities locally rise from 5–15 % up to 40 % in 900 m a.s.l.
- The landward penetration of the sea breeze varies along the coast line and has an extension between 5 and 20 km.
- Partially back trajectories show significant lifting of air parcels which are probed in-situ over the Dakar peninsula, whereas for trajectories starting north of Dakar no crossing of the lowest 200 m is observable.

A comparison of MM5, Falcon and synoptic data as well as discussion of the boundary layer parametrization scheme in the framework of results from literature will follow in Chapter 5.

4.4 Physico-Chemical and Optical Properties

In Section 4.2 first results from the basic data analysis have been provided to demonstrate the indications for the detection of Dakar's urban pollution plume. Section 4.3 validated the anthropogenic origin of the measured aerosol and described the plume structure in detail. In the following section a detailed analysis of the changes in physico-chemical and optical mineral dust properties referring to mixing with anthropogenic pollution will be presented. Results for the changes in size distribution and volatility will be part of the analysis as well as consideration of the absorption coefficient, single scattering albedo and the Ångström exponent of absorption. At last a composition of results from chemical analysis and the three-component model of the PSAP data analysis scheme will be given, including refractive indices and soot mass concentrations.

4.4.1 Particle microphysical properties

All sequences which serve for analysis of optical and microphysical properties of the Dakar plume and the unpolluted reference state are marked blue along the gray altitude line (labels 29a_ and 29b_) in Fig. 4.7. The following aerosol type and aging time classification is based on the analysis of the sampling location combined with back-trajectory analyses. The aerosol type was classified by MM5 trajectories, because these trajectories are able to provide the necessary resolution to detect anthropogenic aerosol source region. The approximate plume aging times were obtained from both, MM5 and Lagranto back trajectory analyses since these time scales are determined by the mesoscale flow. The aging times refer to the time when the sampled air mass left the coast.

The measurement sequences were characterized as mineral dust (md), anthropogenic (anth) and sea salt (ss) and combination of these classes. Thereby the notation "anth" does not mean that this sequence posses only anthropogenic aerosol, but it is the dominant aerosol type referring to the microphysical and optical properties. Results for aerosol microphysical and optical properties are compiled in Table 4.3 for the different aerosol types encountered during the Dakar study. This summary provides all information about aging times, volatility parameters and results from the PSAP data analysis scheme, namely absorption coefficients, Ångström exponents of absorption, refractive indices and the effective chemical composition. Specific results which determine the characteristics of the plume will be discussed in the following.

Table 4.3: Aerosol properties for different aerosol types encountered during the flights on 29 January 2008; data are obtained from the PSAP data analysis scheme and from particle thermodenuder methods. Uncertainties correspond to 1-σ of sequence averages.

Seq. No.	29a_md	29a_1	29a_2	29a_3	29a_4	29b_1	29b_2	29b_3	29b_4
Altitude, m a.s.l.	903	636	636	637	499	943	942	943	946
Time start	15:01	15:32	15:37	15:38	15:40	17:10	17:18	17:20	17:23
Time end	15:25	15:35	15:38	15:39	15:43	17:17	17:19	17:22	17:26
Aerosol type	md	md	md+anth	anth	md+ss	md+anth	md+anth	md+ss	md+ss
Approx. ageing time	n.a.	n.a.	0h	0h	<1h	1-2h	3h	6h	6-7h
Fraction of	0.80	0.81	0.35	0.47	0.77	0.60	0.29	0.97	0.85
nonvolatile particles	±0.02	±0.02	±0.15	±0.12	±0.03	±0.15	±0.08	±0.02	±0.05
σ_{ap} (467nm), 1/Mm	2.97	4.14	6.80	16.37	4.56	6.29	3.75	4.62	2.58
	±0.39	±0.26	±1.24	±3.44	±0.23	±0.52	±1.05	±0.71	±0.29
σ_{ap} (530nm), 1/Mm	1.44	2.10	4.20	11.96	2.47	3.73	2.28	2.31	1.16
	±0.14	±0.15	±0.82	±2.60	±0.15	±0.33	±0.62	±0.35	±0.14
σ_{ap} (660nm), 1/Mm		0.13	1.67	7.37	0.43	1.17	0.79		
	±0.10*	±0.10	±0.37	±1.69	±0.10	±0.12	±0.24	±0.10*	±0.10*
å$_{ap}$(467/660)		9.96	4.05	2.31	6.82	4.87	4.49		
	n/a *	±1.06	±1.16	±0.72	±0.63	±0.63	±1.84	n/a *	n/a *
Re (467nm)	1.548	1.549	1.550	1.553	1.549	1.549	1.549	1.548	1.548
Re (530nm)	1.546	1.547	1.548	1.552	1.547	1.547	1.548	1.546	1.546
Re (660nm)	1.544	1.549	1.546	1.549	1.545	1.545	1.545	1.544	1.544
Im (467nm)× 10^{-3}	2.00	2.30	3.90	8.70	2.50	3.10	3.60	2.20	1.80
Im (530nm)× 10^{-3}	1.20	1.30	2.50	6.40	1.50	2.20	2.30	1.00	0.90
Im (660nm)× 10^{-3}	0.00	0.10	1.10	4.30	0.30	0.80	0.90	0.00	0.00
Quartz, vol-%	99.80	99.76	99.49	98.61	99.72	99.59	99.54	99.80	99.83
BC, vol-%	0.00	0.04	0.25	0.97	0.08	0.19	0.20	0.00	0.00
Fe-Oxides, vol-%	0.20	0.20	0.26	0.42	0.21	0.23	0.26	0.20	0.17

* value was below the limit of detection of 0.1 Mm-1.

Particle number size distributions are presented in Figure 4.18 for the dust layer east of Dakar, over the city of Dakar, west of Dakar and east of Praia. No significant differences are observed for the size range $d_p > 1\,\mu$m. Largest differences are found for $d_p < 0.3\,\mu$m. The increase in the Aitken mode ($d_p < 0.1\,\mu$m) over land and in particular in the Dakar plume corresponds to the presence of an externally mixed mode of secondary particles in the aerosol which vanishes during the transport of the dust over sea due to dilution and altering processes. The size distributions measured west of Dakar and east of Praia are almost similar although the two sites are separated by a distance of approx. 500 km. The slightly enhanced coarse and accumulation mode east of Praia can be contributed to the general characteristics of the dust storm episode which have already been described before. The observation of similar Aitken modes suggests that the modification of the aerosol size distribution by atmospheric dilution and processing is completed soon after the air mass has left the coast and no more emissions are mixed in from the ground. Thus the evolution of the size distribution corroborates the results from the plume structure analysis, which describe the plume as a significant, but locally limited phenomenon.

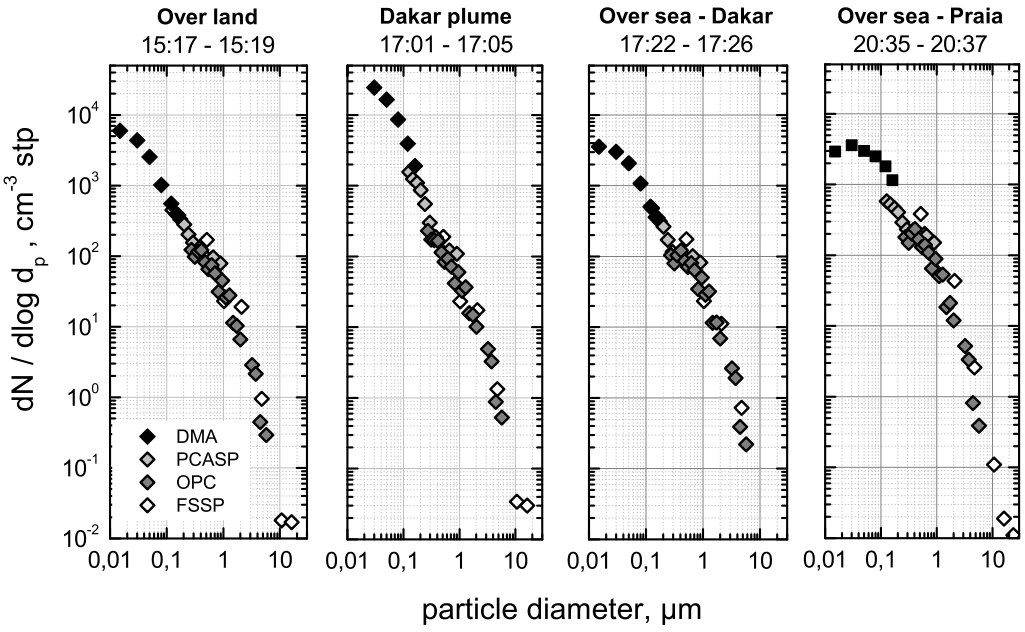

Figure 4.18: Particle size distributions measured in the mineral dust layer at 900 m a.s.l. from left to right: east of Dakar over land, Dakar plume, west of Dakar over sea, and east of Praia over sea. The plot caption shows the measurement techniques for the different size intervals.

A closer look at the modification of the aerosol size distribution by urban emissions is presented in Fig. 4.19, which show the relative increase in the number concentrations measured in the size channels of the PCASP instrument. As reference case we selected the particle size distribution measured inside the dust layer at a distance > 100 km east of Dakar. The labels of the size distributions correspond to the sequences indicated in

Fig. 4.7 and Table 4.3. Upper channel diameters refer to a complex refractive index of $1.545 + 0.0009i$.

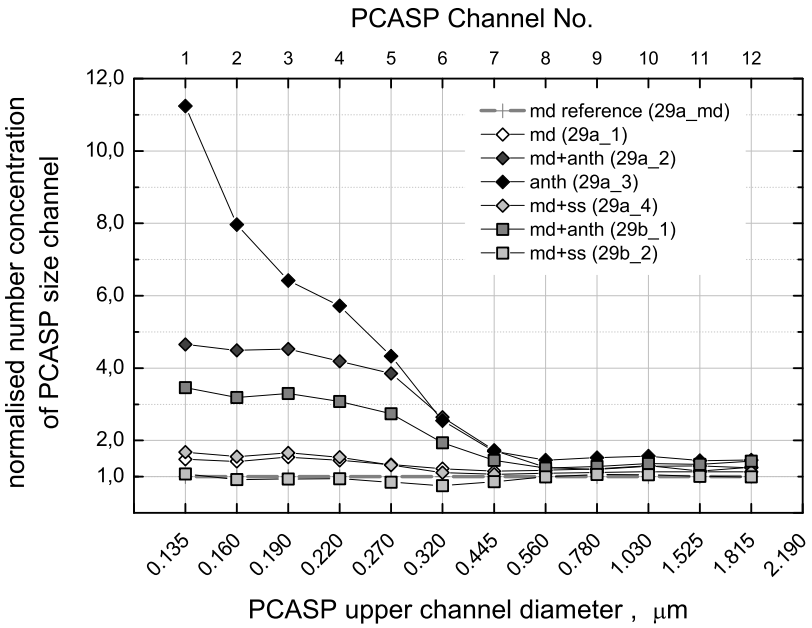

Figure 4.19: Relative increase in particle number concentration per PCASP size channel; size spectra are normalized to the spectrum measured east of Dakar over rural area.

In Fig. 4.19 we can distinguish three different size ranges: for particles with $d_p > 0.5\,\mu$m we don't see any significant modification by urban emissions; for particles with $0.2\,\mu\text{m} < d_p < 0.5\,\mu$m we see an increase by a factor of six compared to unperturbed dust. The strongest effect of the urban emissions is found for particles with $d_p < 0.2\,\mu$m. In the size range covered by the PCASP ($d_p > 0.135\,\mu$m) particle number concentrations are increased by up to a factor of 12, while for sub-100 nm sized particles this increase is as large as a factor of 60, see Fig. 4.18. On the other hand, this mode of nanometer-sized particles diminishes rapidly, while the enhanced fraction in the size range of 0.2–0.5 μm is less changed in the outflow after 6 h of atmospheric processing.
Furthermore the volatility analysis of the measured aerosol is of special interest. Fig. 4.20 (for aerosol type classification see Table 4.3) shows the nonvolatile fraction of the aerosol (left panel) and the contribution of the sub-μm aerosol to absorption (right panel, see next section for details).
The urban pollution plume is characterized by a strong externally mixed mode of secondary volatile particles which contributes 65-70 % of the total aerosol by number. East of Dakar over rural area, there was already an externally mixed mode of volatile particles present contributing 20 % to the particle number concentration, while west of Dakar over sea after 3–6 h of ageing, this mode had almost vanished. We interpret this observation in the following way: over land with its farming activities and even more over the city area with its urban pollution, secondary aerosol particles form from surface gaseous emissions while over the ocean the supply of condensable gases is strongly reduced and the externally mixed mode of secondary particles is rapidly depleted by coagulation.

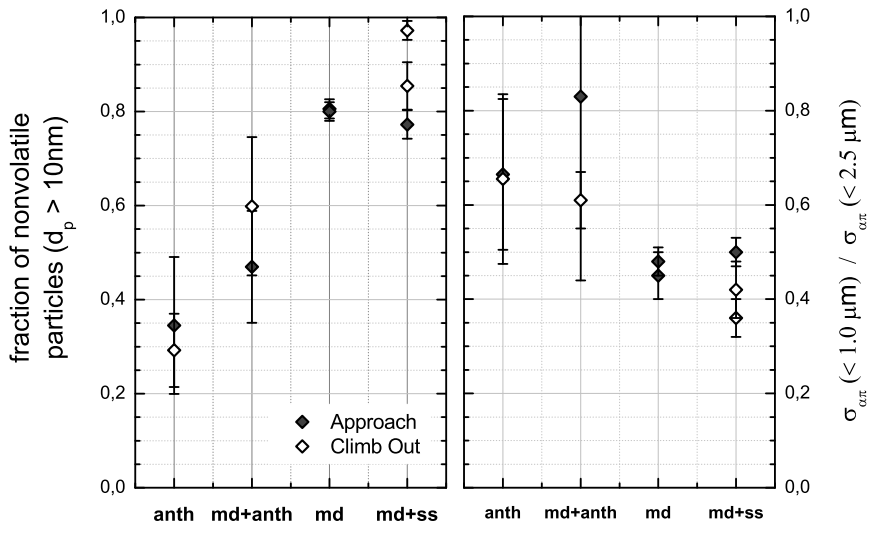

Figure 4.20: Left: Fraction of non-volatile particles of the total aerosol for $d_p > 10\,\mu$m for aerosol samples taken at different distances from the source region. Right: Ratio of sub-μm absorption to total absorption for $d_p < 3.0\,\mu$m. Aerosol types anthropogenic (anth), anthropogenic mixed with mineral dust (md + anth) and mineral dust mixed with sea salt (md + ss) were identified by back trajectory analyses.

In order to detect trends in volatility within the Dakar plume, Fig. 4.21 provides scatter plots of 6-s measurement intervals for approach and climb-out. Two characteristic features are observable: The mineral dust dominated sequences show only little variations in volatility with generally increased particle number concentration over the Dakar peninsula (Seq 29_1 and 29_4), whereas the mineral dust sequences downstream Dakar (Seq 29b_3 and Seq 29b_4) indicate pure mineral dust aerosol due to the negligible volatile fraction. Moreover the anthropogenic dominated sequences provide no distinctive trend in terms of volatility fraction correlating to the total number concentration. The highest number concentrations (N10 $> 10000\,\mathrm{cm}^{-3}$) exhibit a wide range of volatility fractions reaching from 40 % (Seq 29a_3) to > 80 % (Seq 29b_2 and Seq 29a_2).

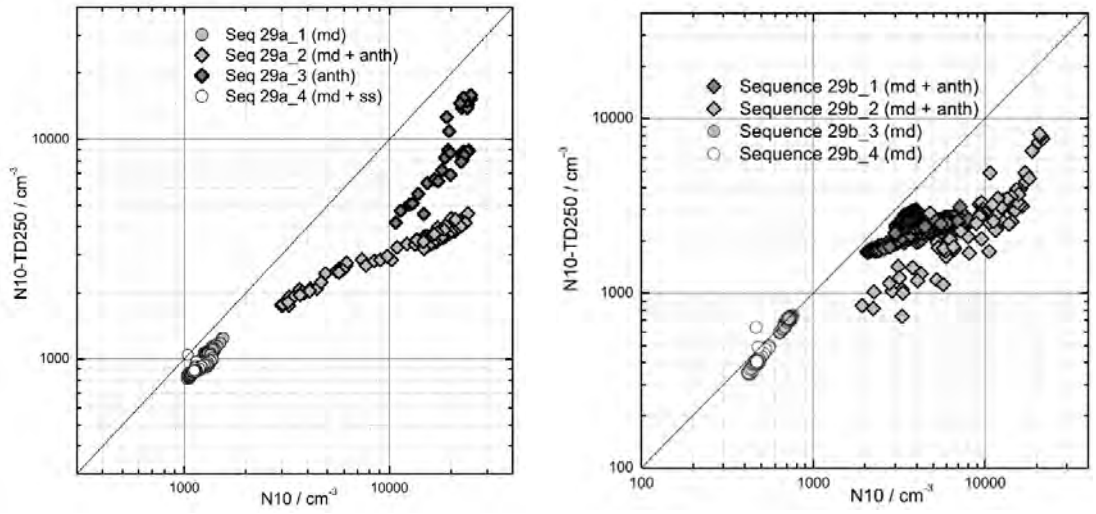

Figure 4.21: Scatter plot of number concentrations N10-TD250 (non-volatile particles $d_p > 10\,\mathrm{nm}$) and N10 (volatile + non-volatile particles) for flight sequences approach (left plot) and climb-out (right plot) Dakar. Measurement locations for approach are shown in Figure 4.8.

4.4.2 Particle optical properties

The analysis of particle optical properties is mainly based on the PSAP data analysis scheme providing results of absorption and extinction related parameters. Revisiting Fig. 4.20, right panel, sub-μm sized particles contribute 65–85 % to aerosol absorption at 530 nm in the urban pollution plume embedded in the dust layer, while in the absence of urban pollution, this fraction is reduced to approx. 40–50 % for unperturbed dust. In order to determine the anthropogenically induced absorption coefficient the differences in absorption coefficients at 660 nm are evaluated. In this spectral region, dust is only very weakly absorbing and the observed differences can be attributed entirely to anthropogenic emissions. From background sequences 29a_md, 29a_1, 29b_3, and 29b_4 a background absorption coefficient of $0.100 \pm 0.016\,\mathrm{Mm}^{-1}$ is calculated (see data in Table 4.3); for comparison, $\sigma_{ap}\,(530\,\mathrm{nm}) = 1.753 \pm 0.542\,\mathrm{Mm}^{-1}$. Subtracting this background value from the absorption measurements conducted in the vicinity of Dakar, the anthropogenic contributions to $\sigma_{ap}\,(660\,\mathrm{nm})$ are obtained. Table 4.4 summarises the results.

Table 4.4: Anthropogenic contribution to aerosol absorption and respective soot mass concentrations in Dakar.

Sequence No.	29a_2	29a_3	29b_1	29b_2	29a_4
anthr. $\sigma_{ap}(660)$, 1/Mm	1.57	7.27	1.07	0.69	0.33
anthr. $\sigma_{ap}(530)$, 1/Mm	2.45	9.94	1.98	0.53	0.72
anthr. frac. $\sigma_{ap}(660)$, %	94	99	91	86	75
anthr. frac. $\sigma_{ap}(530)$, %	58	85	54	23	29
anthr. BC, $\mu g/m^3$	0.36	1.33	0.27	0.07	0.10
BC mass, %	0.141	0.576	0.117	0.030	0.042
SAMUM-1 (Wagner et al., 2009)					
BC mass frac., %	0.104	0.423	0.085	0.022	0.031
OPAC (Hess et al., 1998)					
PSAP scheme BC mass-%	0.143	0.562	0.107	0.117	0.043

Over the city area urban pollution contributes more than 95 % to aerosol absorption at 660 nm while this fraction decreases to 75 % in the area west of the city over the sea. For the wavelength of 530 nm, where dust contributes significantly to absorption, the respective fractions are 85 % and 23 %. From the fact that for 530 nm, the maximum anthropogenic contribution to absorption (85 %) and the contribution of sub-μm aerosol to absorption (also about 85 %) are almost similar, we conclude that the black carbon particles are confined to $d_p < 1.0\,\mu$m and no internal mixing with coarse dust mode particles has occurred. The wavelength dependence of the absorption coefficient as expressed by the absorption Ångstrom exponent $\mathring{a}_{ap}$ is in all cases considerably larger than the value of 1.0 which is expected for pure urban aerosol (Kirchstetter et al., 2004; Bergstrom et al., 2007); see Table 4.3.

Figure 4.22 describes the decrease in $\mathring{a}_{ap}$ due to mixing with urban soot aerosol. Even if the intrusion of soot leads to a significant change of $\mathring{a}_{ap}$, mineral dust still dominates the absorption spectral dependence, otherwise values of $\mathring{a}_{ap}$ would range far beyond 2. According to Petzold et al. (2009) the uncertainty of this method can be estimated as $\pm\Delta\mathring{a}_{ap}/\mathring{a}_{ap} = 20\,\%$.
Besides the spectral dependence of the absorption, the PSAP data analysis scheme also provides information about the wavelength-dependent single scattering albedo ω_0 of the measured aerosol. At this point it has to be recalled that all single scattering albedo values refer to the size range $d_p \leq 3.0\,\mu$m. The values of ω_0 for the three wavelengths of the PSAP are summarized in Fig. 4.23. Sequence 29a_3 (anth), which represents the crossing throughout the plume center, holds the lowest values of ω_0 due to enhanced absorption by soot particles. For a wavelength of 530 nm, an $\omega_0 > 0.979 \pm 0.009$ was found for mineral dust, whereas an $\omega_0 = 0.907 \pm 0.027$ was observed in the plume center. Also for sequences with less anthropogenic pollution (md + anth) a significant decrease in ω_0 can be observed in comparison to the pure mineral dust sequences.

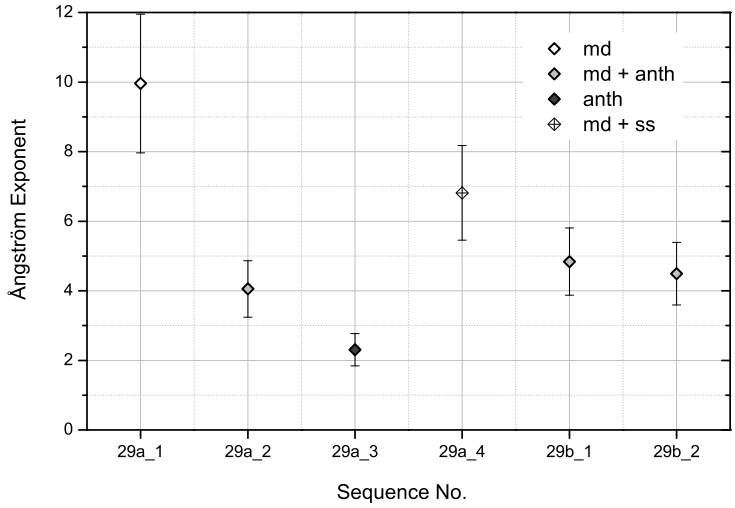

Figure 4.22: Ångström exponents for various sequences presented in Table 4.3. Error bars refer to Petzold et al. (2009), see text for details.

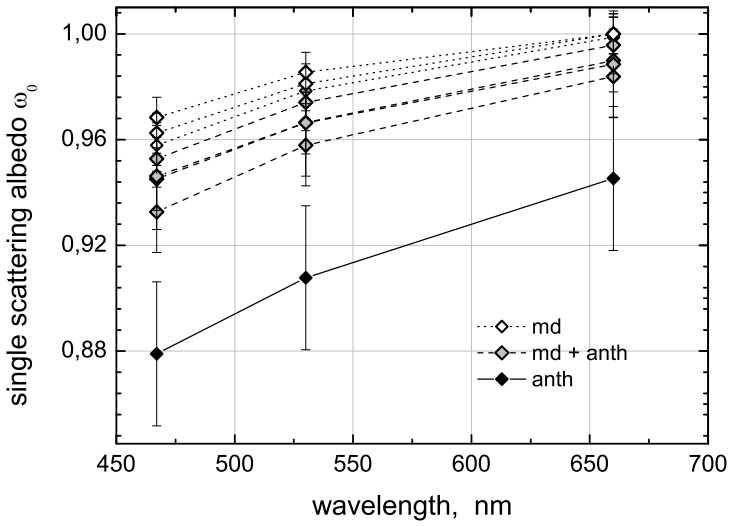

Figure 4.23: Singe-scattering albedo ω_0 of the sub 3.0 μm fraction determined from the PSAP data inversion scheme (Petzold et al., 2009). Values of ω_0 are provided for the PSAP wavelengths $\lambda = 467\,\mathrm{nm}$, $\lambda = 530\,\mathrm{nm}$ and $\lambda = 660\,\mathrm{nm}$. The aerosol type classification refers to Table 4.3.

4.4.3 Particle chemical composition and refractive index

The refractive index crucially depends on the chemical composition, therefore the results from the PSAP data analysis scheme are presented together with the effective chemical composition (also based on the PSAP data analysis scheme) and the results from single particle chemical analysis. A composition of the measured refractive indices for 530 nm referring to the sequences presented in Table 4.3 are shown in Fig. 4.24. The given error bars show the standard deviation of the PSAP analysis scheme which have been discussed in Chapter 3.2.2. It has to be mentioned that due to the simplified three component model an additional inaccuracy has to be assumed referring to the real part of the refractive index, but this systematic error is negligible for the imaginary part. Figure 4.24 shows that the addition of BC to mineral dust increases the imaginary part of the refractive index at 530 nm by more than a factor of 6 for the anthropogenic dominated sequence. The other anthropogenic influenced, but not dominated sequences also present a trend to an increase in k by a factor two, but the increase is less significant. A Comparison to literature shows that although there is a significant impact on the light absorbing properties of dust, the imaginary part of the complex refractive index is still within the natural variability of mineral dust from different sources, see e.g. Petzold et al. (2009). Thus mineral dust with a higher iron content, e.g. described by Quinn et al. (2004) and Lafon et al. (2006), could match the same imaginary part as the anthropogenic polluted mineral dust of the Dakar plume.

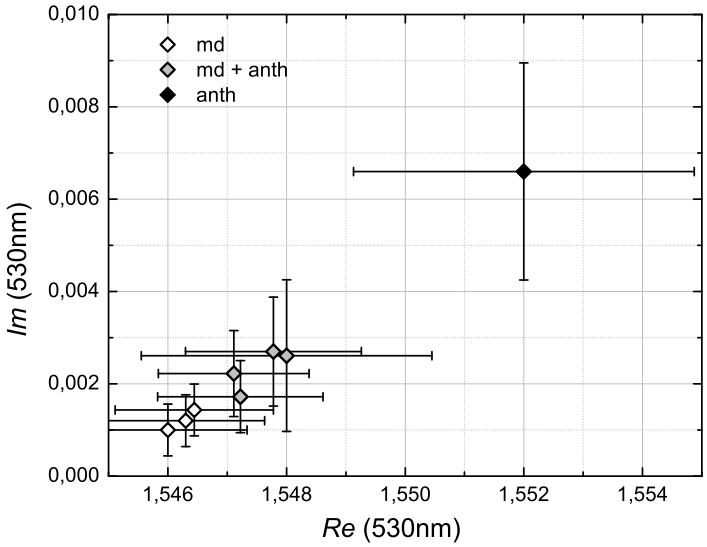

Figure 4.24: Real part (x-axis) and imaginary part (y-axis) of the complex refractive index at 530 nm for mineral dust (md), dust – black carbon mixtures (md + anth), and aerosol dominated by anthropogenic emissions (anth), collected in the vicinity of Dakar.

Based on the calculated complex refractive index, the PSAP data analysis scheme provides an idealized effective chemical composition resting upon quartz, hematite and soot. The results for the Dakar approach and climb-out sequences (see Table 4.3) are given by Fig. 4.25. Even if the results from the three-component model represent only an effective chemical composition, the Dakar plume is detectable in terms of a significant

soot fraction of $1.028 \pm 0.434\,\%$ vol for the heaviest measured pollution (Seq 29a_3) and also the soot fractions of the other sequences with anthropogenic pollution show significant soot contents. The soot fractions are not as high as one could expect within the center of the plume. As size distributions show, soot is only present for particle diameters $d_p < 500\,\mathrm{nm}$, therefore and according to the high mineral dust background, the results (given in % vol.) are traceable. Apart from Seq 29a_3 the iron oxide content varies only within one standard deviation i.e. the PSAP data analysis represents a very consistent background dust loading (see right part Fig. 4.25). The enhanced hematite fraction of the Dakar plume can be referred to other absorbing aerosol fractions which are not implemented in the PSAP data analysis scheme.

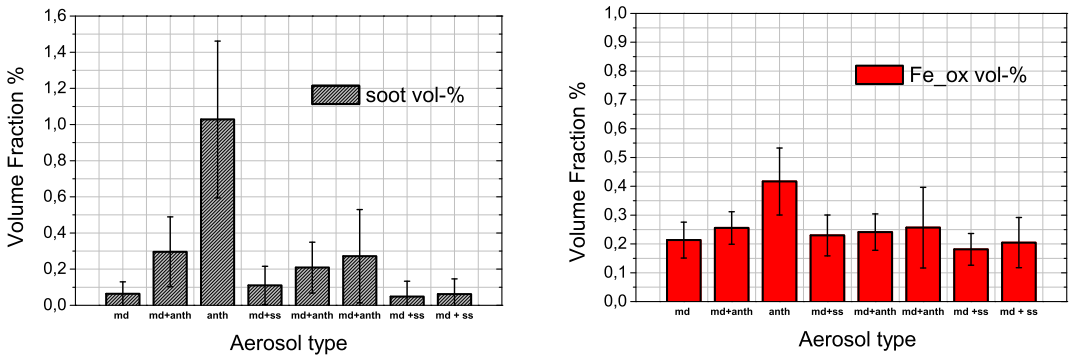

Figure 4.25: Volume fractions of soot (left) and hematite (right) calculated by the PSAP data analysis scheme. The classification of aerosol types refers to Table 4.3.

The anthropogenic contribution to absorption (see Table 4.4) was used to calculate the anthropogenic BC mass concentration by applying the mass-specific absorption coefficient of $7.5\,\mathrm{m^2/g}\,(530\,\mathrm{nm})$ from Bond and Bergstrom (2006). According to Hess et al. (1998) the anthropogenic BC mass concentration M_{BC} can be calculated by $M_{BC} = f\frac{\sigma_{ap}}{C_{ap}}$ where C_{ap} is the mass absorption cross section and f describes the anthropogenic contribution to absorption. Respective values for BC mass concentrations are listed in Table 4.4.
Applying a mass-specific extinction efficiency of $0.87\,\mathrm{m^2/g}$ ($\lambda = 530\,\mathrm{nm}$) (Wagner et al., 2009) to the extinction profiles measured by the HSRL, they can be converted into dust mass concentration profiles by calculating $M_{dust} = \frac{\sigma_{ep}}{C_{ext}}$. Assuming an average extinction coefficient of $\sigma_{ep} = 0.2\,\mathrm{km^{-1}}$ (see Fig. 4.6), an average dust mass concentration of $230\,\mu\mathrm{g/m^3}$ is obtained. Using the OPAC value (Hess et al., 1998) of $0.64\,\mathrm{m^2/g}$ for the mass-specific extinction efficiency of dust, the respective mass concentration is $313\,\mu\mathrm{g/m^3}$. These values can be used as lower and upper estimates for the dust mass concentrations in Dakar. Assuming that the dust mass concentration in Dakar is dominated by the dust advected from the east, the BC mass fraction of the Dakar aerosol can be calculated from the values listed in Table 4.4. Thereafter a comparison to the data obtained from the PSAP inversion scheme is possible. All three values for the BC mass fractions show very good agreement for nearly all sequences. The values compiled in Table 4.4 show that the soot mass fraction of the total aerosol was below 1 % mass for all sequences and a maximum mass concentration of $1.33 \pm 0.56\,\mu\mathrm{g/m^3}$ was calculated.

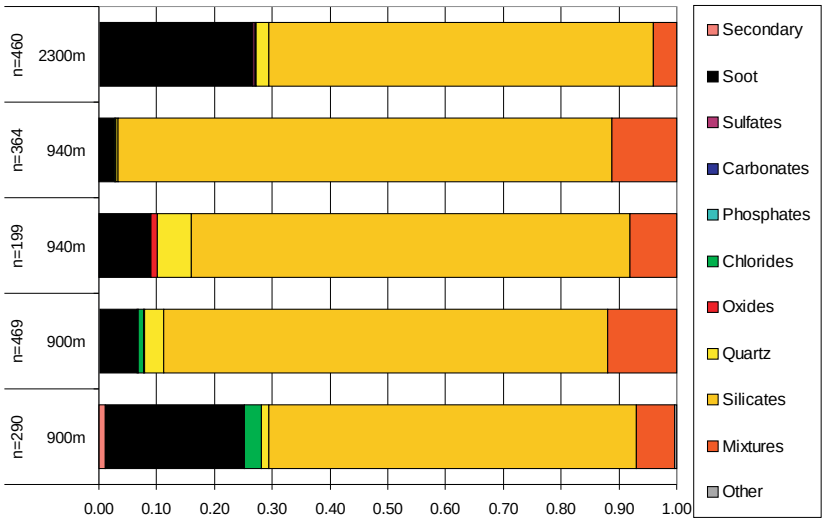

Figure 4.26: Number fraction of particles of specific chemical composition in the size range smaller than 500 nm in diameter; impactor sample numbers are FA_131, FA_130, FA_129, FA_128, and FA_127 (from top to bottom).

Besides the idealized effective chemical composition also real chemical analysis are available for special sequences (which are not conform to the sequences of Table 4.3). The two sequences of impactor samples for chemical analysis are marked in Fig. 4.7 (see labels FA_127 and FA_128) to get a rough estimate, what the microphysical parameters of these sequences look like. The single particle chemical compositions were derived from impactor samples by means of an elemental analysis using SEM-EDX. Figure 4.26 summarizes the abundance of mineralogical compounds by number. These impactor samples were collected during the flights #290108a and #290108b, whereupon only small particles with diameters $d_p < 0.5\,\mu$m were analyzed.
From the dust-dominated cases sample FA_127 shows the highest fraction of carbonaceous particles in the sub-500 nm part although the sample was collected at some distance away from the coast. In contrast, sample FA_128, which was collected closer to the coast shows the lowest fraction of carbonaceous particles in the sub-500 nm fraction. Sample FA_131 was collected in a thin lofted biomass-burning aerosol layer at 2300 m a.s.l. which originated from Central African savanna fires. In this layer also a large fraction of carbonaceous agglomerates is found. In the samples FA_127 and FA_128, which were collected over the sea, few chloride-containing particles were found.
However, PSAP analyses yield a black carbon volume fraction of 8.4 % and an aerosol absorption Angstrom exponent of 1.20 for this sequence. For particles larger than 0.5 μm in diameter (projection diameter), no carbonaceous particles were observed, and the aerosol is always mineral dust-dominated. TEM images of soot agglomerates of impactor sample FA_127 show that all detected particles are in an external mixing state (personal communication to Kirsten Lieke). Thus, the analysis of the impactor samples provide strong evidence, that (1) carbonaceous (soot) particles were present exclusively as external mixtures, and that (2) carbonaceous particles already present in the dust east of Dakar, originating most likely from biomass burning regions.

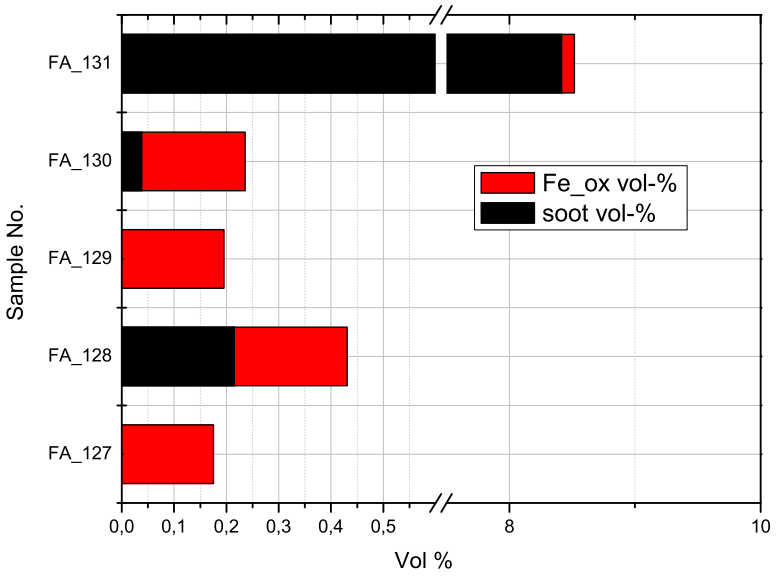

Figure 4.27: Iron oxide and soot volume ratios for impactor sample sequences calculated by the PSAP data analysis scheme. The time sequences used for the PSAP data analysis coincide with the impactor samples sequences described in Fig. 4.26.

The chemical impactor sequences mentioned above were also calculated by the PSAP data analysis scheme, results are presented in Fig. 4.27. It is of great importance that the volume fractions presented in Fig. 4.27 are not at all comparable to the impactor samples (see Fig. 4.26). Only for FA_131 (the biomass burning sample) both results are approximately comparable, because this sequence refers to a size distribution with only very few particles with $d_p > 500\,\mathrm{nm}$. For all other samples the dust particles with diameters $d_p > 500\,\mathrm{nm}$, which form the major contribution to volume are discounted in the chemical analysis, but taken into account in the PSAP data analysis. Furthermore the volume fractions of the PSAP effective chemistry are not directly transferable into number fractions of the impactor samples, because soot particles usually appear only in the sub-300nm fraction. Therefore the soot number fractions of the impactor samples for FA_131 (28 %) generally supports the lower volume fraction of appr. 8 % found by the PSAP effective chemical analysis. Nevertheless, the tendency of the soot fractions should similar for both methods according to samples FA_127 to FA_130, but at this point the PSAP data and the impactor samples are incompatible. A discussion of this problem will be given in the next chapter.

Chapter 5

Discussion and Conclusions

In this chapter a discussion about the results presented in Chapter 4 is given. Besides an evaluation of the sensitivity, accuracy and reliability of the analyzed data, conclusions referring to the basic questions of this study are drawn and constrains of investigation are demonstrated. Furthermore in this context the results are also compared to literature and an estimation of the further development of the plume is provided. Analogously to the preceding parts of this study, this chapter is divided into two main sections: a discussion on the plume structure and a discussion on the change in physio-chemical and optical dust properties due to mixing with the Dakar plume.

5.1 Plume Structure and Meteorological Analysis

In summary the results from HSRL, ECMWF, Falcon in-situ and MM5 modeling data provide a consistent picture of the local circulation pattern. The performance of the mentioned data varies referring to the different problems of investigation. According to the questions on the general plume structure, the sea breeze circulation and the vertical as well as the mesoscale transport of Dakar's urban pollution, every single analysis method provides important information. The HSRL data provides a very distinctive and descriptive picture of the overall plume structure. In addition ECMWF and MM5 data is capable of providing an estimation of the mesoscale circulation pattern which is of great importance due to the long range transport of the plume. Trajectory calculations confirm the anthropogenic origin of the plume aerosol.
Table 5.1 provides a simplified performance estimation of the used analysis methods according to different issues of investigation. Thereby the classification of performances is based on the results which were presented in Chapter 4.3, see Table 5.2.

Table 5.1: Overview of analysis method performances used for investigation of the plume structure.

Parameter	Falcon HSRL	ECMWF/LAGRANTO	Falcon in-situ	MM5
General Plume Structure	+		o	o
Mesoscale Wind Pattern		+		++
Vertical Profiles Dakar	o	o	++	++
Local Trajectories		-		+
Long Range Trajectories		++		o

Table 5.1 shows that only the combination of all different data sources provides a detailed estimation of the meteorological situation and the plume appearance. All parameters of this summary are discussed in detail in the following. As the results from MM5 modeling include the most comprehensive part of the meteorological analysis and at the same time plenty of literature is available for evalutation of the MM5 studies, the focus of evaluation lies on the MM5 model results. HSLR, LAGRANTO and Falcon results will be compared among each other and general uncertainties are discussed as far as possible.

Table 5.2: Classification of analysis method performances used in Table 5.1.

Symbol	Meaning
	no claim for analysis
-	analysis method fails for this problem
o	only rudimentary or side information available
+	basic conclusions provided
++	excellent and detailed performance

5.1.1 General plume structure

The appearance of Dakar's anthropogenic aerosol plume is characterized by a well-defined layer of significantly increased particle number concentration, changes in optical properties (measured in-situ) and increased backscatter ratio and optical depth (both measured by HSRL remote sensing) compared to the surrounding. According to Weitkamp (2005) supermicron-sized desert dust generates lidar depolarization ratios δ up to 0.25, whereas strongly absorbing soot shows significantly lower values for δ. Similar depolarization ratios are presented in this case study. Thus the HSRL data serves as a reliable instrument to analyze features of the small scale plume structure, namely location, vertical and horizontal extension, and dispersion.
In general the plume shows ascend in east-west-direction, whereupon the initial convective lifting takes place in a region 10–30 km east of Dakar. Over the Dakar region the plume is limited to a thin, lifted layer at 400 to 700 m a.s.l., but considerable dispersion is observable at the plume edges and becomes dominant over sea. This assumption based on lidar and in-situ data is proved by trajectory calculation of the MM5 model results.

5.1.2 Sea breeze circulation

The mesoscale wind pattern determines the plume structure as well as the long range transport of the polluted air masses and is therefore an important subject of discussion. On the one hand the mesoscale flow is dominated by the zonal geostrophic wind, on the other hand the local sea breeze circulation has crucial influence on the boundary layer flow. The phenomenon of the sea breeze circulation is observable in all meteorological data sets and additionally even in the HSRL plots. Therefore there is no doubt about

the existence and the importance of the sea breeze. In particular, all variables related to the structure of the planetary boundary layer (PBL) are used to have a strong influence on the fate of airborne aerosols (Shafran et al., 2000). The vertical extension of the Dakar sea breeze respectively the post-frontal marine boundary layer is found to be 150–250 m according to Falcon in-situ measurements and MM5 data. Such a sea breeze depth corresponds to a typical shallow sea breeze type which has been measured and modeled (partially with the MM5) by many authors for several subtropical regions of the world including Asia, Australia and the Mediterranean (Reible et al., 1993; Ding et al., 2004; Lemonsu et al., 2006; Srinivas et al., 2007).
Finkele (1998) and Gilliam et al. (2004) studied the inland propagation of sea breezes due to different geostrophic background flows using varies numerical models. Both authors illustrate that a light geostrophic offshore flow of 1–3 m/s increases the inland propagation, whereas a stronger off-shore flow leads to a decrease in the penetration range. For off-shore geostrophic wind speeds greater than 6–8 m/s the sea breeze develops but stays offshore until it disappears. In general the maximum intensity of the sea breeze as measured by vertical velocity turns out to have a maximum intensity just after the time of the solar radiation maximum.
According to the ECMWF and MM5 data of this case study, the mean mesoscale offshore flow covers a range of 2 to 8 m/s depending on time and the local orography, therefore one expects a time and orography dependent inland propagation for our sea breeze. The presented results proof that the MM5 shows a feasible performance for the regions north-east and south-east of Dakar with small scale characteristics that are supported by the authors mentioned above. Those regions with the strongest mesoscale flow up to 8 m/s (located about 80 km north of Dakar) show no inland penetration, whereas the sea breeze pentetrates the inland up to 20 km from the coast line in regions with lower mesoscale wind speeds. Furthermore the modeled mean vertical velocities up to 20 cm/s also show agreement to the named authors. Beyond that the maximum vertical velocities are observed at 15.30 UTC (that is about 2 hours after the maximum of solar radiation)
In contrast to MM5 data, the ECMWF analysis data does not feature any inland propagation apart from the Dakar peninsula, which can be attributed to the worse resolution. The fact that the Dakar peninsula has an exceptional position showing the earliest initiation of convection and a fundamentally more diffused sea breeze structure than the continental regions can be attributed to the development of the two sea breezes north and south of the peninsula and to a smaller extent to a heat island effect. Childs and Raman (2005) and Freitas et al. (2007) demonstrated that heat islands enhance the propagation speed of sea breezes, what should also be valid for Dakar. Furthermore Gilliam et al. (2004) studied curvature effects of the coast line in terms of sea breeze strengths. They showed that areas of stronger upward motion are related to cape areas, whereas weaker vertical motion is observable over bays. Rudimentarily this observation is represented for 13 UTC referring to the bay east of central Dakar, but the hilly landscape of the peninsula could also be a reason for this observation. In summary the modeled strength, structure and extension of the sea breeze is quite plausible referring to former studies of sea breezes in other locations.

Table 5.3 shows a comparison of the MM5 model output with Falcon in-situ data. The parameters relative humidity, wind direction, boundary layer height and location of max pollution/humidity bubbles were chosen, because they characterize the appearance of the sea breeze.

Table 5.3: Comparison of meteorological data: MM5 versus Falcon in-situ data.

Parameter	MM5	Falcon In-situ data
Rel. humidity sequence 29a_3	36–42 %	14–22 %
Rel. humidity DKR*, 15.45 UTC	50 %	33%
Wind direction sequence 29a_3	90°	85°
Wind direction DKR*, surface	355°	350°
Stable boundary layer height	0–250 m a.s.l.	0–300 m a.s.l.
Location of max pollution/humidity bubbles	western Dakar peninsula	southern Dakar peninsula

* DKR = Dakar airport, located in the north-western part of the Dakar peninsula.

The maximum relative humidity over Dakar in 640 m a.s.l. measured by the Falcon aircraft is less than 25 %, whereas the MM5 simulated values up to 42 % i.e. the MM5 seems to overestimate low level convection. Associated with the overestimation of the sea breeze strength, the modeled surface-near relative humidity at DKR exceeds the measured one. Wind directions and boundary layer height modeled by the MM5 are in good agreement to the measurement results. Furthermore the highest modeled relative humidities in 640 m a.s.l. can be found over the north-western part of the Dakar peninsular. The bubbles of convection are responsible for upward transport of the urban pollution and can not directly be compared to the in-situ measurements of the maximum pollution, because besides the uptake of surface-near air also the strength of pollution, which shows large variations at ground level due to small scale land use, has to be considered. Nevertheless, the MM5 model results show the maximum relative humidities in 640 m a.s.l. less than 10 km away from the maximum pollution detected by in-situ measurments.
The overestimation of sea breeze strength in turn is a feature of the Gayno-Seaman PBL parametrization scheme that has recently been studied by Srinivas et al. (2007) and Miao et al. (2009). Both authors present comprehensive comparisons of several parametrization schemes which demonstrate that GS shows a good overall performance but overestimates the vertical wind speed (partially by a factor of 2–3). Thus it is not astonishing that our MM5 results show deviations from the in-situ data referring to the strength and exact location of convection, but nevertheless the basic circulation pattern is very plausible.

5.1.3 Air mass characterization

Air mass characterizations are based on trajectory calculation and form an important part of this thesis. Therefore they require special evaluation. In this study two different datasets are available to calculate trajectories (forward and backward): the ECMWF analysis data with a horizontal resolution of $0.225° \times 0.225°$ and the results from the MM5 modeling providing a horizontal resolution of $0.03° \times 0.03°$. For long range transport calculations of air masses dominated by the mesoscale flow LAGRANTO trajectories provide more suitable data, because global data is available instead of the limited domains of the MM5. Moreover trajectory calculations by the Lagranto trajectory tool are less time-consuming than trajectory calculation achieved by the MM5. However, Stohl et al. (1998) showed that LAGRANTO trajectories based on the mentioned ECMWF data have position errors in the range of 20 % of the transport

distance just to get an idea of the general inaccuracy of such trajectories.

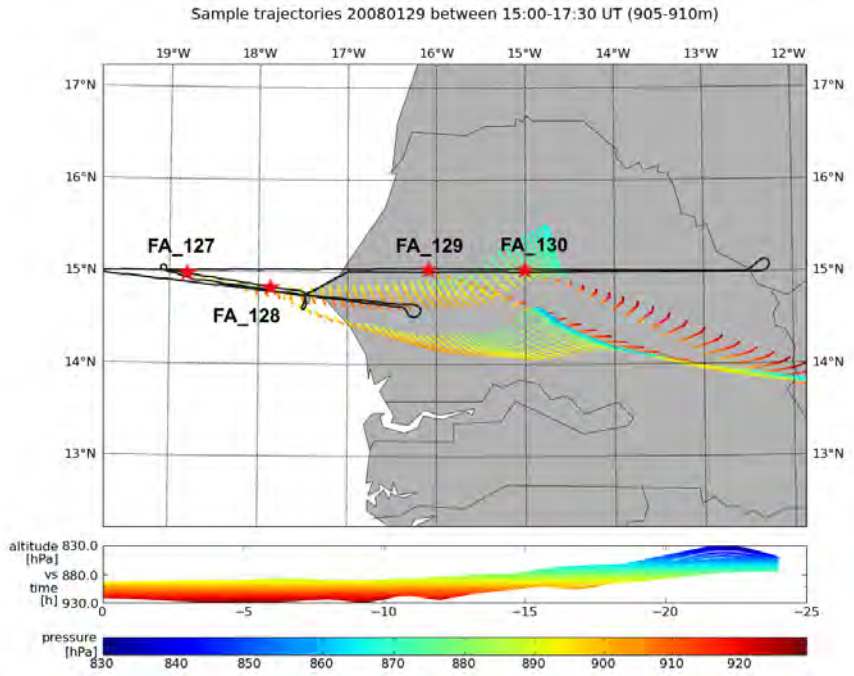

Figure 5.1: LAGRANTO back trajectories for impactor samples collected upstream and downstream Dakar. Stars indicate the sampling locations, black lines demonstrate the flight path of the Falcon aircraft.

The backward trajectories of the four impactor samples near Dakar (presented in Chapter 4.4.3) provide a concrete example for the general complexity of problems referring to trajectory inaccuracy. The results from LAGRANTO trajectory calculations are shown in Fig. 5.1. It is a composition plot of the Falcon flight track (black line) and trajectories starting from the positions where the four impactor samples (marked by red stars and numbered FA_127 to FA_130) were taken. Each calculation time step of 30 min is represented by a single dot in the plot. Figure 5.1 shows that the trajectories of FA_127 directly cross the Dakar peninsula, whereas trajectories of impactor sample FA_128 miss the peninsula due to southerly paths. Furthermore the LAGRANTO trajectories never touch the ground. In contrast the MM5 trajectories behave completely oppositional.
Figure 5.2 shows that the MM5 trajectories for FA_127 cross the coastline far north of Dakar, whereas those of FA_128 match the Dakar area. Moreover the trajectory raw data show that those trajectories, which cross the Dakar peninsula, reach low levels corresponding to a pressure of 970 hPa whereas trajectories of FA_127 never reach pressures higher than 910 hPa. Of course trajectories have to cross polluted areas near surface to be loaded with anthropogenic emissions, therefore the MM5 supports the results from the PSAP data analysis scheme. Even if the LAGRANTO trajectories support the chemical analysis results, they do not evidence the statement that the soot dominated sample FA_127 represents aerosol from the Dakar plume because those trajectories come from heights over Dakar that lie a few hundred meters above the plume. In contrast, the MM5 results argue for the PSAP data analysis and also the volatility as well as size-distribution analyses (see also Fig. 4.7) claim for the accuracy

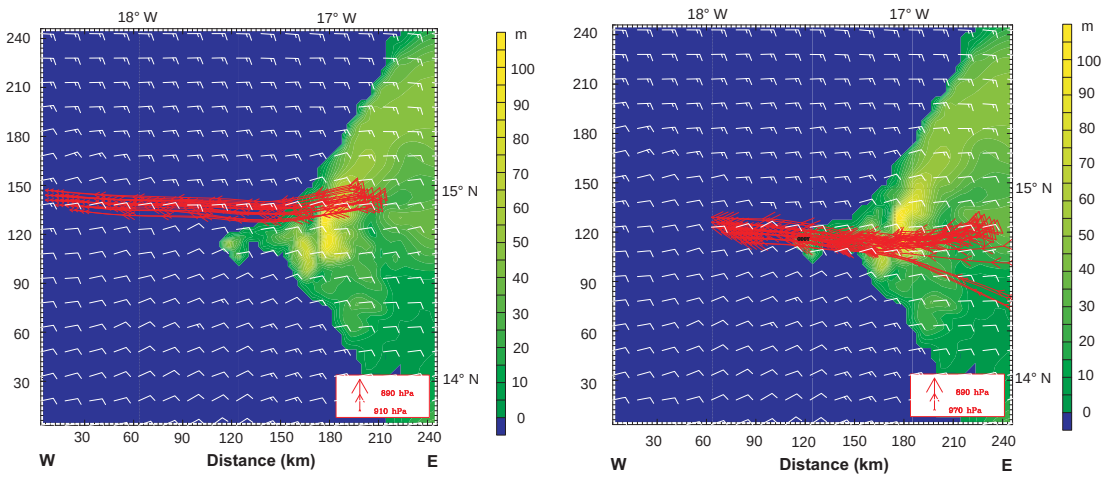

Figure 5.2: MM5 back trajectories for impactor samples FA_127 (left) and FA_128 (right). Starting times of trajectories (17.15 UTC) are equivalent to impactor sampling times.

of the PSAP data. However, it is impossible to clarify the differences between PSAP data and impactor samples finally. Perhaps sample FA_127 and FA_128 got mixed up during transport or analysis or the impactors were contaminated otherwise, but this is just an unprovable guess.

5.1.4 Further development of the plume

Based on the detected aerosol plume over Dakar at 29 January, 18 UTC, in about 400 to 700 m a.s.l. forward trajectories can be calculated to discuss further transport and dispersion of the plume. In this case the use of the MM5 trajectories is neither necessary nor appropriate, because since an air parcel has undergone the sea breeze circulation and passed Dakar, the mesoscale flow dominates and small scale processes become irrelevant. Therefore the use of LAGRANTO trajectories instead of time-consuming MM5 trajectories is sufficient to discuss further development of the plume.
Forward trajectories for a starting level of 600 m show a general northwesterly transport of the plume air masses during the following three days (see Fig. 5.3). Significantly dispersion and considerable ascend is observable for the bulk of the trajectories.
Thus the Dakar plume can be expected to disperse quickly with time. Due to the hardly distinctive change of optical properties in the outer parts of the plume even some km away from the source, the plume will very likely not be detectable by common in-situ or remote sensing measurements after 48 hours.

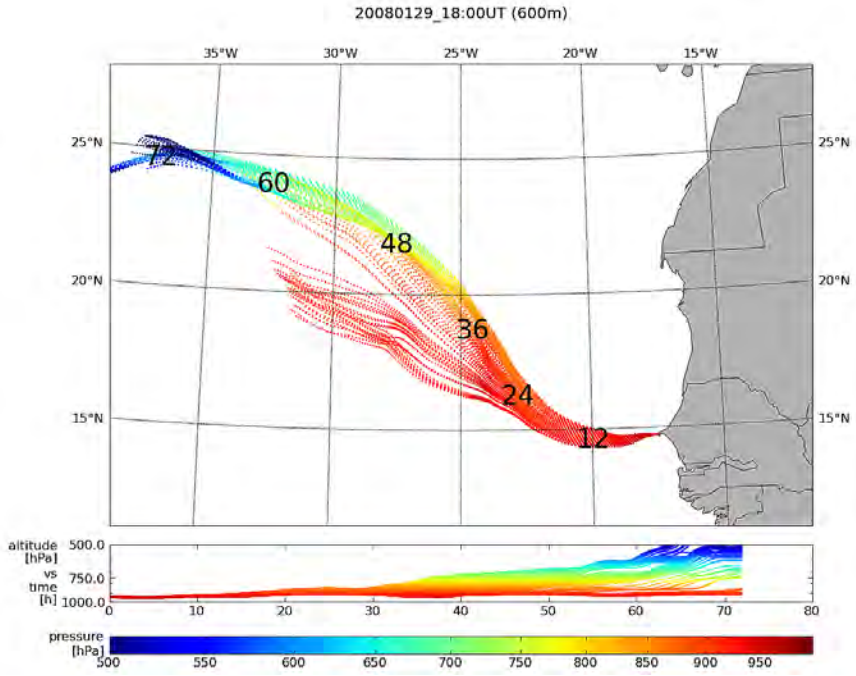

Figure 5.3: Forward trajectories starting from Dakar (14.7°N, -17.5°W) on 29 January 2008 at 18 UTC for a starting level of 600 m a.s.l.

5.2 Aerosol Properties

In order to discuss the changes in optical properties of dust by mixing with anthropogenic emissions from the urban area of Dakar, the results from aerosol measured upstream the source region in pure mineral dust served as a reference state. The differences between average values found in pure mineral dust and values determined from samples taken over the urban area of Dakar showed a clear signature of the Dakar plume in both, HSRL, and in-situ data. But the significance of change referring to most parameters seems to be limited to the near-source region straight over the Dakar peninsula.

HSRL data

The HSRL extinction data at 532 nm indicate an increase of the AOD from 0.28 to 0.31 over land and over sea off Dakar to 0.35 over the area of Dakar. This increase by 16 % is statistically significant. Comparing the increase in extinction to the increase in absorption clearly demonstrates that mineral dust completely dominates the optical properties of the aerosol even over a strong source region for anthropogenic pollution as the city of Dakar. This is one of the key conclusions of this study.

Volatility and size distributions

The presented volatility analyses show a generally higher fraction of volatile particles within the plume and also upstream Dakar, where the slight increase in volatility can be accounted to farming activities. The observed variations of volatility account for the

assumption that Dakar's urban pollution plume contains black carbon dominated areas (featuring low volatility) as well as sulphate/nitrate and organic carbon dominated areas (featuring high volatility). Recalling the results from the MM5 modeling which show great small scale differences for trajectories, the variations of volatility within the plume can be attributed to different pollution emittants (oil refineries, traffic, framing and others). Additionally the aerosol affected by urban pollution was externally mixed. Particle number concentrations were enhanced by more than one order of magnitude in the size range $< 0.3\,\mu$m.

Absorption, single scattering albedo and ångström coefficient

Due to the existence of black carbon aerosol, the plume aerosol light absorption at 660 nm was enhanced by a factor of ten compared to mineral dust upstream of the source. In the green where mineral dust is stronger absorbing than in the red, absorption was still enhanced by a factor of five. Absorption at 530 nm and 660 nm are those parameters which show a real domination of anthropogenic aerosol, whereas all other parameters are modified by mixing, but mineral dust can still be accounted to be the dominating species. The contribution of sub-μm sized particles to aerosol absorption at 530 nm (40–50 % in pure mineral dust and 65–85 % in the plume center) showes similar trends as data reported by Quinn and co-authors (2004) for the outflow from China and Korea towards Japan. They found a fraction of 88–93 % in polluted air masses and a fraction of 73–77 % in mineral dust.
Referring to single scattering albedo values of ω_0 of 0.95–0.99 (at 530 nm) were observed for pure mineral dust and dust + anthropogenic pollution sequences. Only the one sequence related to the highest pollution presents a single scattering albedo value of $\omega_0 = 0.907 \pm 0.027$. Both, values for mineral dust dominated sequences as well as the value for the plume core agrees very well with data reported from literature, see Quinn et al. (2004) and Todd et al. (2007). Bergstrom et al. (2004) presented estimations that addition of urban pollution black carbon fraction leads to a decrease in ω_0-values about 0.06–0.09. Thus, the limitation of the mentioned decrease in ω_0-values to the plume center forces the conclusion that the observed mixing processes are of the that strength described by Bergstrom et al. (2004), but the Dakar plume is only a local phenomenon. The conclusion that mineral dust still dominates the absorption spectral dependence can be drawn, because in contrast to the Dakar plume, $\mathring{a}_{ap}$ - values close to unity were frequently observed in Casablanca during SAMUM-I although mineral dust was present as well in the urban atmosphere (Petzold et al., 2009). Absorption coefficients at 530 nm are of similar magnitude in Dakar $(12.0 \pm 2.6)\,\mathrm{Mm}^{-1}$ and in Casablanca, Morocco $(12.8 \pm 2.2)\,\mathrm{Mm}^{-1}$ while the respective $\mathring{a}_{ap}$ values are 2.3–4.5 (Dakar) and 1.28 ± 0.28 (Casablanca, 18 samples). Likewise, even over the Dakar source region the wavelength dependence of aerosol absorption is dominated by the mineral dust fraction. This observation is completely different to measurements performed during SAMUM-I in the dust-loaded atmosphere of the city of Casablanca (Petzold et al., 2009). There absorption Ångström exponent values close to unity were found. Those values in turn are characteristic for an aerosol dominated by small-sized black carbon agglomerates.

Refractive index

The real parts of the refractive index calculated by the PSAP analysis scheme range from 1.546 to 1.552 for a wavelength of 530 nm, showing an increase with increasing

anthropogenic fraction. These values show good agreement to results from SAMUM-I, see Petzold et al. (2009); Wagner et al. (2009), which provide real parts between 1.53 and 1.56 for dust dominated aerosol. Moreover the imaginary part of the refractive index for little or non anthropogenic influenced aerosol varies between $k = 0.001$–0.002 for 530 nm and can also be compared to some results of SAMUM-I, even if SAMUM-I provides values of $k = 0.0042$ for 550 nm, too. Over the source area of the Dakar plume the imaginary part of the refractive index is increased by a factor of six, but remains still within the natural variability of mineral dust from various sources. Petzold et al. (2009) showed that the PSAP data analysis scheme used for SAMUM-I tended to underestimate k in comparison to results from single particle analysis, therefore our results of k will presumably tend to underestimate the imaginary part, too.

Chemical composition

Black carbon agglomerates (soot) were observed only in the sub-500 nm fraction by electron microscopy. This indicates external mixture of mineral dust and black carbon particles. Back trajectories of samples show that even after 6 h of transport black carbon agglomerates are still externally mixed. Internal mixtures of black carbon agglomerates with mineral dust were not detected. Black carbon aerosol was only observed to mix with secondary sulphate. The coarse particles ($d_p > 0.5\mu$m) were dominated by silicates. The prevalence of externally mixed carbonaceous agglomerates in the dry atmosphere of Western Africa is also reported for biomass burning particles (Formenti et al., 2008; Rajot et al., 2008; Hand et al., 2010) from the AMMA studies. Similar results have been presented by Song et al. (2005) for mixing of Asian dust and urban pollution.

The calculated soot mass concentrations vary extremely according to the fine structure of the plume. BC mass concentrations near to the plume center (up to 1.3 μg/m^3) are comparable to observations from rural East Asia areas over land and offshore, see Parungo et al. (1994), but they are one order of magnitude smaller than mass concentration from extremely polluted source-near areas presented by Andreae et al. (2008). In contrast the peripheral areas of the plume and those regions 10 to 30 km west of Dakar provide mass concentrations ranging from 0.03–0.5 μg/m^3. Referring to Parungo et al. (1994), half-life times of BC were found to be less then 24 hours for Asian urban pollution. Taking into account further dispersion, the large-scale impact of the Dakar plume can be accounted to be very small to negligible.

Chou et al. (2008) have shown that biomass burning aerosols in dust layers are essentially found between 0.1 and 0.6 μm diameter, whereas mineral dust particles are seldom found below diameters of 0.4 μm. With respect to mixing with mineral dust, black carbon from anthropogenic sources and biomass burning particles seem to behave similarly. During the strong dust event of 25 - 30 January 2008, the black carbon emissions from the city of Dakar contributed about 1 % of mass to the total plume aerosol. These soot value shows good agreement to results from Tenerife, see Kandler et al. (2007), whereas the observed fractions of hematite (≈ 0.2 % Vol.) are considerably smaller. However, the impact of the amount of black carbon on the radiative properties of mineral dust seems to be of local importance only, because the high soot contents only occure within the highly polluted areas of the plume directly over the Dakar peninsula.

PSAP data analysis scheme

Finally the performance of the PSAP data analysis scheme is evaluated. As Ångström-coefficients and single scattering albedo are in accordance with results from literature, the general analysis scheme succeeds. The simple three-component model based on the components quartz, soot and hematite creates reasonable real and imaginary parts. In contrast to the other parameters, the refractive index and the effective chemical composition have non-negligible systematic inaccuracies because of the missing input of a measured chemical composition. The limitation to the three PSAP wavelengths is reflected in all of the microphysical and optical results and is simultaneously a limitation of this study. Furthermore the accuracy of refractive indices (calculated by the PSAP data analysis scheme) demonstrates the borders of this method due to the independence from an a-priori assumption of the real part of the refractive index. The effective chemical composition may not be interpreted as a real chemical composition, but nevertheless it provides an accurate method of investigation for this data set. The discussed results for the iron oxide and soot fractions provide a coherent data set with a consistent detection of the plume in terms of soot and plausible soot mass concentrations.

Chapter 6

Summary and Future Work

Summary

In this SAMUM-II case study the mixing of Dakar's anthropogenic plume with mineral dust aerosol was investigated. In order to achieve a reliable basis for the interpretation of the airborne remote sensing and in-situ results, a detailed characterization of the plume structure and an extensive analysis of the meteorological conditions, which determine the plume structure, turned out to be necessary. Based on these analyses the changes in microphysical, optical and chemical mineral dust properties due to mixing with Dakar's anthropogenic emission were studied. The basic results are presented in the following:

- During the Saharan dust outbreak between 28 and 30 January 2008, Dakar's urban pollution plume was determined by the superposition of a westward mesoscale flow and a local sea breeze circulation. Simulations of a mesoscale numerical weather prediction model (MM5) as well as in-situ data demonstrate the importance of the sea breeze, because the associated convective areas are responsible for the vertical transport of surface-near emissions. The HSRL data show that the strongest pollution can be found between 400 to 700 m straight above the Dakar peninsula, whereas dispersion dominates regions west of Dakar over the Atlantic ocean. The results from MM5 modeling show good agreement to in-situ measurements referring to the observation of convective regions, horizontal and vertical wind patterns and the boundary layer height. The meteorological analysis serves as essential data set for the classification and interpretation of the HSRL and in-situ results.

- The optical and microphysical parameters of the mineral dust turned out to be influenced by mixing with anthropogenic pollution to different extents. Aerosol optical depth and extinction are significantly enhanced, but the plume aerosol can still be declared dust-dominated. Furthermore the dust-dominated and rarely polluted plume regions showed single scattering albedos ω_0 of 0.95 to 0.99 (at 530 nm), whereas a minimum of $\omega_{0,min}$ of 0.907 ± 0.027 was observed for the plume center. The absorption Ångström coefficients within the plume range between 2.3 and 4.5. This observation is completely different to measurements performed during SAMUM-I (in 2006, near Casablanca) where values of 1.28 ± 0.28 were measured. In contrast values for absorption at 530 nm ($12.0 \pm 2.6\,\mathrm{Mm}^{-1}$) are quite similar to those measured near Casablanca and significant absorption in

the red is only observable within the plume. Single particle chemical analysis and size distributions show that mineral dust and soot aerosol were solely externally mixed. Soot was detectable only for sub-500 nm particles and maximum mass concentrations of $\approx 1\,\mu g/cm^3$ were found. The change in refractive index due to mixing with urban pollution (up to a factor of six at 530 nm) is significant according to the unpolluted reference dust, but it is still within the natural variations of mineral dust.

In summary significant changes in optical and microphysical properties of mineral dust due to mixing with Dakar's anthropogenic pollution plume were found to be locally confined.

Future work

There are several ideas for further investigation of this data set of SAMUM-II, but the most important aspect of investigation (that is completely omitted in this thesis) is the implementation of the results of this study into a radiative transfer model. Presumably the change in radiative forcing with respect to mixing of anthropogenic pollution into mineral dust aerosol will be insignificant due to the observed small changes in the refractive index, but this assumption has to be proved. Furthermore the results from this case study can also serve as input for simulations in connection with the "EarthCare" project (see the ICAROHS project supported by ESA, `http://wfaa-dat.esrin.esa.int/stse/projects/summaryp101.asp`). Besides, modeling of the further development of the Dakar plume, which was only touched peripherally in this study, could be realized by the use of Flexpart; see Stohl et al. (1998) and references therein.

Bibliography

Ackerman, T. P. and Toon, O. B. (1981). Absorption of visible radiation in atmosphere containing mixtures of absorbing and nonabsorbing particles. *Applied Optics*, 20:3661–3668.

Addlesee, A. (1980). Anisokinetic sampling of aerosols at a slot intake. *Journal of Aerosol Science*, 11:483–493.

An, W. J., Pathak, R. K., Lee, B.-H., and Pandis, S. N. (2007). Aerosol volatility measurement using an improved thermodenuder: Application to secondary organic aerosol. *Journal of Aerosol Science*, 38:305–314.

Andreae, M. O., Schmid, O., Yang, H., Chand, D., Yu, J. Z., and co authors (2008). Optical properties and chemical composition of the atmospheric aerosol in urban Guangzhou, China. *Atmospheric Environment*, 42:6335–5350.

Ångström, A. (1964). The parameters of atmospheric turbidity. *Tellus*, 16:64–75.

Ansmann, A., Petzold, A., Kandler, K., Tegen, I., Wendisch, M., and co authors (2011). Saharan Mineral Dust Experiments SAMUM-1 and SAMUM-2: What have we learned. *Tellus*, 63.

Arakawa, A. and Messinger, F. (1976). Numerical methods used in atmospheric models. Technical report, GARP technical report 17, WMO/ICSU.

Bergstrom, R. W., Pilewskie, P., Pommier, J., Rabbette, M., Russell, P., and co authors (2004). Spectral absorption of solar radiation by aerosols during ACE-Asia. *Journal of Geophysical Research - Atmospheres*, 109:D19S15, doi:10.1029/2003JD004467.

Bergstrom, R. W., Pilewskie, P., Russell, P. B., Redemann, J., Bond, T. C., and co authors (2007). Spectral absorption properties of atmospheric aerosols. *Atmospheric Chemistry and Physics Discussion*, 7:10669–10686.

Bohren, C. F. and Huffman, D. R. (1983). *Absorption and Scattering of Light by Small Particles*. John Wiley & Sons, Inc.

Bond, T. C., Anderson, T. L., and Campbell, D. (1999). Calibration and intercomparison of filter-based measurements of visible light absorption by aerosols. *Aerosol Science and Technology*, 30:582–600.

Bond, T. C. and Bergstrom, R. W. (2006). Light absorption by carbounaceous particles: An investigative review. *Aerosol Science and Technology*, 39:1–41.

Bouchlaghem, K., Mansour, F. B., and Elouragini, S. (2007). Impact of a sea breeze event on air pollution at the Eastern Tunisian Coast. *Atmospheric Research*, 86:162–172.

Brock, C. A., Schröder, F.and Kärcher, B., Petzold, A., Busen, R., and Fiebig, M. (2000). Ultrafine particle size distributions measured in aircraft exhaust plumes. *Journal of Geophysical Research - Atmospheres*, 105:26,555–26,567.

Childs, P. P. and Raman, S. (2005). Observations and numerical simulations of urban heat island and sea breeze circulations over New York City. *Pure and Applied Geophysics*, 162:1955–1980.

Chou, C., Formenti, P., Maille, M., Ausset, P., Helas, G., and co authors (2008). Size distribution, shape, and composition of mineral dust aerosols collected during the African Monsoon Multidisciplinary Analysis Special Observation Period 0: Dust and biomass-burning experiment field campaign in Niger, January 2006. *Journal of Geophysical Research - Atmospheres*, 113:doi:10.1029/2008JD009897.

Chýlek, P., Srivastava, V., Pinnick, R. G., and Wang, R. T. (1988). Scattering of electromagnetic waves by composite spherical particles: experiment and effective medium approximations. *Applied Optics*, 27:2396–2404.

Ciddor, E. C. (1996). Refractive index of air: new equations for the visible and near infrared. *Applied Optics*, 35, No. 9:1566–1573.

Clarke, A. D. (1991). A thermo-optic technique for in situ analysis of size-resolved aerosol physicochemistry. *Atmospheric Environment*, 25:635–644.

Clarke, A. D., Shinozuka, Y., Napustin, V. N., Howell, S., Huebert, B., and co authors (2004). Size distributions and mixtures of dust and black carbon aerosol in Asian outflow: Physiochemistry and optical properties. *Journal of Geophysical Research - Atmospheres*, 109:D15S09, doi:10.1029/2003JD004378.

Curtius, J., Weigel, R., Vössing, H.-J., Wernli, H., Werner, A., and co authors (2005). Observations of meteoritic material and implications for aerosol nucleation in the winter Arctic lower stratosphere derived from in situ particle measurements. *Atmospheric Chemistry and Physics Discussions*, 5:5039–5080.

Ding, A., Wang, T., Zhao, M., Wang, T., and Li, Z. (2004). Simulation of sea-land breezes and a discussion of their implications on the transport of air pollution during a multi-day ozone episode in the Pearl River Delta of China. *Atmospheric Environment*, 38:6737–6750.

Droplet Measurement Technologies, I. (2009). *Passive Cavity Aerosol Spectrometer Probe (PCASP-100X)*. 2545 Central Avenue, Boulder, CO 80301 USA.

Dubovik, O., Holben, B. N., Lapyonok, T., Sinyuk, A., Mishchenko, M. I., and co authors (2002). Non-spherical aerosol retrieval methods employing light scattering by spheroids. *Geophysical Research Letters*, 29:10.1029/2001GL014506.

Dudhia, J., Gill, D., Maning, K., Wang, W., and Bruyere, C. (2005). *PSU/NCAR Mesoscale Modeling System Tutorial ClassNotes and Users' Guide (MM5 Modeling System Version 3)*.

Esselborn, M. (2008). *Lidar–Messung der Extinktion des atmosphärischen Aerosols am Beispiel der Feldstudie SAMUM–1.* PhD thesis, University of Munich.

Esselborn, M., Wirth, M., Fix, A., Tesche, M., and Ehret, G. (2008). Airborne high spectral resolution lidar for measuring aerosol extinction and backscatter coefficients. *Applied Optics*, 47:346–358.

Esselborn, M., Wirth, M., Fix, A., Weizierl, B., Rasp, K., and co authors (2009). Spatial distribution and optical properties of Saharan dust observed by airborne high spectral resolution lidar during SAMUM 2006. *Tellus*, 61B:131–143.

Fan, S.-M., Horowitz, L. W., II, H. L., and Moxim, W. J. (2004). Impact of air pollution on wet deposition of mineral dust aerosols. *Geophysical Research Letters*, 31:doi:10.1029/2003GL018501.

Faulhaber, A. E., Thomas, B. M., Jimenez, J. L., Jayne, J. T., Worsnop, D. R., and Ziemann, P. J. (2009). Characterization of a thermodenuder-particle beam mass spectrometer system for the study of organic aerosol volatility and composition. *Atmospheric Measurement Techniques*, 2:15–31.

Feldpausch, P., Fiebig, M., Fritzsche, L., and Petzold, A. (2006). Measurement of ultrafine aerosol size distributions by a combination of diffusion screen separators and condensation particle counters. *Journal of Aerosol Science*, 37:577–597.

Feng, J. (2008). A size-resolved model and a four-mode parameterization of dry deposition of atmospheric aerosols. *Journal of Geophysical Research*, 113:doi:10.1029/2007JD009004.

Fiebig, M. (2001). *Das troposphärische Aerosol in mittleren Breiten - Mikrophysik, Optik und Klimaantrieb am Beispiel der Feldstudie LACE 98.* PhD thesis, Ludwig-Maximilians-Universtität München.

Finkele, K. (1998). Inland and offshore propagation speeds of a sea breeze from numerical simulatios and measurements. *Boundary Layer Meteorology*, 87:307–329.

Formenti, P., Elbert, W., Meaenhaut, W., Haywood, J., and Andreae, M. O. (2003). Chemical composition of mineral dust aerosol during the Saharan Dust Experiment (SHADE) airborne campaign in the Cape Verde region, September 2000. *Journal of Geophysical Research*, 108:doi:10.1029/2002JD002648.

Formenti, P., Rajot, J. L., Desboeufs, K., Caquineau, S., Chevaillier, S., and co authors (2008). Regional variability of the composition of mineral dust from western Africa: Results from the AMMA SOP0/DABEX and DODO field campaigns. *Journal of Geophysical Research - Atmospheres*, 113:D00C13, doi:10.1029/2008JD009903.

Freitas, E. D., Rozoff, C. M., Cotton, W. R., and Dias, P. L. S. (2007). Interactions of an urban heat island and sea-breeze circulations during winter over the metropolitan area of São Paulo, Brazil. *Boundary Layer Meteorology*, 122:43–65.

Fuller, K. A., Malm, W. C., and Kreideweis, S. M. (1999). Effects of mixing on extinction by carbonaceous particles. *Journal of Geophysical Research - Atmospheres*, 104:15941–15954.

Fung, I. Y., Meyn, S. K., Tegen, I., Doney, S. C., John, J. G., and co authors (2000). Iron supply and demand in the upper ocean. *Global Biogeochemical Cycles*, 14, No.1:281–295.

Gaza, R. S. (1998). Mesoscale meteorology and high ozone in the northeast united states. *Journal of Applied Meteorology*, 37:961–977.

Giechaskiel, B., Wang, X., Gilliland, D., and Drossinos, Y. (2010). The effect of particle chemical composition on the activation probability in n-butanol condensation particle counters. *Journal of Aerosol Science*, 42:20–37.

Giglio, L., Descloitres, J., Christopher, O. J., and Kaufman, Y. J. (2003). An enhanced contextual fire detection algorithm for MODIS. *Remote Sensing of Environment*, 87:273–282.

Gilliam, R. C., Raman, S., and Niyogi, D. N. S. (2004). Observational and numerical study on the influence of large-scale flow direction and coastline shape on sea-breeze evolution. *Boundary Layer Meteorology*, 111:275–300.

Grell, A. G., Dudhia, J., and Stauffner, D. R. (1995). A Description of the Fifth-Generation Penn State/NCAR Mesoscale Model (MM5). Technical report, NCAR.

Griffin, D. W., Garrison, V. H., Herman, J. R., and Shinn, E. A. (2001). African desert dust in the Caribbean atmosphere: Microbiology and public health. *Aerobiologica*, 17:203–213.

Hair, J. W., Hostetler, C. A., Cook, A. L., Harper, D. B., Ferrare, R. A., and co authors (2008). Airborne High Spectral Resolution Lidar for profiling aerosol optical properties. *Applied Optics*, 47:6734–6753.

Hamburger, T. (2010). *Aerosol microphysical properties during anticyclonic flow conditions over Europe*. PhD thesis, University of Munich.

Hamburger, T., McMeeking, G., Minikin, A., Birmili, W., Dall'Osto, M., and co authors (2010). Overview of the synoptic and pollution situation over Europe during the EUCAARI-LONGREX field campaign. *Atmospheric Chemistry and Physics Discussions*, 10:19129–19174.

Hand, V. L., Capes, G., Vaughan, D. J., Formenti, P., Haywood, J. M., and Coe, H. (2010). Evidence of internal mixing of African dust and biomass burning particles by individual particle analysis using electron beam techniques. *Journal of Geophysical Research - Atmospheres*, 115:D13301, doi:10.1029/2009JD012938, 2010.

Haywood, J. and Boucher, O. (2000). Estimates of the direct and indirect radiative forcing due to tropospheric aerosols: a review. *American Geophysical Union*, 38, 4:513–543.

Heintzenberg, J. (2009). The SAMUM-1 experiment over Southern Morocco: overview and introduction. *Tellus*, 61B:2–11.

Hermann, M., Adler, S., Caldow, R., Stratmann, F., and Wiedensohler, A. (2005). Pressure-dependent efficiency of a condensation particle counter operated with FC-43 as working fluid. *Journal of Aerosol Science*, 36:1322–1337.

Hermann, M. and Wiedensohler, A. (2001). Counting efficiency of condensation particle counters at low-pressures with illustrative data from the upper troposphere. *Journal of Aerosol Science*, 32:975–991.

Hess, M., Koepke, P., and Schult, I. (1998). Optical Properties of Aerosols and Clouds: The Software Package OPAC. *Bulletin of the American Meteorological Society*, 79:831–844.

Hinds, W. C. (1999). *Aerosol Technology*. John Wiley & Sons, New York.

Holton, J. R. (2004). *An Introduction to Dynamic Meteorology*. Elsevier Academic Press, London.

Hong, S.-Y. and Pan, H.-L. (1996). Nonlocal boundary layer vertical diffusion in a medium-range forecast model. *Monthly Weather Review*, 124:2322–2339.

Huffman, J. A., Docherty, K., Aiken, A. C., Cubison, M. J., Ulbrich, L. M., and co authors (2009). Chemically-resolved aerosol volatility measurements from two megacity field studies. *Atmospheric Chemistry and Physics*, 9:7161–7182.

IPCC (2007). *Contribution of Working Group I to the Fourth Assessment Report of the Intergovernmental Panel on Climate Change, 2007*. Cambridge University Press, Cambridge, United Kingdom.

Jackson, J. D. (1998). *Classical Electrodynamics*. John Wiley & Sons, New York.

Jacobson, M. Z. (2000). A physically-based treatment of elemental carbon optics: Implications for global direct forcing of aerosols. *Geophysical Research Letters*, 27, No.2:217–220.

Janjić, Z. I. (1990). The step-mountain coordinate: Physical package. *Monthly Weather Review*, 118:1429–1443.

Kahnert, M., Nousiainen, T., and Räisänen, P. (2007). Mie simulations as an error source in mineral aerosol radiative forcing calculations. *Royal Meteorological Society*, 133:299–307.

Kandler, K., Benker, N., Bundke, U., Cuevas, E., Ebert, M., and co authors (2007). Chemical composition and complex refractive index of Saharan mineral dust at Izana, Tenerife (Spain) derived by electron microscopy. *Atmospheric Environment*, 41:8058–8074.

Kandler, K., Schütz, L., Deutscher, C., Ebert, M., Hofmann, H., and co authors (2009). Size distribution, mass concentration, chemical and mineralogical composition and derived optical parameters of the boundary layer aerosol at Tinfou, Morocco, during SAMUM 2006. *Tellus B*, 61:32–50.

Kirchstetter, T. W., Novakov, T., and Hobbs, P. V. (2004). Evidence that the spectral dependence of light absorption by aerosols is affected by organic carbon. *Journal of Geophysical Research - Atmospheres*, 109:D21208, doi:10.1029/2004JD004999.

Klett, J. D. (1981). Stable analytical inversion solution for processing lidar returns. *Applied Optics*, 20:211–220.

Korhonen, P., Kulmala, M., Laaksonen, A., Viisanen, Y., McGraw, R., and co authors (1999). Ternary nucleation of H_2SO_4, NH_3 and H_2O in the atmosphere. *Journal of Geophysical Research - Atmospheres*, 104:26349–26353.

Krueger, B. J., Grassian, V. H., Cowin, J. P., and Laskin, A. (2005). Heterogeneous chemistry of individual mineral dust particles from different dust source regions: the importance of particle mineralogy. *Atmospheric Environment*, 38:6253–6261.

Laakso, L. (2004). Kinetics and dynamics of atmospheric ions, clusters and aerosols. *Report series in aerosol science*, No.70:5–33.

Lafon, S., Sokolik, I. N., Rajot, J. L., Caquineau, S., and Gaudichet, A. (2006). Characterization of iron oxides in mineral dust aerosols: Implications for light absorption. *Journal of Geophysical Research - Atmospheres*, 111:D21207, doi:10.1029/2005JD007016.

Lemonsu, A., Bastin, S., Masson, V., and Drobinski, P. (2006). Vertical structure of the urban boundary layer over Marseille under sea-breeze conditions. *Boundary-Layer Meteorology*, 118:477–501.

Linke, C., Möhler, O., Veres, A., Mohacsi, A., Bozoki, Z., and co authors (2006). Optical properties and mineralogical composition of different Saharan mineral dust samples: a laboratory study. *Atmospheric Chemistry and Physics*, 6:3315–3323.

Liu, Y. and Daum, P. H. (2000). The effect of refractive index on size distributions and light scattering coefficients derived from optical particle counters. *Journal of Aerosol Science*, 31:945–957.

Lohmann, U. and Feichter, J. (2005). Global indirect aerosol effects: a review. *Atmospheric Chemistry and Physics*, 5:717–737.

Markowski, P. and Richardson, Y. (2010). *Mesoscale Meteorology in Midlatitudes*. John Wiley & Sons, Ltd.

McMurry, P. H. (2000). The history of condensation nucleus counters. *Aerosol Science and Technology*, 33:297–322.

Melas, D., Ziomas, I. C., and Zerefos, C. S. (1995). Boundary layer dynamics in an urban coastal environment under sea breeze conditions. *Atmospheric Environment*, 29:3605–3617.

Miao, J.-F., Wyser, K., Chen, D., and Ritchie, H. (2009). Impacts of boundary layer turbulence and land surface process parameterizations on simulated sea breeze characteristics. *Annales Geophysicae*, 27:2303–2320.

Mie, G. (1908). Beiträge zur Optik trüber Medien, speziell kolloidaler Metallösungen. *Annalen der Physik*, 330:377–445.

Miller, S. T. K., Keim, B. D., Talbot, R. W., and Mao, H. (2003). Sea breeze: Structure, forecasting, and impacts. *Reviews of Geophysics*, 41:doi:10.1029/2003RG000124.

Mishchenko, M. I., Hovenier, J. W., and Travis, L. D. (2000). *Light Scattering by Nonspherical Particles*. Academic Press, London.

Mogili, P. K., Yang, K. H., Young, M. A., Kleiber, P. D., and Grassian, V. H. (2007). Environmental aerosol chamber studies of extinction spectra of mineral dust aerosol components: Broadband ir-uv extinction spectra. *Journal of Geophysical Research - Atmospheres*, 112:D21204, doi:10.1029/2007JD008890.

Nho-Kim, E.-Y., Michou, M., and Peuch, V.-H. (2004). Parameterization of size-dependent particle dry deposition velocities for global modeling. *Atmospheric Environment*, 38:1933 – 1942.

Orlanski, I. (1975). A rational subdivision of scales for atmospheric processes. *Bulletin of the American Meteorological Society*, 56:527–530.

Parungo, F., Nagamoto, C., Zhou, M.-Y., Hansen, A. D. A., and Harris, J. (1994). Aeolian transport of aerosol black carbon from China to the ocean. *Atmospheric Environment*, 28:3251–3260.

Petzold, A., Fiebig, M., Flentje, H., Keil, A., Leiterer, U., and co authors (2002). Vertical variability of aerosol properties observed at a continental site during the Lindenberg Aerosol Characterization Experiment (LACE 98). *Geophysical Research Letters - Atmospheres*, 107:doi:10.1029/2001JD001043.

Petzold, A., Rasp, K., Weinzierl, B., Esselborn, M., Hamburger, T., and co authors (2009). Saharan dust absorption and refractive index from aircraft-based observations during SAMUM 2006. *Tellus*, 61 B:118–130.

Pinheiro, A. C. T., Descloitres, J., Privette, J. L., Susskind, J., Iredell, L., and co authors (2007). Near-real time retrievals of land surface temperature within the MODIS Rapid Response System. *Remote Sensing of Environment*, 106:326–336.

Pinnick, R. G. and Auvermann, H. J. (1979). Response characteristics of Knollenberg light-scattering aerosol counters. *Journal of Aerosol Science*, 10:55–74.

Pryor, S. C. and Barthelmie, R. J. (2000). Particle dry deposition to water surfaces: Processes and consequences. *Marine Pollution Bulletin*, 41:220–231.

Quimette, R. J. and Flagan, R. C. (1982). The extinction coefficient of multicomponent aerosols. *Atmospheric Environment*, 16:2405–2419.

Quinn, P. K., Coffman, D. J., Bates, T. S., Welton, E. J., Covert, D. S., and co authors (2004). Aerosol optical properties measured on board the Ronald H. Brown during ACE-Asia as a function of aerosol chemical composition and source region. *Journal of Geophysical Research - Atmospheres*, 109:D19S01, doi:10.1029/2003JD004010.

Raes, F., Van Dingenen, R., Vignati, E., Wilson, J., Putaud, J.-P., and co authors (2000). Formation and cycling of aerosols in the global troposphere. *Atmospheric Environment*, 34:4215–4240.

Rajot, J. L., Formenti, P., Alfaro, S., Desboeufs, K., Chevaillier, S., and co authors (2008). Amma dust experiment: An overview of measurements performed during the dry season special observation period (SOP0) at the Banizoumbou (Niger) supersite. *Journal of Geophysical Research - Atmospheres*, 113:D00C14, doi:10.1029/2008JD009906,.

Rasp, K. (2007). Spektrale Absorption und Brechungsidex von Saharastaub - Ergebnisse der SAMUM-1 Messkampagne. Master's thesis, University of Munich.

Raynor, G. S., Sethuraman, S., and Brown, R. M. (1979). Formation and characteristics of coastal internal boundary layers during onshore flows. *Boundary Layer Meteorology*, 16:487–514.

Reible, D. D., Simpson, J. E., and Linden, P. F. (1993). The sea breeze and gravity-current frontogenesis. *Quarterly Journal of the Royal Meteorological Society*, 119:1–16.

Rodriguez, S., Querol, X., Alastuey, A., Kallos, G., and Kakaliagou, O. (2001). Saharan dust contributions to PM10 and TSP levels on Southern and Eastern Spain. *Atmospheric Environment*, 35:2433–2447.

Rogers, R. R., Hair, J. W., Hostetler, C. A., Ferrare, R. A., Obland, M. D., and co authors (2009). NASA LaRC airborne high spectral resolution lidar aerosol measurements during MILAGRO: observations and validation. *Atmospheric Chemistry and Physics Discussions*, 9:8817–8856.

Rotstayn, L. D. and Penner, J. E. (2001). Indirect aerosol forcing, quasi forcing, and climate response. *Journal of Climate*, 14:2960–2975.

Seifert, M., Tiede, R., Schnaiter, M., Linke, C., Möhler, O., and co authors (2004). Operation and performance of a differential mobility particle analysizer and a TSI 3010 condensation particle counter at stratospheric temperatures and pressures. *Aerosol Science*, 35:981–993.

Seinfeld, J. H. and Pandis, S. N. (1996). *Atmospheric Chemistry and Physics*. John Wiley & Sons, New York.

Shafran, P. C., Seaman, N. L., and Gayno, G. A. (2000). Evaluation of numerical predictions of boundary layer structure during the Lake Michigan Ozone Study. *Journal of Applied Meteorology*, 39:412–426.

Shettle, E. P. and Fenn, R. W. (1979). Models for the aerosols of the lower atmosphere and the effects of humidity variations on their optical properties. Technical report, Air Force Geophysics Laboratory.

Shinn, E. A., Smith, G. W., Prospero, J. M., Betzer, P., Hayes, M. L., and co authors (2000). African dust and the demise of Caribbean coral reefs. *Geophysical Research Letters*, 27, No.19:3029–3032.

Simpson, J. E. (1994). *Sea Breeze and Local Wind*. Cambridge University Press, Cambridge, United Kingdom.

Sokolik, I. N. and Toon, O. B. (1996). Direct radiative forcing by anthropogenic airborne mineral aerosols. *Nature*, 381:681–683.

Sokolik, I. N. and Toon, O. B. (1999). Incorporation of mineralogical composition into models of the radiative properties of mineral aerosol from UV to IR wavelengths. *Journal of Geophysical Research - Atmospheres*, 104:9423–9444.

Song, C. H., Maxwell-Meier, K., Weber, R. J., Kapustin, V., and Clarke, A. (2005). Dust composition and mixing state inferred from airborne composition measurements during ACE-Asia C130 Flight #6. *Atmospheric Environment*, 39:359–369.

Srinivas, C. V., Venkatesan, R., and Singh, A. B. (2007). Sensitivity of mesoscale simulations of land–sea breeze to boundary layer turbulence parameterization. *Atmospheric Environment*, 41:2534–2548.

Stohl, A., Hittenberger, M., and Wotawa, G. (1998). Validation of the lagrangian particle dispersion model FLEXPART against large-scale tracer experiment data. *Atmospheric Environment*, 32:4245–4264.

Su, W., Schuster, G. L., Loeb, N. G., Rogers, R. R., Ferrare, R. A., and co authors (2008). Aerosol and cloud interaction observed from high spectral resolution lidar data. *Journal of Geophysical Research - Atmospheres*, 113:doi:10.1029/2008JD010588.

Tegen, I. and Schepanski, K. (2009). The global distribution of mineral dust. *IOP Conference Series: Earth and Environmental Science*, 7, Number 1:doi:10.1088/1755–1307/7/1/012001.

Thomsen, G. L. (2006). *Numerical Simulations of low-level convergence Lines over north-eastern Australia*. PhD thesis, University of Munich.

Thorpe, A. J., Volkert, H., and Ziemianski, M. J. (2003). The Bjerknes' Theorem - A Historical Perspective. *Bulletin of the American Meteorological Society*, 84:471–480.

Todd, M. C., Washington, R., Martins, J. V., Dubovik, O., Lizcano, G., and co authors (2007). Mineral dust emission from the Bodélé Depression, northern Chad, during BoDEx 2005. *Journal of Geophysical Research - Atmospheres*, 112:D06207, doi:10.1029/2006JD007170.

Troen, I. and Mahrt, L. (1986). A simple model of the atmospheric boundary layer; sensitivity to surface evaporation. *Boundary-Layer Meteorology*, 37:129–148.

Virkkula, A. (2010). Correction of the calibration of the 3-wavelength Particle Soot Absorption Photometer (3λ PSAP). *Aerosol Science and Technology*, 44:706–712.

Virkkula, A., Ahlquist, N. C., Covert, D. S., Arnott, W. P., Sheridan, P. J., and co authors (2005). Modification, calibration and a field test of an instrument for measuring light absorption by particles. *Aerosol Science and Technology*, 39:68–83.

Wagner, F., Bortoli, D., Pereira, S., Costa, M., Silva, A. M., and co authors (2009). Properties of dust aerosol particles transported to portugal from the sahara desert. *Tellus*, 61 B:96–117.

Wandinger, U., Müller, D., Böckmann, C., Althausen, D., Matthias, V., and co authors (2002). Optical and microphysical characterization of biomass-burning and industrial-pollution aerosols from multiwavelength lidar and aircraft measurements. *Journal of Geophysical Research - Atmospheres*, 107:doi:10.1029/2000JD000202.

Weigel, R., Hermann, M., Curtius, J., Voigt, C., Walter, S., and co authors (2008). Experimental characterization of the condensation particle counting system for high altitude aircraft-borne application. *Atmospheric Measurement Techniques Discussions*, 1:321–374.

Weingartner, E., Saathoff, H., Schaiter, M., Streit, N., Bitnar, B., and co authors (2003). Absorption of light by soot particles: determination of the absorption coefficient by means of aethalometers. *Journal of Aerosol Science*, 34:1445–1463.

Weinzierl, B., Petzold, A., Esselborn, M., Wirth, M., Rasp, K., and co authors (2009). Airborne measurements of dust layer properties, particle size distribution and mixing state of saharan dust during SAMUM 2006. *Tellus*, 61B:96–117.

Weitkamp, K. (2005). *Lidar: Range-Resolved Optical Remote Sensing of the Atmosphere*. Springer Science+Business Media Inc.

Wernli, H. and Davies, H. C. (1997). A lagrangian-based analysis of extratropical cyclones. i: The method and some applications. *Quarterly Journal of the Royal Meteorological Society*, 123:467–489.

Wilson, J. C., Hyun, J. H., and Blackshear, E. D. (1983). The function and response of an improved stratospheric condensation nucleus counter. *Journal of Geophysical Research - Oceans*, 88:6781–6785.

Appendix A

MM5 Figures and Tables

Table: Vertical levels

In chapter 3.2.3 a description of the model set-up used for the MM5-simulations of this case study was given. Additionally to the parameters presented in that chapter, the exact adjustment of the vertical layers is necessary to reconstruct our results. The used σ-levels can be converted into pressure-levels (see Equation 2.55) and these in turn can be converted into heights in meters a.s.l. by using:

$$p\left(h\right) = p_s \left(1 - \frac{\Gamma h}{T_s}\right)^{\frac{Mg}{R\Gamma}} \tag{A.1}$$

where $\Gamma = 5\,\mathrm{K\,km^{-1}}$ is the assumed lapse rate, $M = 0.02896\,\mathrm{kg\,mol^{-1}}$ is the mean molar mass of the atmosphere, $R = 8.314\,\mathrm{J\,K^{-1}\,mol^{-1}}$, g is the acceleration due to gravity and $T_s = 275\,\mathrm{K}$ describes the surface temperature. Table A.1 provides an overview of the vertical levels in terms of the parameters σ, p and z.

Table A.1: Vertical Levels of the MM5 in terms of *sigma*-, p- and z-coordinates.

σ-level	pressure-level (mb)	height above mean sea-level (m)
0.000	100.0	15731.9
0.050	145.0	13537.9
0.100	190.0	11865.2
0.150	235.0	10502.5
0.200	280.0	9347.0
0.250	325.0	8340.5
0.300	370.0	7446.7
0.350	415.0	6641.3
0.400	460.0	5907.4
0.450	505.0	5234.3
0.500	550.0	4606.8
0.550	595.0	4023.6
0.600	640.0	3476.9
0.650	685.0	2962.0
0.700	730.0	2475.3
0.750	775.0	2013.5
0.800	820.0	1574.1
0.850	865.0	1154.8
0.890	901.0	832.6
0.930	937.0	521.2
0.960	964.0	294.9
0.980	982.0	146.0
0.990	991.0	72.7
1.000	1000.0	0.0

Vertical velocity at $\sigma = 0.985$

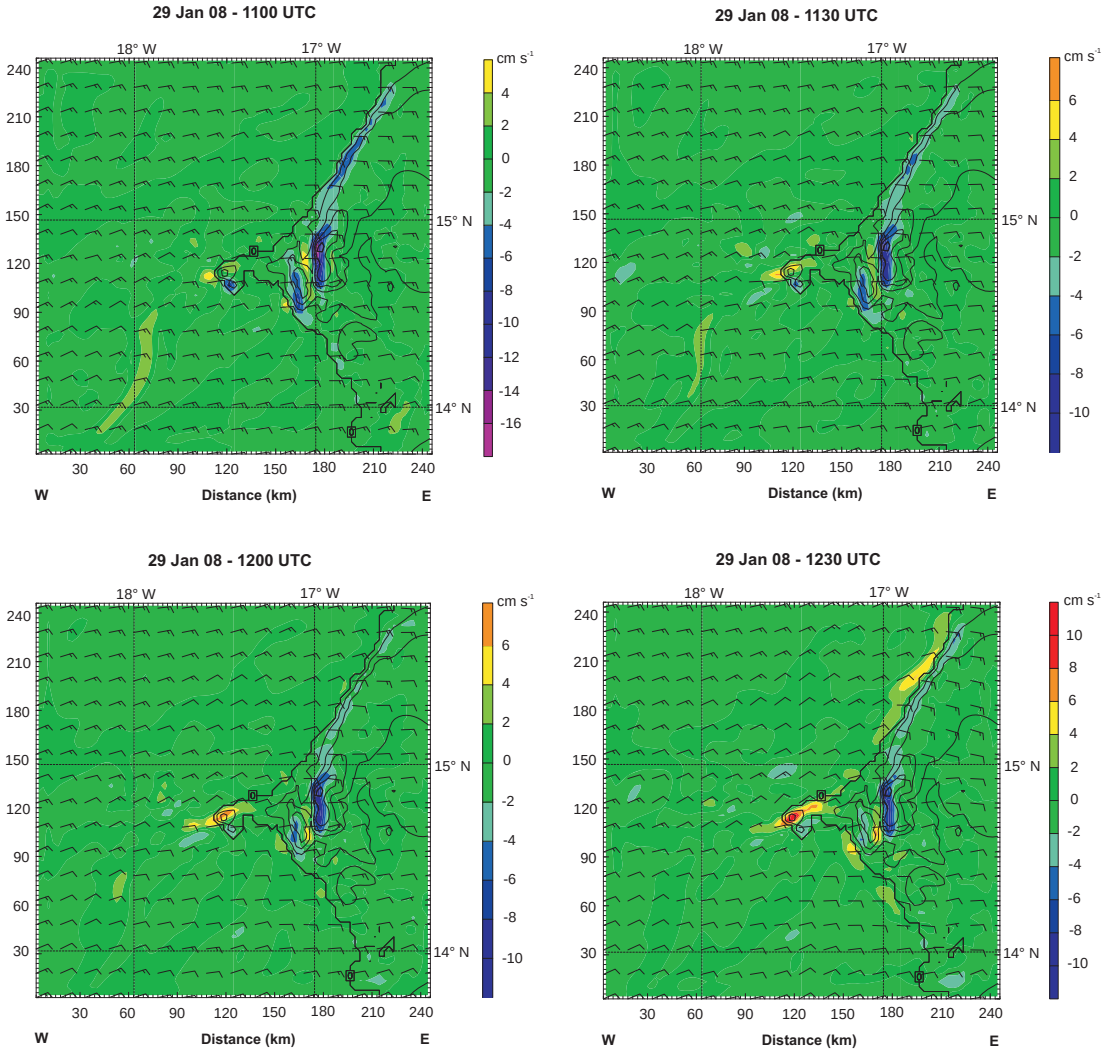

Figure A.1: MM5 vertical velocity (contours) and horizontal wind (black vanes) at $\sigma = 0.985$ for 29 January 2008, 11.00–12.30 UTC; black lines show orography in intervals of 20 m.

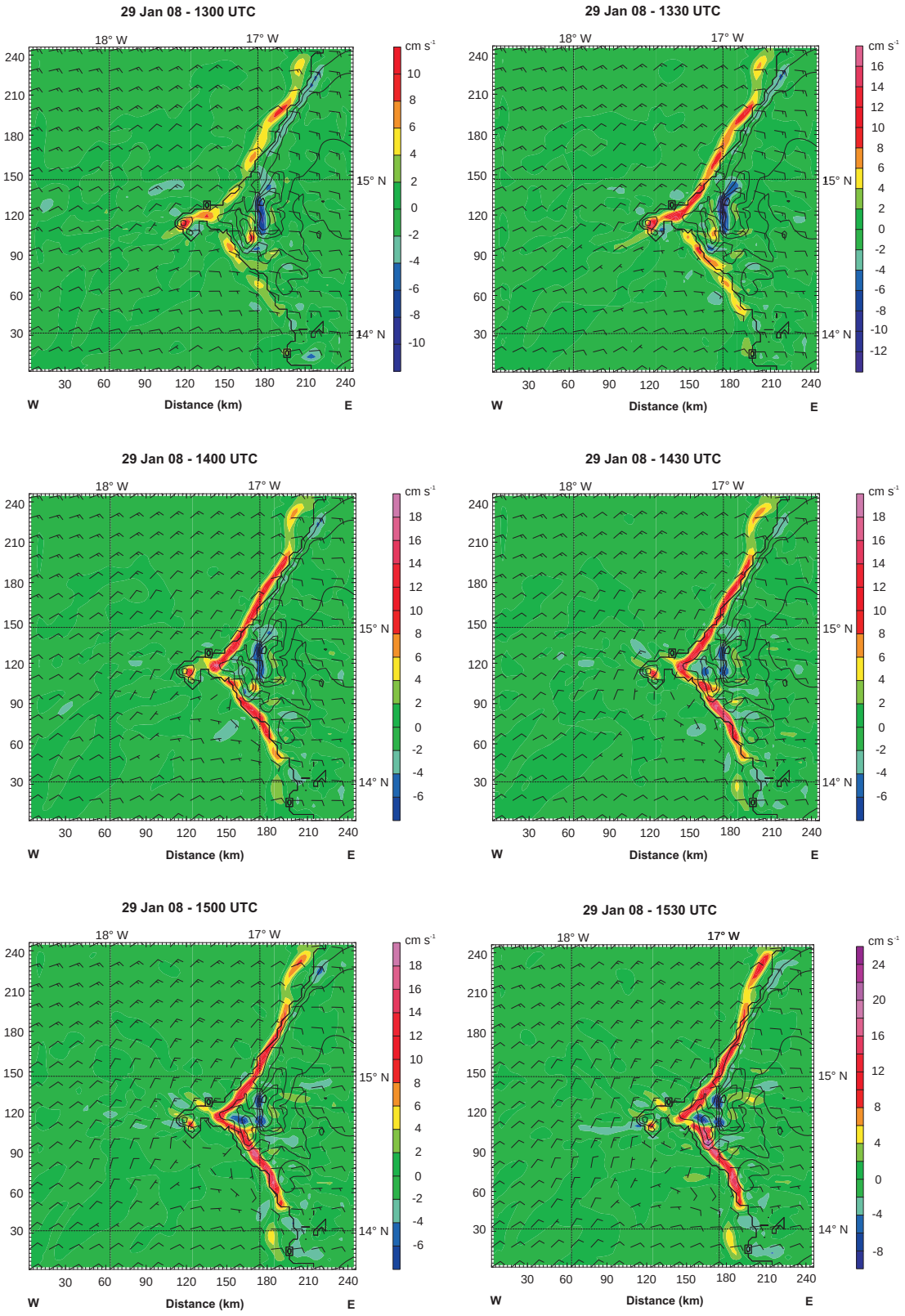

Figure A.2: MM5 vertical velocity (contours) and horizontal wind (black vanes) at $\sigma = 0.985$ for 29 January 2008, 13.00–15.30 UTC; black lines show orography in intervals of 20 m.

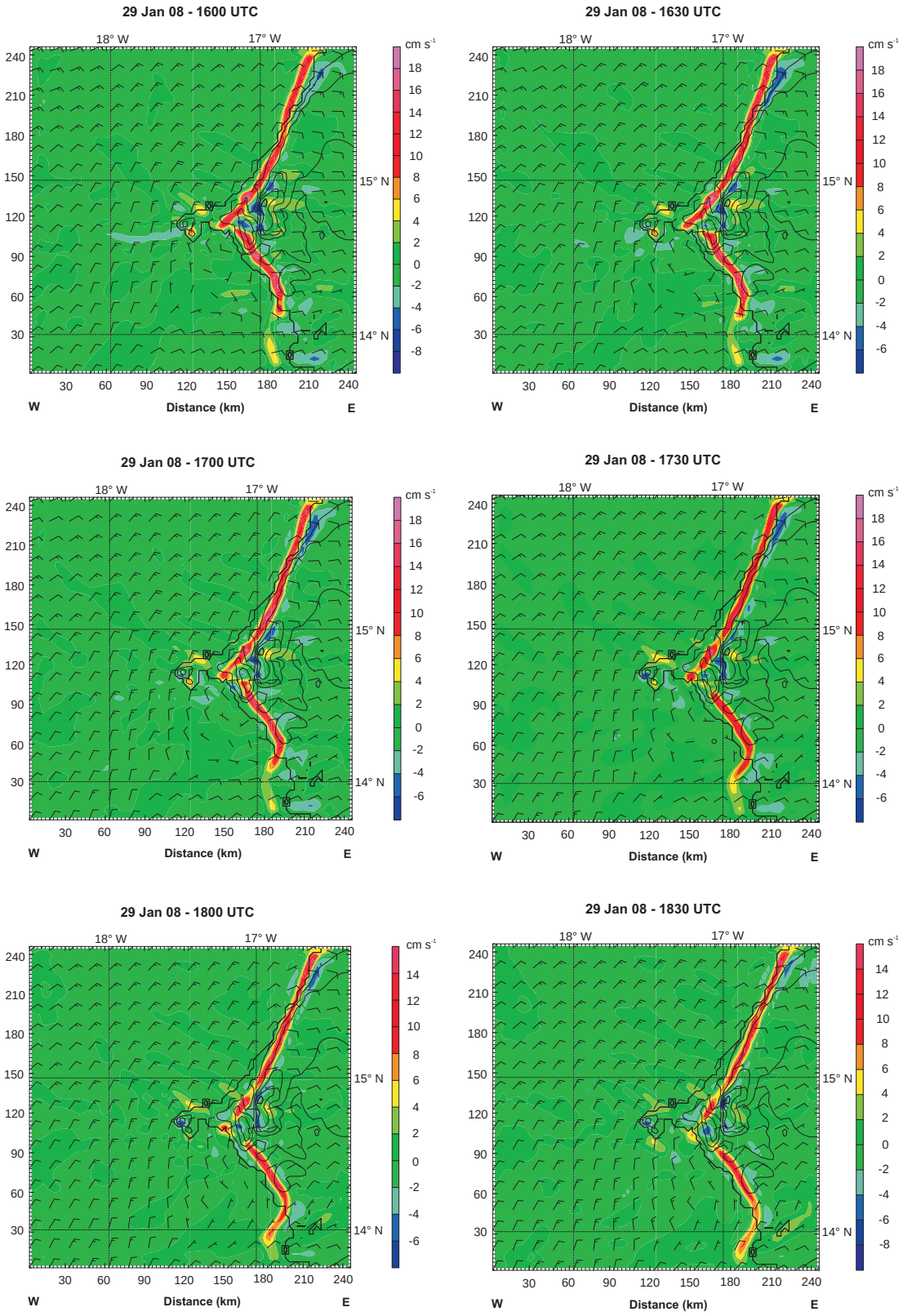

Figure A.3: MM5 vertical velocity (contours) and horizontal wind (black vanes) at $\sigma = 0.985$ for 29 January 2008, 16.00–18.30 UTC; black lines show orography in intervals of 20 m.

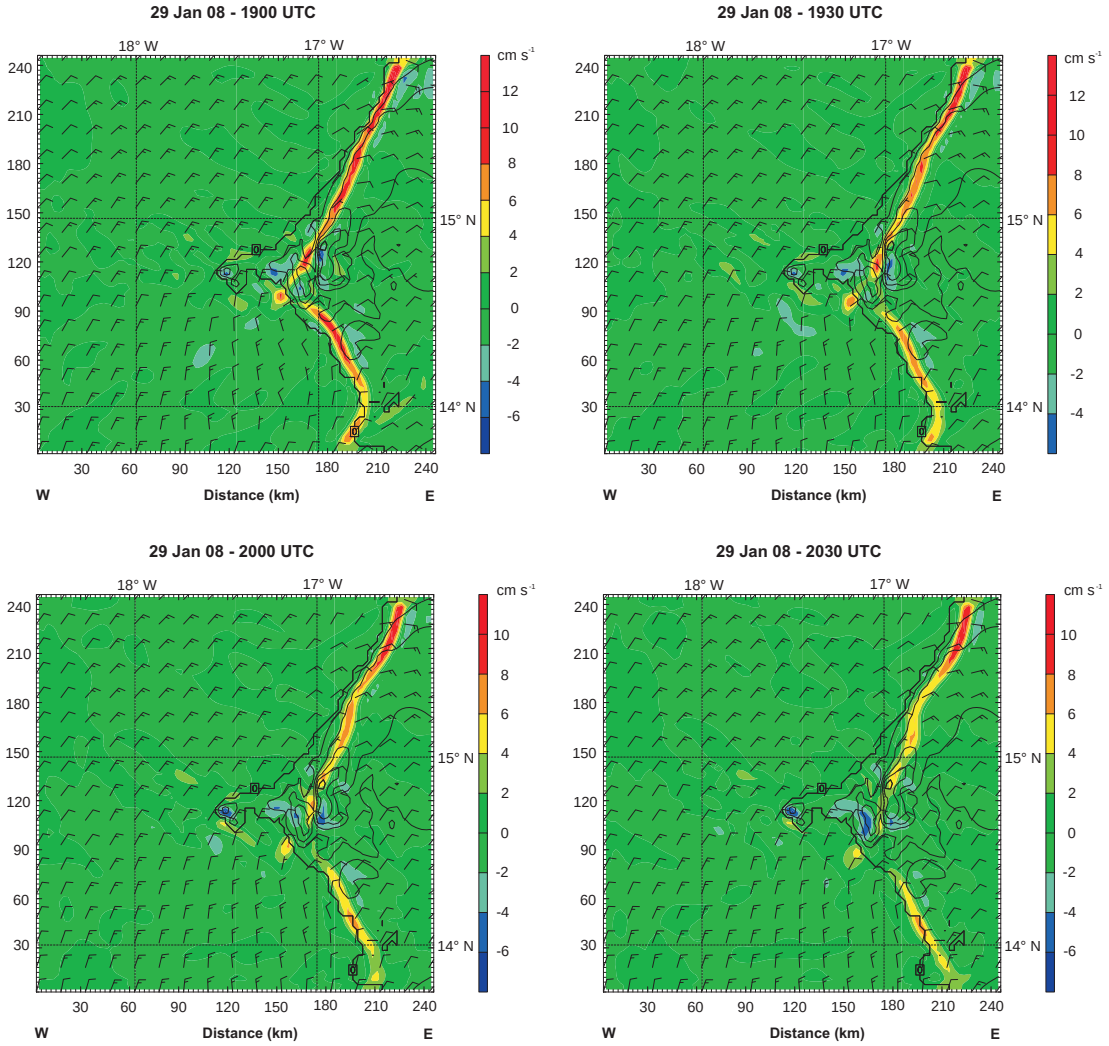

Figure A.4: MM5 vertical velocity (contours) and horizontal wind (black vanes) at $\sigma = 0.985$ for 29 January 2008, 19.00–20.30 UTC; black lines show orography in intervals of 20 m.

Relative humidity at the surface

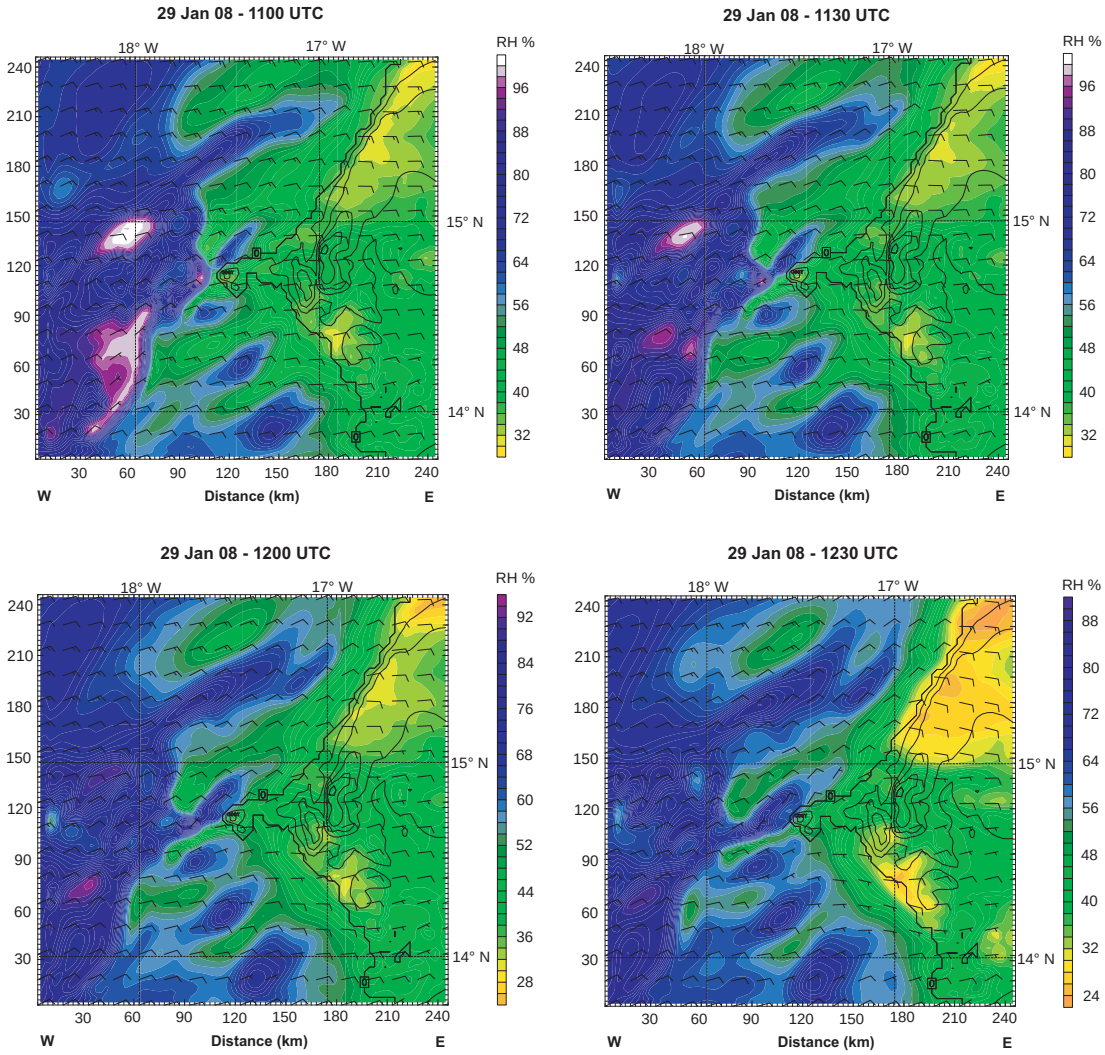

Figure A.5: MM5 relative humidity (contours) and horizontal wind (black vanes) at the surface for 29 January 2008, 13.00–14.30 UTC; black lines show orography in intervals of 20 m.

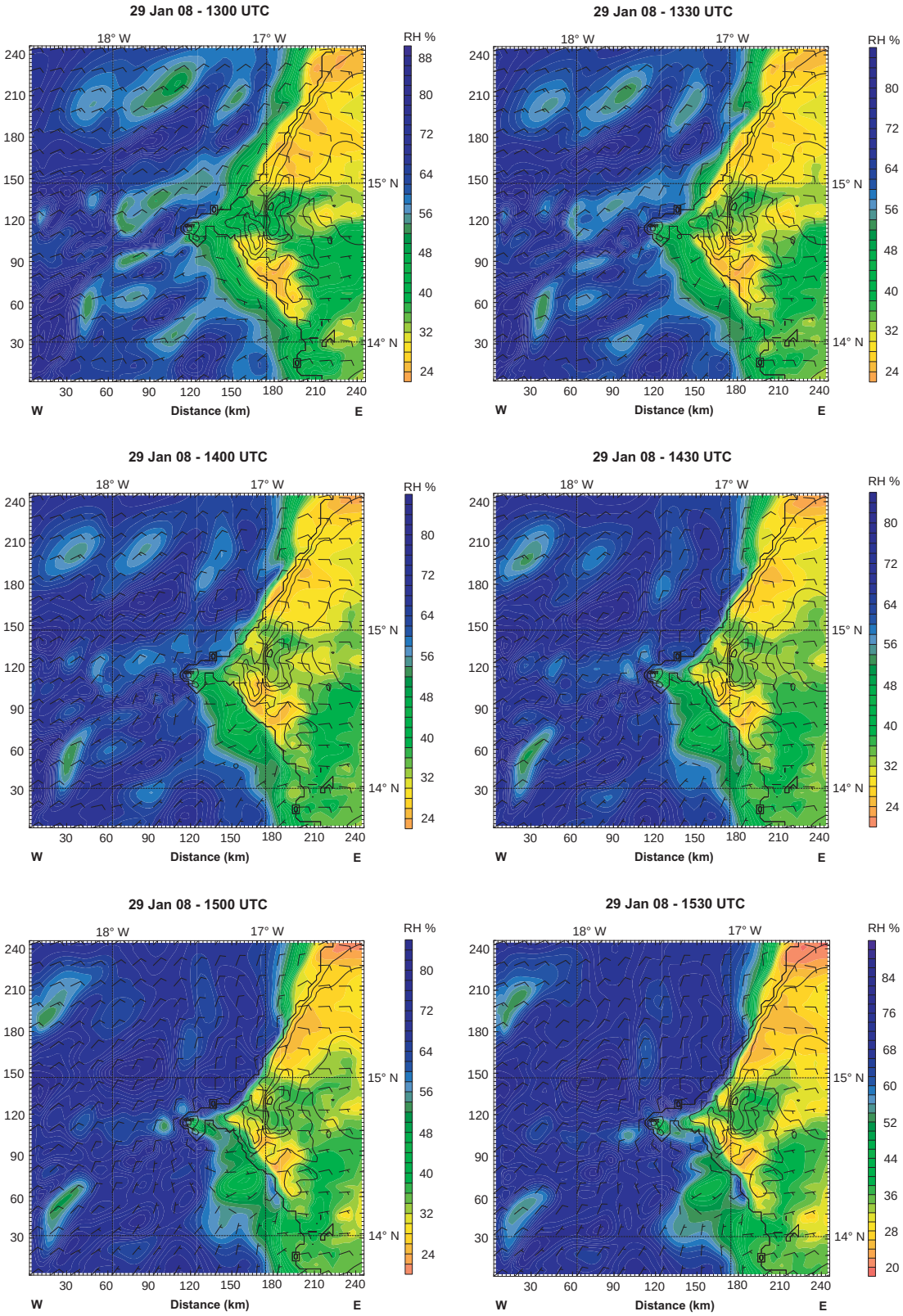

Figure A.6: MM5 relative humidity (contours) and horizontal wind (black vanes) at the surface for 29 January 2008, 15.00–20.30 UTC; black lines show orography in intervals of 20 m.

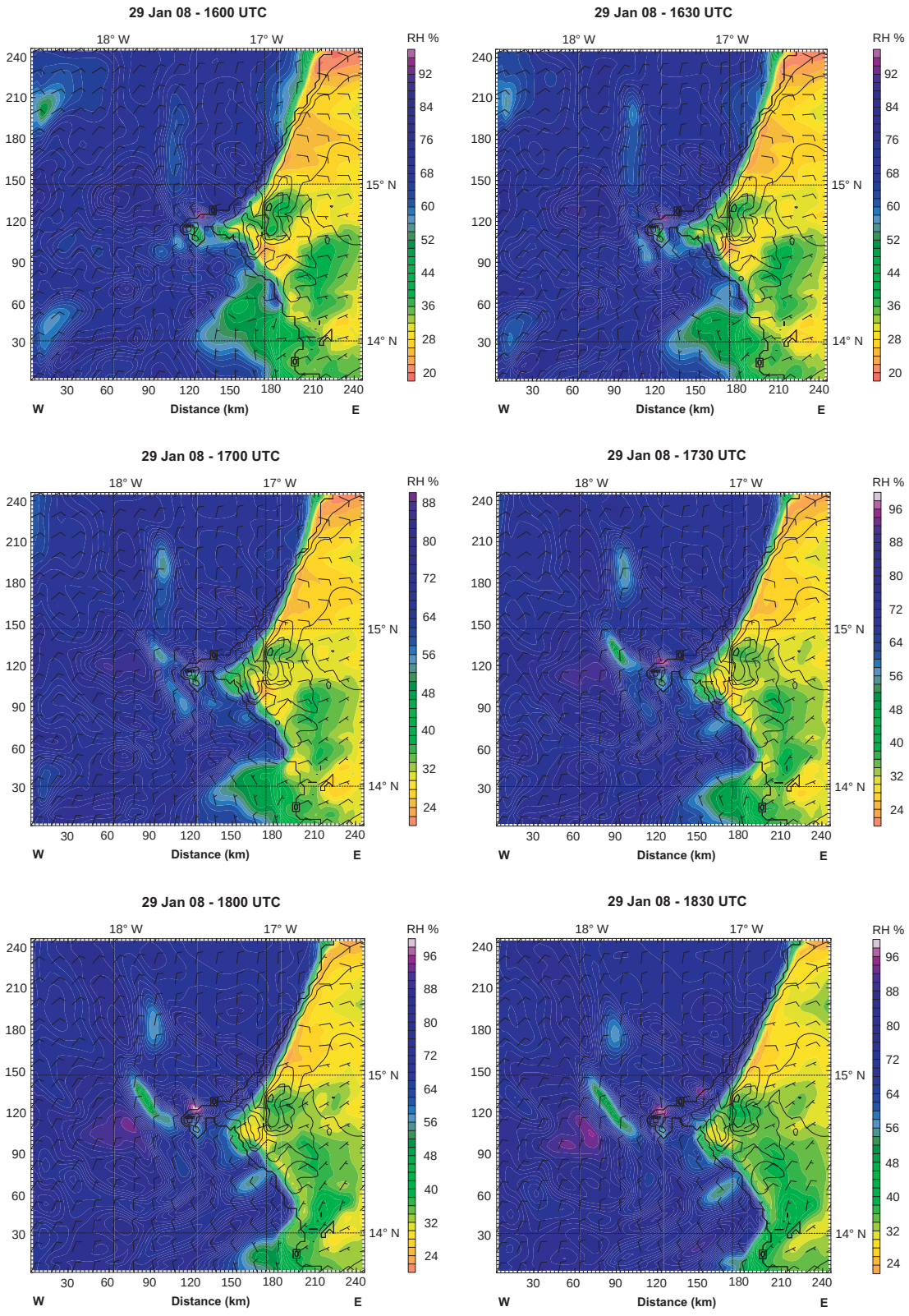

Figure A.7: MM5 relative humidity (contours) and horizontal wind (black vanes) at the surface for 29 January 2008, 15.00–20.30 UTC; black lines show orography in intervals of 20 m.

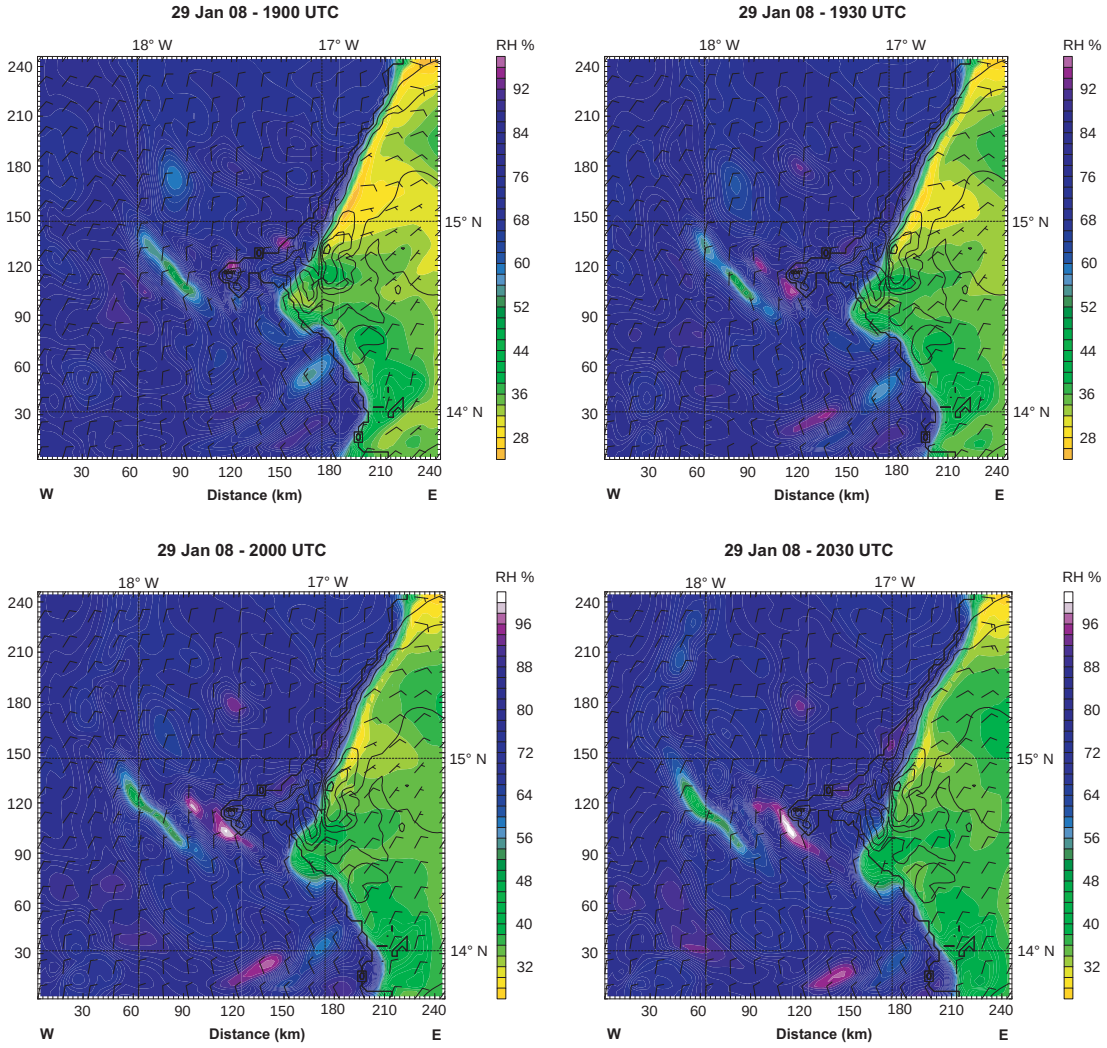

Figure A.8: MM5 relative humidity (contours) and horizontal wind (black vanes) at the surface for 29 January 2008, 15.00–20.30 UTC; black lines show orography in intervals of 20 m.

Relative humidity at 900 m a.s.l.

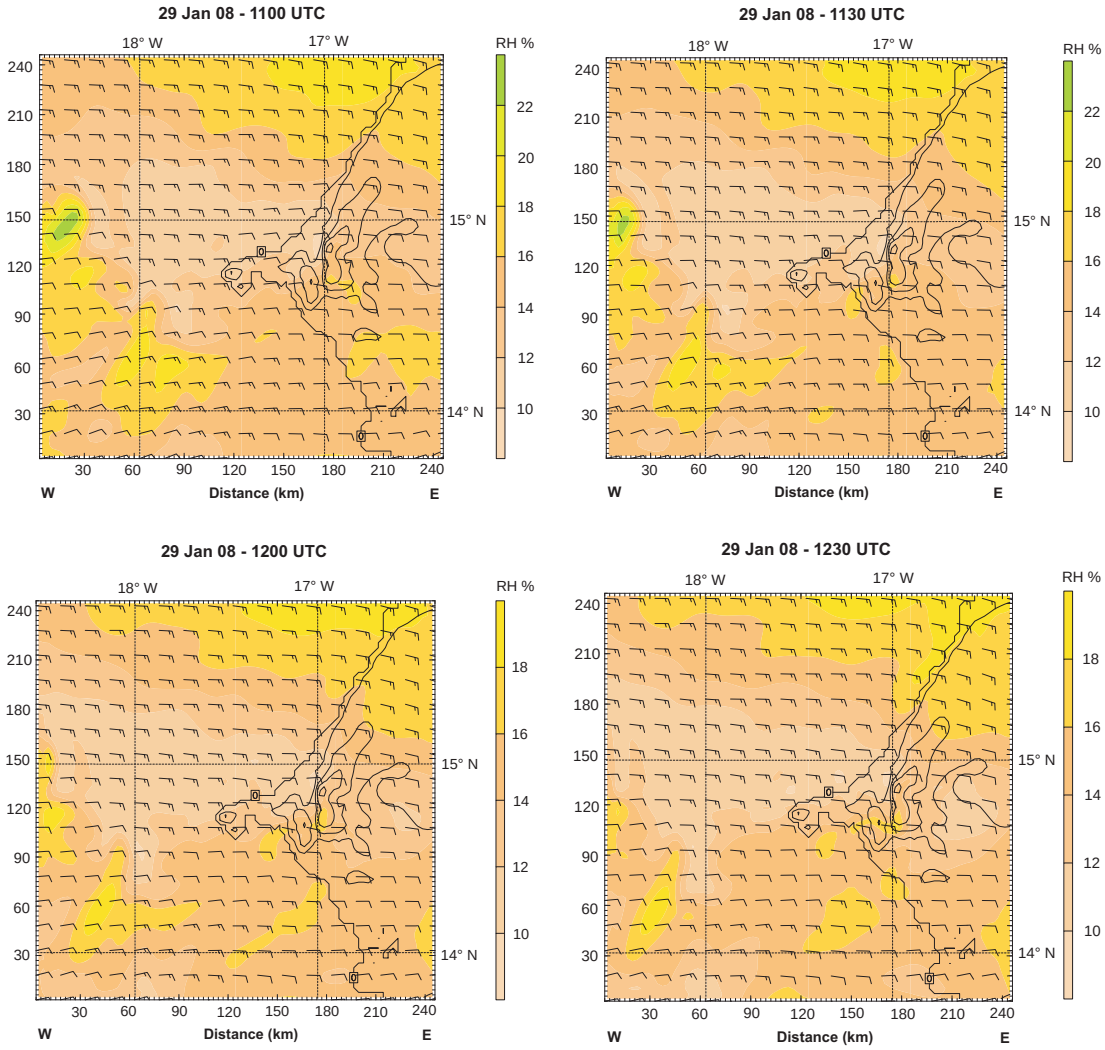

Figure A.9: MM5 relative humidity (contours) and horizontal wind (black vanes) at 900 m a.s.l. for 29 January 2008, 11.00–12.30 UTC; black lines show orography in intervals of 20 m.

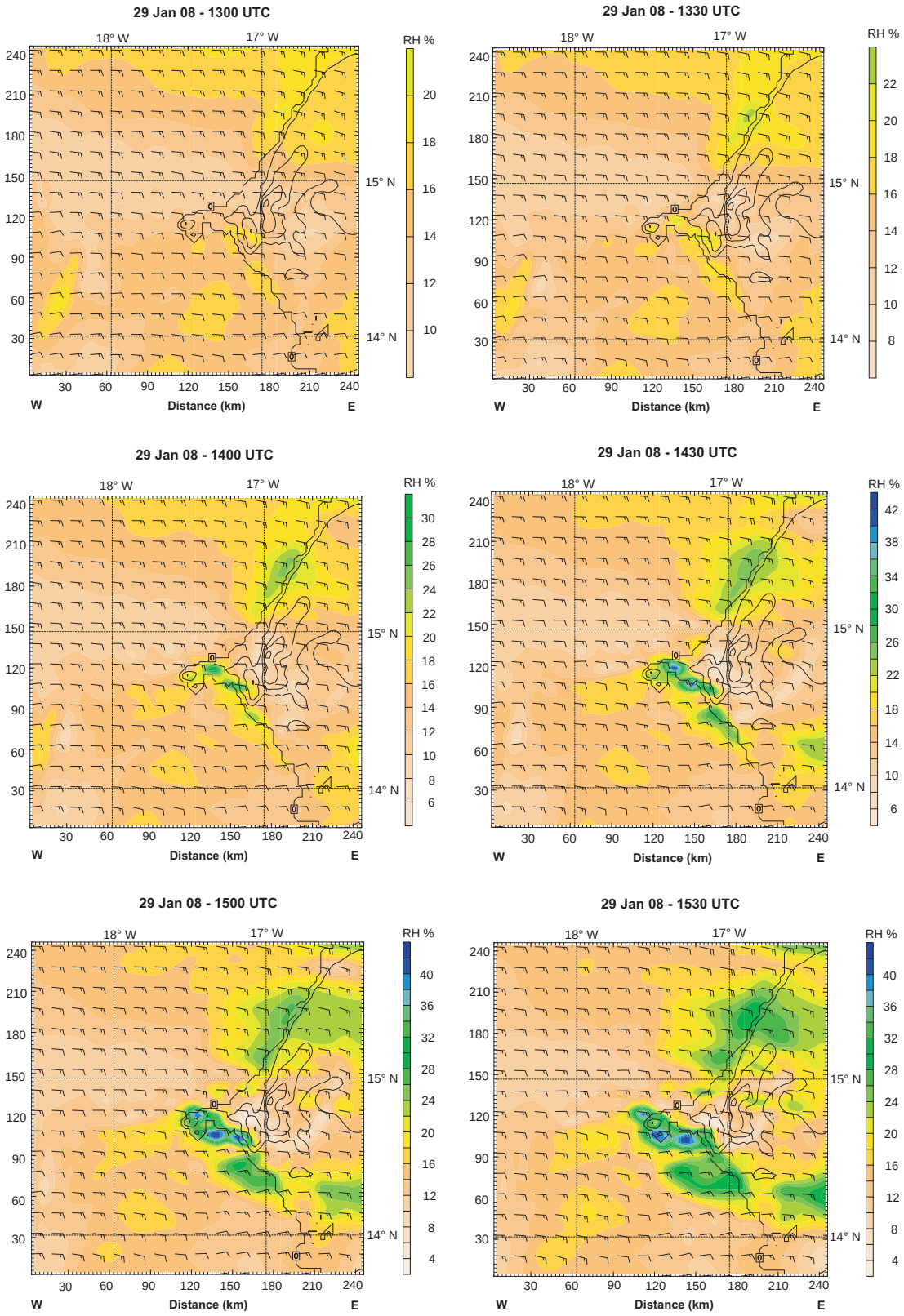

Figure A.10: MM5 relative humidity (contours) and horizontal wind (black vanes) at 900 m a.s.l. for 29 January 2008, 13.00–15.30 UTC; black lines show orography in intervals of 20 m.

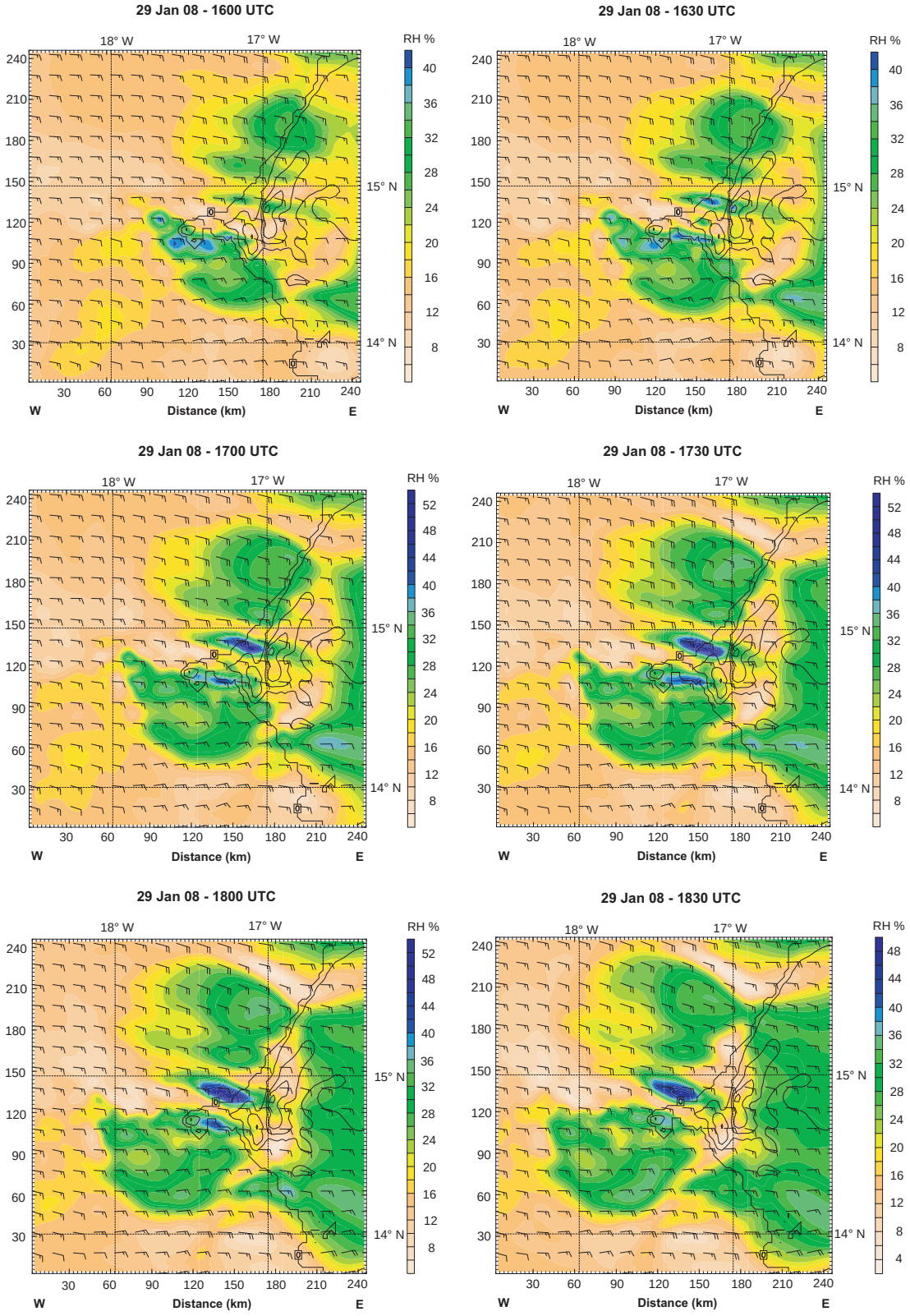

Figure A.11: MM5 relative humidity (contours) and horizontal wind (black vanes) at 900 m a.s.l. for 29 January 2008, 16.00–18.30 UTC; black lines show orography in intervals of 20 m.

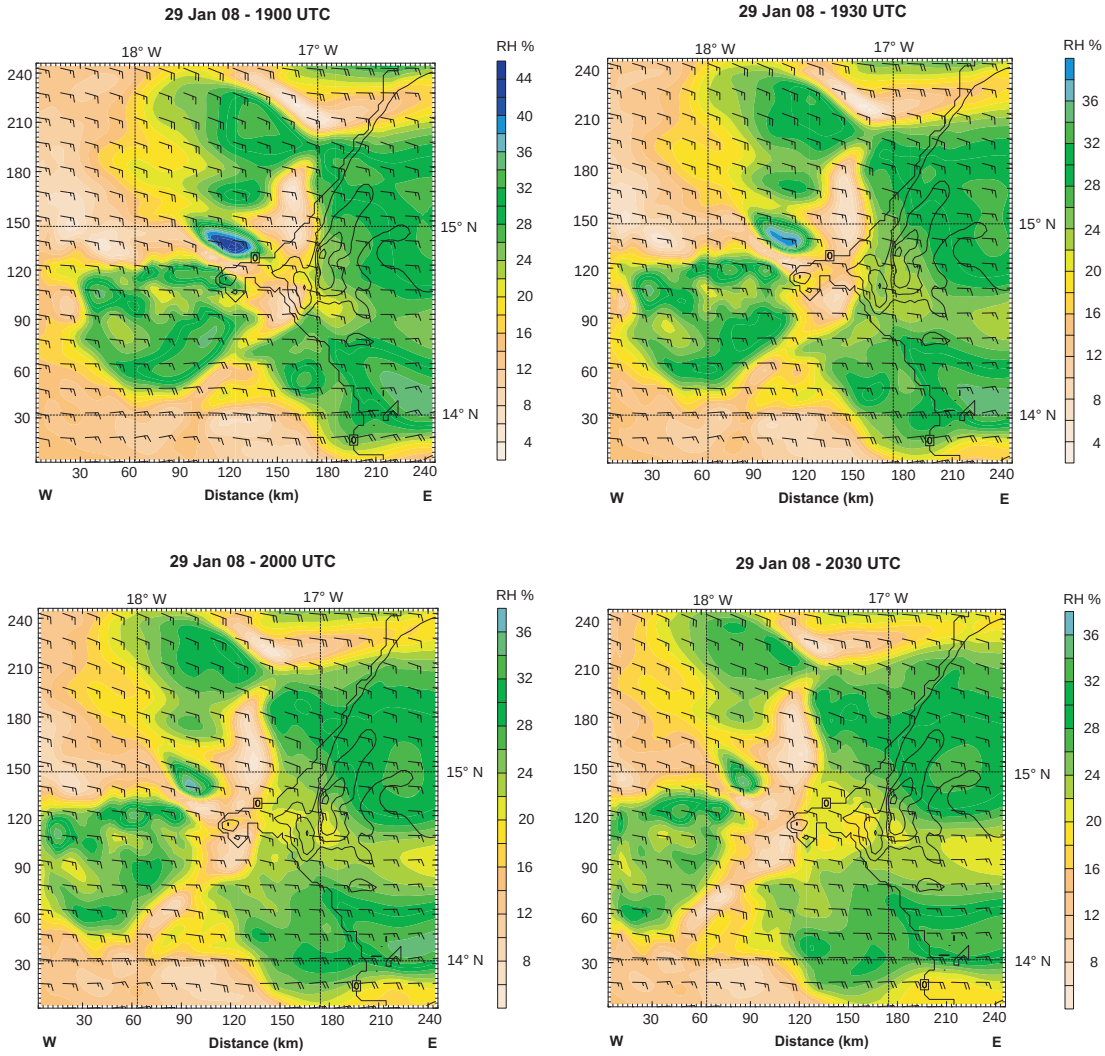

Figure A.12: MM5 relative humidity (contours) and horizontal wind (black vanes) at 900 m a.s.l. for 29 January 2008, 19.00–20.30 UTC; black lines show orography in intervals of 20 m.

Vertical cross sections

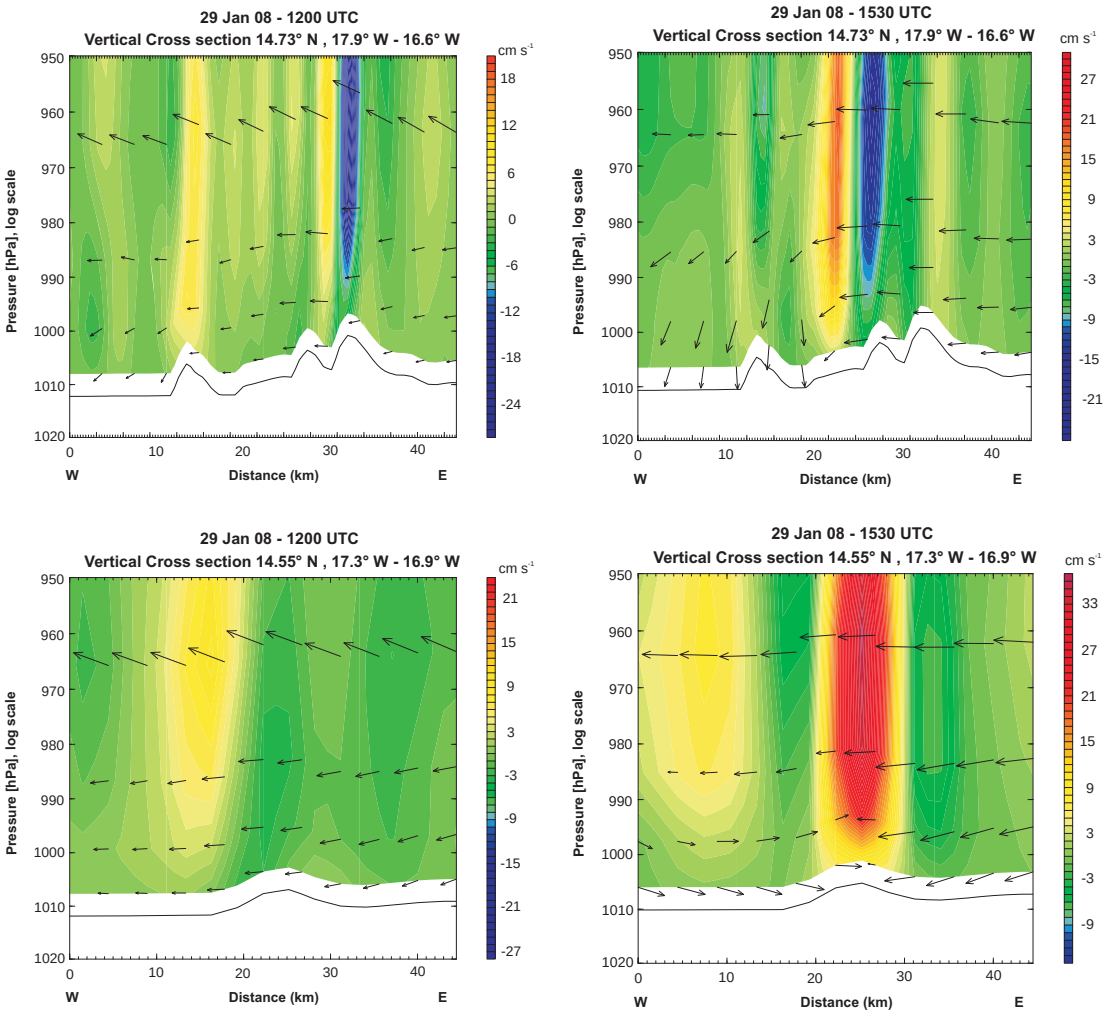

Figure A.13: MM5 vertical cross sections in W-E direction for the Dakar peninsula (upper plots) and the area 20 km south of Dakar (lower plots) for 12 UTC and 15.30 UTC. Arrows show horizontal wind speed and direction, contours indicate vertical motion.

Appendix B

HSRL Figures

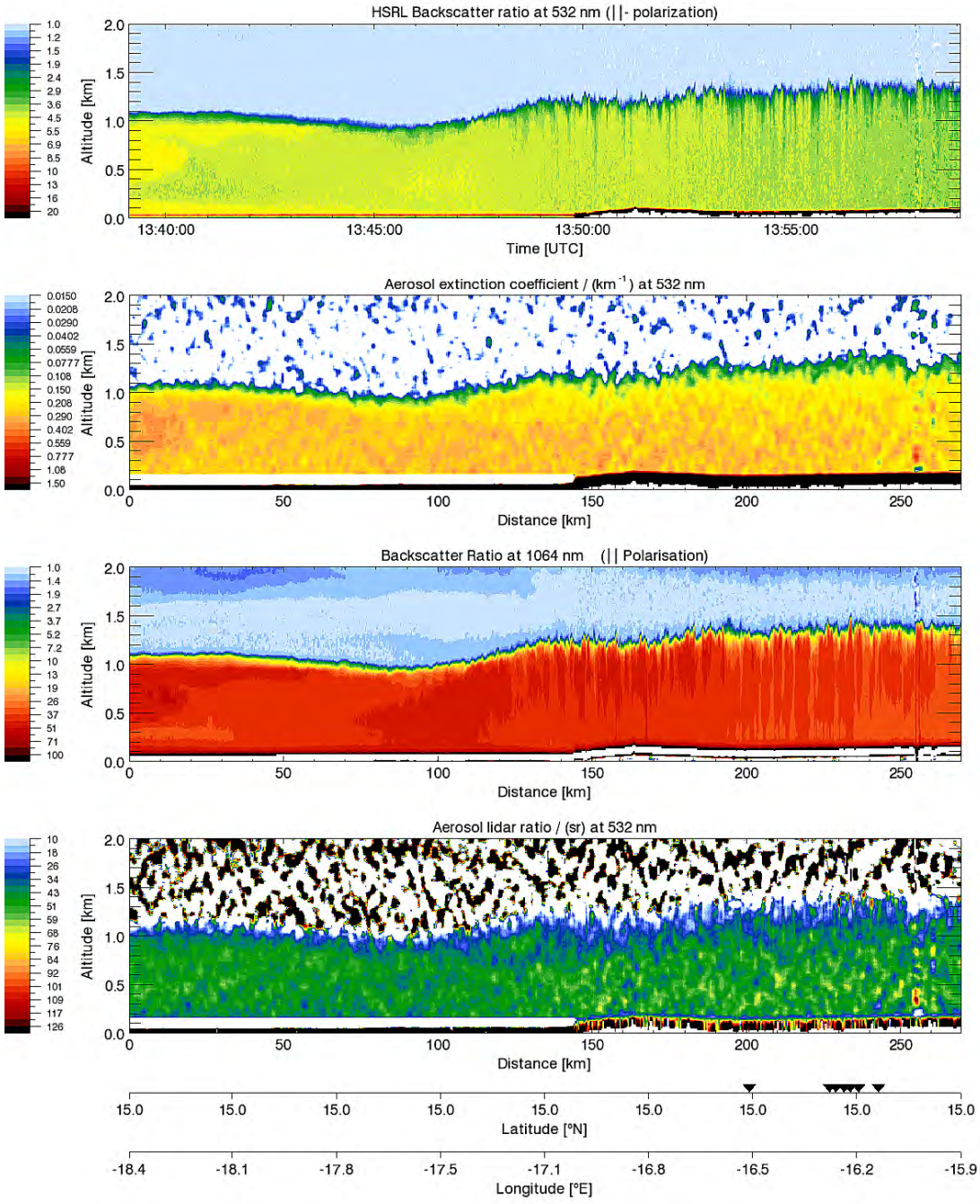

Figure B.1: HSRL coast line cross sections for flight #290108a. The coast line was crossed about 40 km north of Dakar at about 13.50 UTC; see latitude and longitude information below the charts.

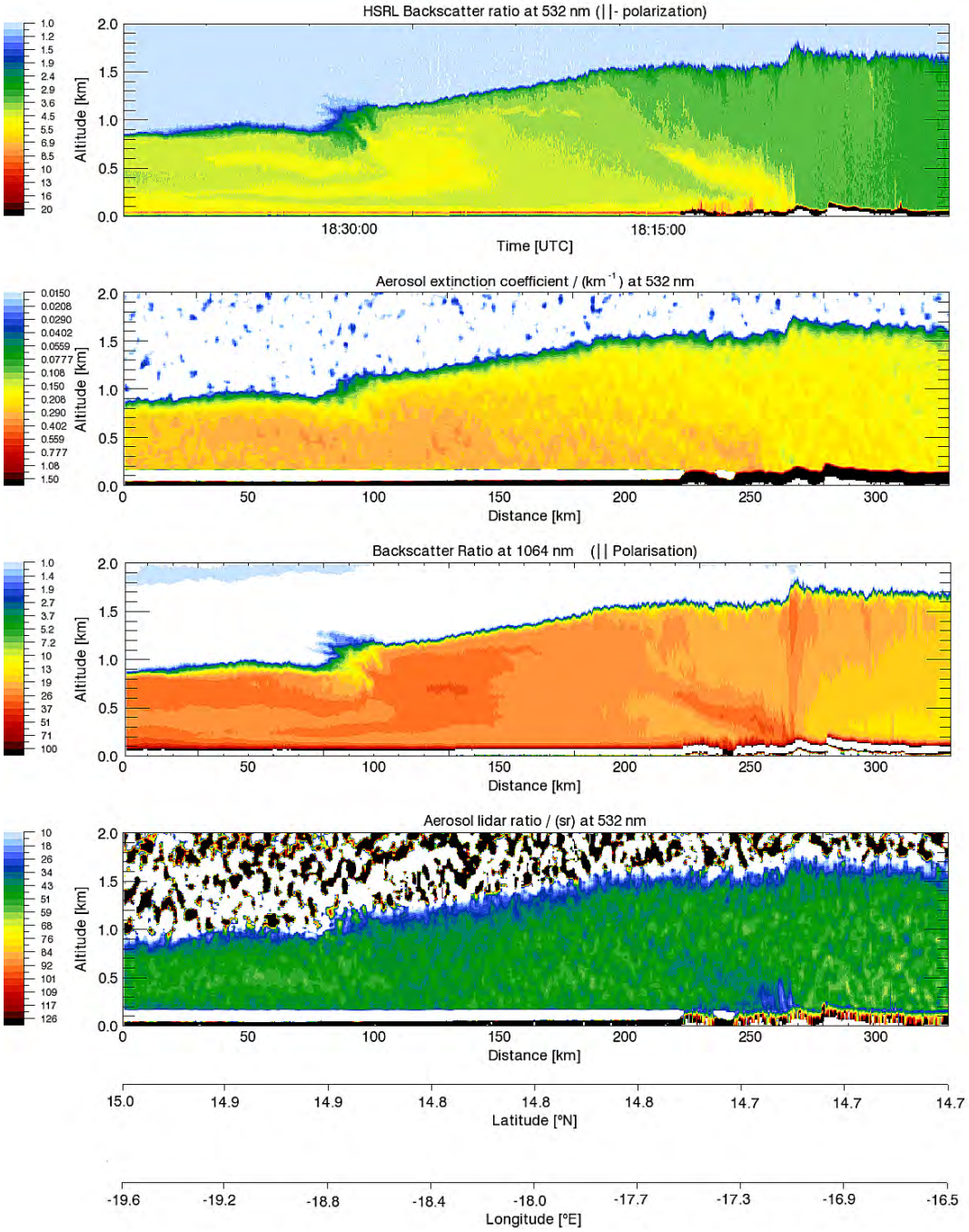

Figure B.2: HSRL coast line cross sections for flight #290108b. The coast line was crossed directly over Dakar at about 18.15 UTC; see latitude and longitude information below the charts.

List of Abbreviations

Abbreviation	Description
Abbreviation	Description
ACE	Aerosol characterization experiment
AMMA	African Monsoon Multidisciplinary Analysis
anth	Anthropogenic
ATN	Attenuation of light intensity
AOD	Aerosol optical depth
BC	Black carbon
CIBL	Convective internal boundary layer
CPC	Condensation particle counter
CPSA	Condensation particle size analyzer
DFG	Deutsche Forschungsgemeinschaft
DKR	Dakar airport
DMA	Differential mobility analyzer
DLR	Deutsches Zentrum für Luft- und Raumfahrt
ECMWF	European centre for medium-range weather forecasts
ESA	European Space Agency
EUMETSAT	European organization for the exploitation of meteorological satellites
FLYTUL	Flight analysis tool using LAGRANTO
GPaC	Giant particle counter
GS	Gayno-Seaman (boundary layer parametrization
HSRL	High spectral resolution lidar
ICAROHS	Inter-Comparison of Aerosol Retrievals and Observational Requirements for multi-wavelength HSRL Systems
Im	Imaginary part of complex refractive index
IPCC	Intergovernmental panel on climate change
KHB	Kelvin-Helmholtz billow

Continued on Next Page...

Continued List of Abbreviations

Abbreviation	Description
LAGRANTO	Lagrangian analysis tool
Lidar	Light detection and ranging
MM5	Mesoscale meteorology model 5
MODIS	Moderate-resolution imaging spectroradiometer
ms	Mineral dust
OPC	Optical particle counter
PBL	Planetary boundary layer
PCASP	Passive cavity aerosol spectrometer probe
PSAP	Particle soot absorption photometer
RAI	Praia airport
Re	Real part of complex refractive index
RF	Radiative forcing
SAMUM	Saharan mineral dust experiment
SBC	Sea-breeze circulation
SBF	Sea-breeze front
SBG	Sea-breeze gravity current
SBH	Sea-breeze head
ss	Sea salt
SSA	Single scattering albedo
TD	Thermodenuder
UTC	Universal time coordinated
WMO	World meteorological organization
TRACE-P	Transport and chemical evolution over the Pacific

List of Symbols

Symbol	Description
ϵ	Permitivity
γ	Surface tension
λ	Wavelength
μ	Permeability
ν	Ratio of specific heats
ω	Frequency
ω_0	Single scattering albedo
Ω	Solid angle
ϕ	Azimuth angle
ρ	Density
σ	MM5 vertical coordinate
σ_{ap}	Absorption coefficient
σ_{sp}	Scattering coefficient
σ_{ext}	Extinction coefficient
θ	Scattering angle
Θ	Potential temperature
å_{ap}	absorption ångström coefficient
å_{ext}	extinction ångström coefficient
A	Surface
CMD	Count median diameter
C	Circulation
C_{abs}	Absorption cross section
C_{ext}	Extinction cross section
C_{sca}	Scattering cross section
D	Diffusion coefficient

Continued on Next Page...

Continued List of Symbols

Symbol	Description
d_p	Particle diameter
E	Electric field
f	Coriolis parameter
F	Flow (PSAP)
ik	Imaginary part of the ref index
I	Irradiance
k_B	Boltzmann coefficient
$\mathbf{k}$	Wave vector
K_0	Coagulation constant
g	Gravitational acceleration
g_l	Gibbs free energy of liquid phase
g_v	Gibbs free energy of vapor phase
G	Gibbs free energy
GSD	Geometric standard deviation
H	Sea-breeze circulation height
$\mathbf{H}$	Magnetic field
L	Sea-breeze cross-shore length
N	Number of particles/molecules
m	Complex refractive index
m	Map scale factor
n	Real part of the ref index
p	Pressure
P_n^m	Legrendre functions of first kind
Q	Heat
Q_{ext}	Extinction efficiency
r_P	Particle radius
Re	Real part
R	Gas constant
S	Entropy
S_a	Lidar ratio
S_j	Scattering matrix elements
$\mathbf{S}$	Poynting vector

Continued on Next Page...

Continued List of Symbols

Symbol	Description
t	Time
T	Temperature
TEM	Transmission electron microscopy
TR	Transmission
u	x-component of horizontal velocity
$\mathbf{u}$	Velocity vector
U	Internal energy of a system
v	y-component of horizontal velocity
$\vec{v}$	Horizontal velocity vector
V	Volume
w	Vertical velocity
W	Electromagnetic energy
X	Vector scattering amplitude

List of Figures

1.1 Aerosol radiative forcing effects 1
1.2 Global aerosol optical depth at 0.55 μm 2
1.3 Radiative transfer calculation scheme 3
1.4 SAMUM project map 4

2.1 Evolution of tropospheric aerosol 8
2.2 Idealized size distribution modes 12
2.3 Coordinate system for scattering plane 15
2.4 Angle-dependent scattering intensity for spherical particles 18
2.5 Wavelength dependency of the complex refractive index 20
2.6 Types of aerosol mixtures 20
2.7 Schematics of a sea breeze system 23
2.8 Theoretical treatment of a sea breeze system 24
2.9 MM5 grid configurations 26

3.1 Photos of the isokinetic Flacon inlets 30
3.2 Schematics of an aircraft-borne CPC 32
3.3 Example of a CPC counting efficiency curve 33
3.4 Schematics of the PCASP-100X optical system 34
3.5 PCASP scattering cross section 35
3.6 Schematic of the typical PSAP set-up 36
3.7 Schematics of a thermodenuder 39
3.8 Principle set-up of a lidar system 40
3.9 Principle set up of the HSRL 41
3.10 TEM field images of pure and externally mixed soot 43
3.11 Overall data analysis scheme of this case study 44
3.12 PSAP data analysis scheme 45
3.13 MM5 model domains 50
3.14 MM5 terrain of domain D02 and D03 51

4.1 Satellite pictures dust storm episode 28 - 30 January 2008 54
4.2 Back trajectories Praia, 950 hPa-starting-level 55
4.3 Back trajectories Praia, 775 hPa starting-level 55
4.4 Flight patterns #290108a and #290108b 56
4.5 Map of the aerosol optical depth Senegal - Cape Verdes 57
4.6 HSRL extinction profiles and PSAP absorption 58
4.7 Total number concentrations approach and climb-out Dakar 59
4.8 Map of measurement sequences approach Dakar 60
4.9 HSRL vertical cross sections 61
4.10 HSRL vertical cross section zoom Dakar 62

4.11 ECWF wind field 1000 hPa and 925 hPa 64
4.12 Dakar vertical profiles measured by the Falcon 66
4.13 MM5 results for vertical velocity and horizontal wind 68
4.14 MM5 sounding Dakar airport 70
4.15 MM5 relative humidity at 900 m a.s.l. and 640 m a.s.l. 71
4.16 Trajectories for in-situ measurements Dakar 72
4.17 MM5 back trajectories for climb-out Dakar 72
4.18 Comparison of size distributions 76
4.19 PCASP channel-wise increase in particle number concentration 77
4.20 Fraction of non-volatile particles and ratio of sub-μm absorption 78
4.21 Scatter plot non-volatile fracitons 79
4.22 Ångström exponents for various sequences 81
4.23 Singe scattering albedo from the PSAP data inversion scheme 81
4.24 Refractive indices from PSAP data analysis 82
4.25 Effective chemical compositions for several sequences 83
4.26 Chemical composition from impactor samples 84
4.27 PSAP iron oxide and soot volume ratios for impactor samples 85

5.1 LAGRANTO back trajectories for impactor samples 91
5.2 MM5 back trajectories for impactor samples 92
5.3 Forward trajectories for the Dakar plume 93

A.1 MM5 vertical velocity and horizontal wind 11.00 - 12.30 UTC 111
A.2 MM5 vertical velocity and horizontal wind 13.00 - 15.30 UTC 112
A.3 MM5 vertical velocity and horizontal wind 16.00 - 18.30 UTC 113
A.4 MM5 vertical velocity and horizontal wind 19.00 - 20.30 UTC 114
A.5 MM5 relative humidity at the surface 13.00 - 14.30 UTC 115
A.6 MM5 relative humidity at the surface 15.00 - 20.30 UTC 116
A.7 MM5 relative humidity at the surface 15.00 - 20.30 UTC 117
A.8 MM5 relative humidity at the surface 15.00 - 20.30 UTC 118
A.9 MM5 relative humidity at 900 m a.s.l. part 11.00 - 12.30 UTC 119
A.10 MM5 relative humidity at 900 m a.s.l. 13.00 - 15.30 UTC 120
A.11 MM5 relative humidity at 900 m a.s.l. 16.00 - 18.30 UTC 121
A.12 MM5 relative humidity at 900 m a.s.l. 19.00 - 20.30 UTC 122
A.13 MM5 vertical cross sections 123

B.1 HSRL cross section 40 km north of Dakar 126
B.2 HSRL cross section for the Dakar region 127

List of Tables

2.1 Coagulation effects on number concentrations 10
2.2 Moments of the size distribution function 11
2.3 Typical size distribution modes 12

3.1 Overview of used measurement techniques 31
3.2 Constants for calculation of σ_{ap} from PSAP raw signal 38
3.3 refractive indices used for the PSAP data analysis 48
3.4 Set up of MM5 model domains 51

4.1 aerosol optical thickness for selected sequences 58
4.2 ECMWF analysis and synoptic data for Dakar airport 65
4.3 Summary of measured aerosol properties 75
4.4 Anthropogenic contribution to aerosol absorption 80

5.1 Analysis method performances used for investigation 87
5.2 Classification of analysis method performances 88
5.3 Comparison MM5 - Falcon in-situ data 90

A.1 Vertical Levels of the MM5 110

Acknowledgment

First of all I would like to thank Dr. Andreas Petzold for the excellent general supervision and the freedom to realize my own ideas during my placements and the development of this thesis.

I also would like to thank Prof. Dr. Bernhard Mayer for co-examining in general and the great interest in my thesis including useful suggestions in particular.

Furthermore I would particularly like to thank Dr. Gerald Thomsen (LMU), Dr. Christoph Kiemle (DLR), Dr. Thomas Hamburger and Amir Ibrahim (both DLR), Dr. Kirsten Lieke and Dr. Konrad Kandler (both TU Darmstadt) for instructions, personal communication and patience referring to my question. Without them this work would not have become what it is.

I'm grateful to Prof. Dr. Ulrich Schumann and Dr. Hans Schlager for enabling me to work on this thesis at the Institut für Physik der Atmosphäre, DLR, Oberpfaffenhofen.

Moreover I also would like to thank all my colleagues at the department for the pleasant working atmosphere, many interesting conversations and illustrious coffee breaks. I really enjoyed my time in the department.

Furthermore I want to thank all my friends from Munich and Würzburg who accompany and support me since many years. I promise you to catch up on everything we neglected during the last busy months. In the end I have to thank my parents who provided me with self-confidence, helped me to develop my talents and supported me wherever they could. You established the real basis of this thesis. Beyond that I would like to thank my girlfriend Julia. I'm deeply grateful for your patience and your encouragement and for bringing back sunshine to my life.

Erklärung

Hiermit erkläre ich, dass ich die vorliegende Arbeit selbstständig und nur unter Verwendung der angegebenen Literatur und Hilfsmittel erstellt habe.

München, den 31.März 2011

Andreas Veira